

American University in Cairo

## AUC Knowledge Fountain

---

Theses and Dissertations

---

2-1-2015

### Nanocomposites of Layered Clays and graphene/graphene oxide for drug delivery

Nada Mahmoud Hegazy

Follow this and additional works at: <https://fount.aucegypt.edu/etds>

---

#### Recommended Citation

##### APA Citation

Hegazy, N. (2015). *Nanocomposites of Layered Clays and graphene/graphene oxide for drug delivery* [Master's thesis, the American University in Cairo]. AUC Knowledge Fountain.

<https://fount.aucegypt.edu/etds/215>

##### MLA Citation

Hegazy, Nada Mahmoud. *Nanocomposites of Layered Clays and graphene/graphene oxide for drug delivery*. 2015. American University in Cairo, Master's thesis. *AUC Knowledge Fountain*.

<https://fount.aucegypt.edu/etds/215>

This Thesis is brought to you for free and open access by AUC Knowledge Fountain. It has been accepted for inclusion in Theses and Dissertations by an authorized administrator of AUC Knowledge Fountain. For more information, please contact [mark.muehlhaeusler@aucegypt.edu](mailto:mark.muehlhaeusler@aucegypt.edu).

# **The American University in Cairo**

School of Science and Engineering

Nanotechnology Graduate Program



## **Nanocomposites of Layered Clays and graphene/graphene oxide for drug delivery**

A thesis submitted in partial fulfillment of the requirements for the  
degree of

Master of Science in Nanotechnology

**By Nada Mahmoud Hegazy**

Under the supervision of

**Prof. Adham Ramadan**

Fall 2015

The American University in Cairo

**Nanocomposites of Layered Clays and  
graphene/graphene oxide for drug delivery**

A Thesis submitted by

Nada Mahmoud Hegazy

To the Nanotechnology Graduate Program

Fall 2015

A thesis submitted in partial fulfillment of the requirements for the degree of  
Master of Science in Nanotechnology

Has been approved by

Thesis Committee Supervisor /Chair: Dr. Adham R. Ramadan

Affiliation: Professor of Chemistry and Dean of Graduate Studies, the American  
University in Cairo.

Thesis External Examiner: Dr. Omaima N. El Gazayerly

Affiliation: Professor and Chair of the Pharmaceutics and Industrial Pharmacy  
Department, Faculty of Pharmacy, Cairo University.

Thesis Internal Examiner: Dr. Wael Mamdouh

Affiliation: Assistant Professor of Chemistry, Chemistry Department, School of Sciences  
and Engineering, the American University in Cairo.

Thesis Committee Moderator: Dr. Mayyada El Sayed

Affiliation: Visiting Assistant Professor of Chemistry, Chemistry Department, School of  
Sciences and Engineering, the American University in Cairo.

\_\_\_\_\_  
Program Director

\_\_\_\_\_  
Date

\_\_\_\_\_  
Dean

\_\_\_\_\_  
Date

# Acknowledgment

Research work was a significant experience for me, not only on the academic level, but also on the personal level. It has added to my research experience, and added to my circle of acquaintances.

First of all, I would like to thank my big family: parents, grandparents, sister, brother, aunt, and uncles. Each one of them provided me with emotional support, they were patient and standing out there for me all along. Their prayers and encouraging is what sustained me that far.

A special appreciation and sincere gratitude to my advisor Prof. Adham Ramadan, for being a tremendous mentor and for his continuous support, patience, and immense knowledge. His guidance helped so much throughout the research, and am really grateful to him for accepting me to work under his supervision.

My sincere gratitude to the huge technical support, provided by Mr. Mahmoud Abdel Moez, and Mr. Emad Farag. I am also very grateful to Mr. Ahmed Omayya for being a supportive friend in my research work and for facilitating a lot of technicalities. Without their help, I wouldn't have conducted this work.

I would like to acknowledge the support of my graduate professors, their educational material and advices.

Last but definitely not least, my colleagues who turned to be best friends ever, who made this experience more fun and smooth. Words are not enough to express how supportive they were throughout my research work, career and on a personal level. Thanks for each and every one of them: Zahraa, Raghda, Alshaima, Yomna, Ruaa and Woroud.

# LIST OF ABBREVIATIONS

Abbreviation	Meaning
ALG	Alginate
BP	Benzyl penicillin
BSA	Bovine serum protein
CD44	Cluster determinant
CS	Chitosan
Cy	Cytamine
DA	Dopamine
DLS	Dynamic light scattering
DNA	Deoxy ribonucleic acid
DO	Dicetyl phosphate
DOX	Doxorubicin
FA	Folic acid
FPP	Farensyl diphosphate synthase
FT-IR	Fourier transform infrared
G	Graphene
GBMs	Graphene based materials
GIT	Gastro-intestinal tract
GO	Graphene oxide
GSH	Glutathione
GTPase	Guanosine triphosphate
HA	Hyaluronic acid
I.V.	Intravenous
IR	Infrared
KBr	Potassium bromide
LDH	Layered double hydroxide
LDV	Laser Doppler velocimetry
nBPs	Nitrogen containing bisphosphonates
NGO	Nano-carrier graphene oxide
NSAIDS	Non-steroidal anti-inflammatory drugs
PAA	Polyacrylic acid
PEG	Polyethylene glycole
rGO	Reduced graphene oxide
ROS	Reactive oxygen species
SA	Stearyl amine
SEM	Scanning electron microscope
SGF	Simulated gastric fluid
SLNs	Solid lipid nanoparticles
TMC	Trimethyl chitosan
U.V	Ultraviolet
USP	United state pharmacopeia
Vis	Visible
XRD	X-ray diffraction

# ABSTRACT

Layered double hydroxides (LDH) comprise a class of materials that can be either found as natural minerals or can be synthetically prepared. Their structure is composed of a mixture of divalent and trivalent metal cations, forming brucite-like layers, that are neutralized with anions in the interlayer gallery. They have unique physical and chemical characteristics such as: high surface area, large charge density, biocompatibility and exchange capacity. These have attracted attention to the LDHs as potential drug delivery vehicles.

Graphene (G) has also attracted the attention to exceptional properties, such as huge surface area, charge density concentration, membrane permeability by piercing mechanism and many others, expanding its use to include biomedical applications, such as drug delivery. Moreover, the possibility of large scale production of exfoliated graphene oxide (GO) sheets from G offered a further opportunity for their use. GO has a high exposed oxygenated surface that allows loading of large number of drugs by different bonding interactions and is dispersible in water.

Alendronate sodium is a water soluble nitrogen containing bisphosphonate (nBP) drug, that has low bioavailability (< 1 %) due to its low epithelial permeability. It also exhibits gastrointestinal adverse effects.

The objective of the work is to create a hybrid nanocomposite of Zn-Al LDH in its nitrate form with G/GO, (G/GO-Zn-Al-NO<sub>3</sub> LDH), combining the properties of these structures: membrane permeability and large interacting surface of G or GO, the buffering effect and the capability of the LDH in storing and controlling the drug release. The hybrid nanocomposites incorporated 2% w/w of G or GO with two different M<sup>2+</sup>/M<sup>3+</sup> ratios of LDH, 2:1 and 3:1. They were loaded with the drug by co-precipitation and ion exchange. The samples were characterized by XRD, FTIR, Zetasizer analyzer, and the amount of drug loaded and released were determined by UV/Vis spectroscopy, and the results were compared to those of drug-LDH controls. Samples that have show successful intercalation of the drug in bi-layered arrangement are: co-precipitation samples using M<sup>2+</sup>/M<sup>3+</sup> ratio of 3:1 (drug-LDH, G/GO-LDH), and ion-exchange samples, that don't incorporate G/GO (drug-LDH), prepared using either M<sup>2+</sup>/M<sup>3+</sup> ratios of 2:1 or 3:1. Their loading amounts ranged from 25.4 to 51 % w/w, and they exhibited a sustained release over 24 hours with a release percentages, ranging from 2.1% (1.07 mg) up to 4.2 % (1.52 mg). The other samples showed loading by surface adsorption on brucite-like layers of the LDH and the G or GO. They have drug loading amounts ranging, from 12.4 to 57.3 % w/w. This work demonstrated the potential of G/GO-Zn-Al LDH nanocomposites for sustained drug delivery.

# Table of contents

<b>LIST OF FIGURES.....</b>	<b>IX</b>
<b>LIST OF TABLES .....</b>	<b>XIII</b>
<b>1. Introduction.....</b>	<b>2</b>
1.1 Layered double hydroxides .....	2
1.1.1. Structure of LDH: .....	2
1.1.2. Preparation of LDH: .....	5
1.1.3. Post treatment of prepared LDH samples:.....	8
1.1.4. Precautions during LDH preparation:.....	8
1.1.5. Applications of LDH: .....	9
1.2 Graphene .....	10
1.2.1. Structure of G: .....	10
1.2.2. Graphene oxide: .....	11
1.2.3. GO preparation:.....	13
1.2.4. Applications of G and GO: .....	14
1.2.5. Biological interaction and toxicity of G and GO: .....	15
1.3 Bisphosphonates .....	18
1.3.1. Nitrogen containing bisphosphonates: .....	19
1.3.2. Bioavailability of BP:.....	20
1.3.3. Pharmacokinetics of BP:.....	21
1.3.4. Alendronate sodium .....	21
1.4. Statement of purpose.....	22
<b>2. Literature Review .....</b>	<b>24</b>
2.1. LDH intercalated systems .....	24
2.1.1. Non Steroidal Anti-Inflammatory Drugs (NSAIDS) intercalated LDHs:.....	24
2.1.2. GO and drug intercalated LDHs:.....	26
2.2. GO based delivery systems.....	27
2.2.1. Delivery of anticancer drugs:.....	27
2.2.2. Delivery of active proteins:.....	29
2.3. Alendronate sodium delivery systems .....	30
<b>3. Theoretical Background.....</b>	<b>33</b>

3.1. X-ray diffraction (XRD).....	33
3.1.1. Principle of XRD: .....	33
3.1.2. Instrumentation of XRD:.....	37
3.2. Ultraviolet/Visible (UV/Vis) spectroscopy .....	38
3.2.1. Principles of UV/Vis spectroscopy:.....	38
3.2.2. Instrumentation of UV/Vis spectroscopy: .....	39
3.3. Fourier transform Infrared (FTIR) spectroscopy.....	41
3.3.1. Principles of FTIR: .....	41
3.3.2. Instrumentation of FTIR: .....	43
3.4. Scanning Electron Microscopy (SEM) .....	44
3.4.1. Principles of SEM: .....	44
3.4.2. Instrumentation of SEM: .....	45
3.5. Zetasizer analyzer .....	46
3.5.1. Principle of Zetasizer: .....	46
3.5.2. Instrumentation of Zetasizer:.....	49
<b>4. Materials and Methods .....</b>	<b>51</b>
4.1. Materials.....	51
4.2. Preparation of pristine LDHs .....	51
4.3. Oxidation of G powder .....	52
4.4. Preparation of G and GO/LDH hybrids .....	52
4.4.1. Determining the optimum GO weight percentage in the hybrid (%w/w): .....	52
4.4.2. Determining the optimum volume for the G and GO dispersion solutions for the preparation of the LDH-G and LDH-GO hybrids: .....	53
4.5. Loading of alendronate sodium.....	55
4.5.1. Co-precipitation:.....	55
4.5.2. Ion- exchange: .....	57
4.6. Characterization .....	58
4.6.1. Powder X-ray Diffraction (PXRD):.....	58
4.6.2. Fourier Transform Infrared Spectroscopy (FTIR):.....	58
4.6.3. Scanning Electron Microscope (SEM):.....	58
4.6.4. Ultraviolet/Visible (UV/Vis) spectroscopy:.....	58
4.6.5. Zetasizer analyzer .....	59



4.7. Determination of alendronate sodium loading.....	60
4.8. In- vitro drug release .....	60
<b>5. Results and Discussion.....</b>	<b>62</b>
5.1. Pristine LDHs.....	62
5.1.1. XRD: .....	62
5.1.2. FTIR: .....	64
5.1.3. SEM:.....	65
5.2. Oxidation of G powder .....	66
5.2.1. XRD: .....	66
5.2.2. FTIR: .....	67
5.2.3. SEM:.....	67
5.3. Preparation of G/GO-LDH hybrids.....	69
5.3.1. Determining the optimum GO weight percentage in the hybrid (%w/w): .....	69
5.3.2. Determining the optimum solution volume for the G and GO dispersion for the preparation of the LDH-G and LDH-GO hybrids: .....	70
5.4. Loading of Alendronate sodium .....	76
5.4.1. Co-precipitation samples:.....	76
5.4.2. Ion-exchange samples: .....	85
5.5. Determination of drug loading and release profile.....	95
5.5.1. Drug loading: .....	95
5.5.2. Drug release profile: .....	99
5.6. Summary of the work and results .....	102
<b>6. Conclusion and Future work .....</b>	<b>108</b>
6.1. Conclusion .....	108
6.2. Future work .....	109
<b>References.....</b>	<b>111</b>
<b>Appendix A: Calibration curves.....</b>	<b>123</b>

# LIST OF FIGURES

Figure 1-1.	Schematic representation of hydrotalcite three dimensional structure.	3
Figure 1-2.	G layer consists of two interpenetrated triangular sub-lattice in two different colors, the atom of one sub-lattice (A) is located at the centre of the triangle defined by the other sub-lattice (B).	11
Figure 1-3.	Structure of GO sheets.	12
Figure 1-4.	Coarse-grained molecular dynamic simulation of interactions between a lipid bi-layer, (A-D) represent the small G sheet, (E-H) represent interaction of larger multi-layered G.	16
Figure 1-5	The chemical structure of inorganic pyrophosphate and BP.	19
Figure 1-6	The structural activity relationship of BP.	19
Figure 1-7.	Pharmacological action of nBPs.	20
Figure 1-8.	The chemical structure of alendronate sodium in trihydrate form.	22
Figure 3-1.	Diagram of X-ray generation.	34
Figure 3-2.	Three dimensional unit cell.	35
Figure 3-3.	Parallel planes of atoms intersecting the unit cell.	36
Figure 3-4.	X-ray reflection from two parallel planes.	37
Figure 3-5.	The Bragg-Brentano geometry.	38
Figure 3-6.	Example of XRD chart.	38
Figure 3-7.	Schematic diagram of single-beam spectrophotometer setup.	39
Figure 3-8.	Schematic diagram of double-beam spectrophotometer setup.	40
Figure 3-9.	An example of a U.V spectrum.	40
Figure 3-10.	Changes in the dipole moments of a diatomic molecule.	41
Figure 3-11.	Stretching (a) and, bending vibrational (b) mode.	42

Figure 3-12.	Principle of FT-IR spectrometer operation.	43
Figure 3-13.	Illustration of the different signals obtained from hitting the sample specimen with the incident electron beam.	45
Figure 3-14.	Diagram of the scanning electron microscope (SEM).	46
Figure 3-15.	A screen with a speckle pattern of bright and dark areas.	47
Figure 3-16.	Correlation function of small and large particles over time.	48
Figure 3-17.	A typical size distribution graph.	48
Figure 3-18.	A schematic description of the Zetasizer analyzer.	49
Figure 5-1.	XRD patterns of Zn <sub>2</sub> -Cp (a), and Zn <sub>3</sub> -Cp (b).	63
Figure 5-2.	FTIR spectra of Zn <sub>3</sub> -Cp (a), and Zn <sub>2</sub> -Cp (b) pristine LDHs.	64
Figure 5-3.	SEM images of pristine Zn-Zl-NO <sub>3</sub> LDH.	65
Figure 3-4.	XRD patterns of G (a), and GO (b).	66
Figure 5-5.	FTIR spectra of G (a), and GO (b).	67
Figure 5-6.	SEM images of G (a), and GO (b).	68
Figure 5-7.	GO-LDH hybrids prepared with GO: 2 % (a), 6.2 % (b) and 13.4 % w/w (c).	69
Figure 5-8.	XRD patterns of G (a), Zn <sub>2</sub> -Cp (b), Zn <sub>2</sub> -G.04-Cp (c), Zn <sub>2</sub> -G.1 Cp (d), Zn <sub>2</sub> -G.2-Cp (e), and Zn <sub>2</sub> -G.4-Cp (f).	71
Figure 5-9.	XRD patterns of GO (g), Zn <sub>2</sub> -Cp (h), Zn <sub>2</sub> -GO.04-Cp (i), Zn <sub>2</sub> -GO.1-Cp (j), Zn <sub>2</sub> -GO.2-Cp (k), and Zn <sub>2</sub> -GO.4-Cp (l).	71
Figure 5-10.	XRD patterns of G (a), Zn <sub>3</sub> -Cp (b), Zn <sub>3</sub> -G.04-Cp (c), Zn <sub>3</sub> -G.1-Cp (d), Zn <sub>3</sub> -G.2-Cp (e), and Zn <sub>3</sub> -G.4-Cp (f).	72
Figure 5-11.	XRD patterns of GO (g), Zn <sub>3</sub> -Cp (h), Zn <sub>3</sub> -GO.04-Cp (i), Zn <sub>3</sub> -GO.1-Cp (j), Zn <sub>3</sub> -GO.2-Cp (k), and Zn <sub>3</sub> -GO.4-Cp (l).	72
Figure 5-12.	FTIR spectra of G (a), Zn <sub>2</sub> -Cp (b) Zn <sub>2</sub> -G.04-Cp (c), Zn <sub>2</sub> -G.1-Cp (d), Zn <sub>2</sub> -G.2-Cp (e), and Zn <sub>2</sub> -G.4-Cp (f).	74

Figure 5-13.	FTIR spectra of GO (g), Zn <sub>2</sub> -Cp (h), Zn <sub>2</sub> -GO.04-Cp (i), Zn <sub>2</sub> -GO.1-Cp (j), Zn <sub>2</sub> -GO.2-Cp (k), and Zn <sub>2</sub> -GO.4-Cp Cp (l).	74
Figure 5-14.	FTIR spectra of G (a), Zn <sub>3</sub> -Cp (b), Zn <sub>3</sub> -G.04-Cp (c) , Zn <sub>3</sub> -G.1-Cp (d), Zn <sub>3</sub> -G.2-Cp (e), and Zn <sub>3</sub> -G.4-Cp (f).	75
Figure 5-15.	FTIR spectra of GO (g), Zn <sub>3</sub> -Cp (h), Zn <sub>3</sub> -GO.04-Cp (i) , Zn <sub>3</sub> -GO.1-Cp (j), Zn <sub>3</sub> -GO.2-Cp (k), and Zn <sub>3</sub> -GO.4-Cp (l).	75
Figure 5-16.	XRD patterns of alendronate sodium (a), pristine LDH Zn <sub>3</sub> -Cp (b), and A-Zn <sub>3</sub> -Cp (c).	77
Figure 5-17.	XRD patterns of alendronate sodium (a), Zn <sub>3</sub> -G.04-Cp (b), A-Zn <sub>3</sub> -G-Cp (c), Zn <sub>3</sub> -GO.04-Cp (d), and A-Zn <sub>3</sub> -GO-Cp (e).	78
Figure 5-18.	XRD patterns of alendronate sodium (a), pristine LDH Zn <sub>2</sub> -Cp (b), and A-Zn <sub>2</sub> -Cp (c).	79
Figure 5-19.	XRD patterns of alendronate sodium (a), Zn <sub>2</sub> -G.04-Cp (b), A-Zn <sub>2</sub> -G-Cp (c), Zn <sub>2</sub> -GO.04-Cp (d), and A-Zn <sub>2</sub> -GO-Cp (e).	80
Figure 5-20.	FTIR spectra of A-Zn <sub>3</sub> -Cp (a), Zn <sub>3</sub> -Cp (b), and alendronate sodium (c).	81
Figure 5-21.	FTIR spectra of A-Zn <sub>3</sub> -G-Cp (a), Zn <sub>3</sub> -G.04-Cp (b), and alendronate sodium (c).	82
Figure 5-22.	FTIR spectra of A-Zn <sub>3</sub> -GO-Cp (a), Zn <sub>3</sub> -GO.04-Cp (b), and alendronate sodium (c).	82
Figure 5-23.	FTIR spectra of A-Zn <sub>2</sub> -Cp (a), Zn <sub>2</sub> -Cp (b), and alendronate sodium (c).	83
Figure 5-24.	FTIR spectra of A-Zn <sub>2</sub> -G-Cp (a), Zn <sub>2</sub> -G.04-Cp (b), and alendronate sodium (c).	84
Figure 5-25.	FTIR spectra of A-Zn <sub>2</sub> -GO-Cp (a), Zn <sub>2</sub> -GO.04-Cp (b), and alendronate sodium (c).	85
Figure 5-26.	XRD patterns of alendronate sodium (a), pristine LDH Zn <sub>3</sub> -Cp (b), and A-Zn <sub>3</sub> -IE (c).	86
Figure 5-27.	XRD patterns of alendronate sodium (a), Zn <sub>3</sub> -G.04-Cp (b), A-Zn <sub>3</sub> -G-IE (c), Zn <sub>3</sub> -GO.04-Cp (d), and A-Zn <sub>3</sub> -GO-IE (e).	87

Figure 5-28.	XRD patterns of alendronate sodium (a), pristine LDH Zn <sub>2</sub> -Cp (b), and A-Zn <sub>2</sub> -IE (c).	88
Figure 5-29.	XRD patterns of alendronate sodium (a), Zn <sub>2</sub> -G.04-Cp (b), A-Zn <sub>2</sub> -G-IE (c), Zn <sub>2</sub> -GO.04-Cp (d), and A-Zn <sub>2</sub> -GO-IE (e).	89
Figure 5-30.	FTIR spectra of A-Zn <sub>3</sub> -IE (a), Zn <sub>3</sub> -Cp (b), and alendronate sodium (c).	90
Figure 5-31.	FTIR spectra of A-Zn <sub>3</sub> -G-IE (a), Zn <sub>3</sub> -G.04-Cp (b), and alendronate sodium (c).	92
Figure 5-32.	FTIR spectra of A-Zn <sub>3</sub> -GO-IE (a), Zn <sub>3</sub> -GO.04-Cp (b), and alendronate sodium (c).	92
Figure 5-33.	FTIR spectra of A-Zn <sub>2</sub> -IE (a), Zn <sub>2</sub> -Cp (b), and alendronate sodium (c).	93
Figure 5-34.	FTIR spectra of A-Zn <sub>2</sub> -G-IE (a), Zn <sub>2</sub> -G.04-Cp (b), and alendronate sodium (c).	94
Figure 5-35.	FTIR spectra of A-Zn <sub>2</sub> -GO-IE (a), Zn <sub>2</sub> -GO.04-Cp (b), and alendronate sodium (c).	94
Figure 5-36.	A plot of the percentages of the drug loaded (% w/w) versus particle sizes (nm), to compare between the loading percentages, particle sizes and loading-size relationship, among samples prepared by same M <sup>2+</sup> /M <sup>3+</sup> ratio, 3:1 (blue) or 2:1 (orange), and between both ratios.	97
Figure 5-37.	A plot of the percentages of the drug loaded (% w/w) versus particle sizes (nm), to compare between the loading percentages, particle sizes and loading-size relationship, among samples prepared by same M <sup>2+</sup> /M <sup>3+</sup> ratio, 3:1 (green) or 2:1 (red), and between both ratios.	99
Figure 5-38.	Release profile of A-Zn <sub>3</sub> -Cp (blue), A-Zn <sub>3</sub> -G-Cp (red) and A-Zn <sub>3</sub> -GO-Cp (green).	100
Figure 5-39.	Release profile of A-Zn <sub>2</sub> -IE (blue), A-Zn <sub>3</sub> -IE (red).	101

# LIST OF TABLES

Table 1-1.	Ionic radii of some common divalent and trivalent metal cations.	4
Table 1-2.	Basal spacing values given by different intercalated anions in LDH.	5
Table 1-3.	pH values of precipitation of some $M^{3+}$ and $M^{2+}$ hydroxides.	6
Table 3-1.	Target materials used in X-ray tubes and their characteristic wavelengths.	34
Table 3-2.	Different shapes of unit cells and their possible axis systems.	35
Table 4-1.	G and GO/Zn-Al-NO <sub>3</sub> hybrids prepared with different concentrations of G and GO suspensions/solutions.	54
Table 4-2.	Intercalated systems with alendronate sodium prepared by co-precipitation.	55
Table 4-3.	Intercalated systems with alendronate sodium prepared by ion-exchange.	57
Table 5-1.	The lattice parameters, d-spacing and interlayer distances of Zn <sub>2</sub> -Cp and Zn <sub>3</sub> -Cp.	63
Table 5-2.	The calculated d-spacings and interlayer spaces of prepared G/GO-LDH hybrids, with different concentrations of G and GO (mg/ml) and metal cations ratio of LDH.	73

Table 5-3.	Comparison between the parameters of the loaded samples prepared by co-precipitation using a metal cations ratio of 3:1 and their controls.	78
Table 5-4.	Comparison between the parameters of the loaded samples prepared by ion-exchange, using a metal cations ratio of 3:1 and their controls.	87
Table 5-5	Comparison between the parameters of the loaded samples prepared by ion-exchange, using metal cations ratio of 2:1 and their controls.	89
Table 5-6.	The drug loaded amounts and particle sizes of samples prepared by co-precipitation using $M^{2+}/M^{3+}$ ratios 2:1 and 3:1 respectively.	96
Table 5-7.	The drug loaded amounts and particle sizes of samples prepared by ion-exchange using $M^{2+}/M^{3+}$ ratios 2:1 and 3:1 respectively.	98
Table 5-8.	Amounts and percentages of the drug released from 100 mg of hybrid system at 24 hr.	101
Table 5-9.	All prepared samples and their results with respect to the following aspects: drug loading mechanism, loaded amount (% w/w), and the total drug released at 24 hr (% of total load).	103
Table 5-10	Schematic presentation of the drug loading mechanism in all prepared loaded samples.	104

# **Chapter 1.**

## **Introduction**



# 1. Introduction

---

## 1.1 Layered double hydroxides

Layered double hydroxides (LDH) comprise a class of materials that can be either found as natural minerals in the soil, in sediments, as precipitants of saline water and hazardous waste sites, or could be synthetically prepared. They are used in a wide range of applications such as catalysis, filtration, drug or gene delivery, as exchangeable or absorbent materials, additives in polymer matrices or to create composites with other nanomaterials. These applications are based on the unique physical and chemical characteristics that LDHs possess such as high surface area, stability, large charge density, inertness, buffering effect, biocompatibility and great exchangeable capacity, in addition to the flexibility of controlling the surface layers and interlayer gallery content [1][2][3][4][5].

### 1.1.1. Structure of LDH:

LDHs are also known as mixed-metal-hydroxide anionic clays or hydrotalcite-like materials. Their structure is based on that of brucite [ $Mg(OH)_2$ ], which consists of Magnesium ions that are octahedrally surrounded by hydroxide ions. The octahedral units are connected end to end to form infinite layers and then these layers stack over each other to give a three dimensional structure. When a fraction of the divalent metal cations is substituted with trivalent cations, the hydroxide layers become positively charged. These positive layers are charge-balanced by the intercalation of anions in the interlayer gallery, which also contains water molecules, giving rise to Hydrotalcite, figure (1-1). Hydrotalcite was the first LDH discovered; it was introduced by Manasse in 1915, having a chemical formula of [ $Mg_6Al_2(OH)_2CO_3.H_2O$ ], and has been used as the reference term. After which Feitknecht in the late 1930s and 1940s introduced the term (Double sheet structure), describing a structure with intercalated hydroxide layers. And after the use of X-Ray diffraction for the study of minerals in the 1960's, Allman and Taylor had well understood the exact structure of LDH [1][3][5][6].

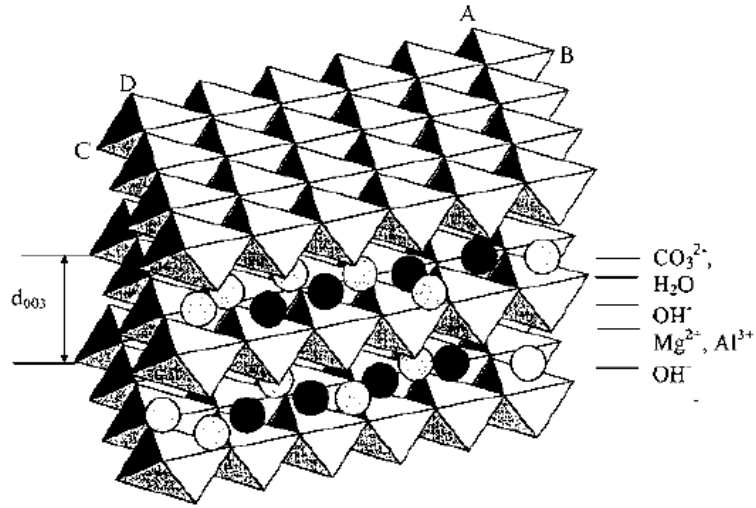


Fig 1-1. Schematic representation of hydrotalcite three dimensional structure [3].

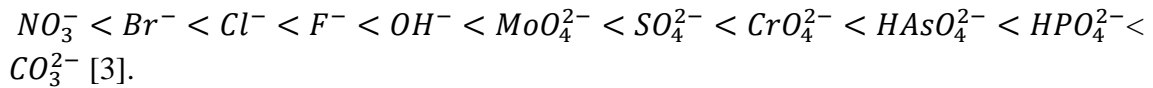
Different compositions of LDH materials are prepared by changing the type of divalent and trivalent cations as well as the interlayer anions, but still maintaining a general formula of  $[M_{1-x}^{2+}M_x^{3+}(OH)_{2x}]^{x+}(A^{n-})_{x/n}.mH_2O$ , where  $M^{2+}$  and  $M^{3+}$  are the divalent and trivalent metal cations in the hydroxide layers respectively. Pure LDH structures exist at values of  $x$  in the range of  $0.2 < x < 0.33$ , where  $x$  represents the metal ratio as  $M^{3+}/(M^{2+} + M^{3+})$  or in the range of 2-4 when expressed as  $M^{2+}/M^{3+}$  ratio. When the  $x$  value is higher than 0.33, an impure form of LDH is formed due to repulsion between the increased positive charge density of the trivalent metal ions, allowing the inclusion of foreign ions. For  $x$  values less than 0.2, the lower positive charge density allows for less anionic inclusion, which would prevent the formation of the metal hydroxide and the structure collapses [1][3][6].

There are a wide variety of divalent and trivalent metal cations to choose from, with different ionic radii as shown in table (1-1) [3]. The metals are chosen according to the proper ionic radius that can form the hydroxide layers, therefore the most preferential radii are the ones close to those of  $Mg^{2+}$  and  $Al^{3+}$  ions as in brucite for divalent and trivalent metal cations respectively [1]. The order of stability is  $Mg < Mn < Co \approx Ni < Zn$  for divalent metal cations, and  $Al < Fe$  for trivalent metal cations [1].

Table 1-1. Ionic radii of some common divalent and trivalent metal cations [3].

<b>M<sup>2+</sup></b>	<b>Radius (nm)</b>	<b>M<sup>3+</sup></b>	<b>Radius (nm)</b>
Fe	0.061	Al	0.054
Co	0.065	Co	0.055
Ni	0.069	Fe	0.055
Mg	0.072	Mn	0.058
Cu	0.073	Ga	0.062
Zn	0.074	Rh	0.067
Mn	0.083	Ru	0.068
Pd	0.086	Cr	0.069
Ti	0.086	V	0.074
Cd	0.095	In	0.080
Ca	0.100	Y	0.090
		La	0.103
V <sup>4+</sup>	0.058		
Ti <sup>4+</sup>	0.061	Li <sup>+</sup>	0.076
Sn <sup>4+</sup>	0.069	Na <sup>+</sup>	0.102
Zr <sup>4+</sup>	0.072		

While  $A^{n-}$  is the interlayer exchangeable anions, there is no limitation to the type of anions that could be incorporated within the interlayer galleries, as long as they compensate the positive charges of the hydroxide layers and generate purely prepared LDHs. Precautions are needed during preparation if using anions other than carbonates to prevent contamination with carbon dioxide from the aqueous solution or the surrounding environment. However, anions have different structures, radii (table 2-1), charges and charge densities that affect the basal spacing (interlayer distance + thickness of one brucite-like layer) or height of the LDH [3][6]. The charge density and bond strength are arranged in the following order:



The weaker bonded anions could be easily exchangeable with other strongly bonded anions that are favored to be taken by the positively charged hydroxide layers, this characteristic provides the LDHs with their exchange capacity property. Finally m is the number of water molecules in the interlayer gallery filling the unoccupied spaces made by the anions [1][2][3].

Table 1-2. Basal spacing values given by different intercalated anions in LDH [6].

<b>Anions</b>	<b>C'(A°)</b>
OH <sup>-</sup>	7.55
(CO <sub>3</sub> ) <sup>2-</sup>	7.65
F <sup>-</sup>	7.66
Cl <sup>-</sup>	7.86
Br <sup>-</sup>	7.95
I <sup>-</sup>	8.16
(NO <sub>3</sub> ) <sup>-</sup>	8.79
(SO <sub>4</sub> ) <sup>2-</sup>	8.58
(ClO <sub>4</sub> ) <sup>-</sup>	9.20

### **1.1.2. Preparation of LDH:**

Several synthetic techniques have been successfully used for the preparation of LDHs, and these include co-precipitation, classical ion- exchange and reconstruction techniques, with co-precipitation being the most simple, direct and commonly used among all techniques. There are other techniques such as sol-gel, salt oxide, hydrothermal and template methods and many others, but LDHs are not easily obtainable with these techniques and therefore not frequently used [3][4].

#### **A- Co-precipitation**

In this preparation method, the synthesis conditions should reach supersaturation for the metal cations to precipitate, which takes place by controlling the pH at a value higher than or equal to the value at which the most soluble hydroxide is precipitated. Table (3-1) shows the pH values at which some metal cations reach supersaturation to create the hydroxide layers. The co-precipitation reaction could take place either at low supersaturation or high supersaturation conditions. In the former case, two solutions are added simultaneously together, one containing a mixture of divalent and trivalent metal salts with the ratio of choice and the other containing an alkali to maintain the desired pH, all into an aqueous solution containing the desired interlayer anions, and the pH is maintained by either manual control or by using an automated titration device. The anion that is to be intercalated should be of higher affinity to LDH and in excess amount to compete with the anions of the metal salts. Therefore, the most commonly used anions in metal salt precursors are nitrates and chlorides due to their weak affinity for LDHs and thus could be easily replaced with others. However, the desired anion could be readily included in the metal salt precursors, and in this case the alkali is added directly into a

solution of the metal salt precursors till the desired pH is reached. In case carbonates are not the intercalating anions, precautions are to be taken by carrying the reaction under a nitrogen atmosphere, because of the high affinity of carbonates to LDHs. The advantages of the low supersaturation technique, are the capability to control the charge density of the hydroxide layers by controlling the pH, and the production of highly crystalline LDHs, that is for the increased rate of crystal growth rather than the rate of nucleation [1][3][4][6].

As for the case of high supersaturation, the mixed metal salt solution is added to an alkaline solution containing the desired interlayer anion in excess. However, this technique has some disadvantages such as the generation of less crystalline and impure LDHs due to the increased rate of nucleation at the expense of crystal growth, because of the continuous alteration in the solution's pH [1][3][4][6].

Table 1-3. pH values of precipitation of some  $M^{3+}$  and  $M^{2+}$  hydroxides [1][6].

<b>Cation</b>	<b>pH at <math>10^{-2}</math> M</b>	<b>pH at <math>10^{-4}</math> M</b>	<b>pH at which hydroxide re-dissolves</b>
$Al^{3+}$	3.9	8	9.0-12
$Cr^{3+}$	5.0	9.5	12.5
$Cu^{2+}$	5.0	6.5	
$Zn^{2+}$	6.5	8.0	14
$Ni^{2+}$	7	8.5	
$Fe^{2+}$	7.5	9.0	
$Co^{2+}$	7.5	9.0	
$Mn^{2+}$	8.5	10	

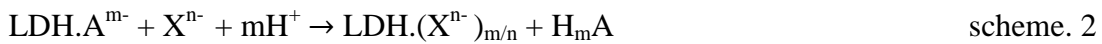
## B- Ion exchange

The ion exchange is another frequently used method when the co-precipitation technique is not applicable, such as when the divalent and trivalent metal cations or interlayer anions are unstable in alkaline media, or when the desired anions are difficult to intercalate by co-precipitation but rather favor direct anionic exchange. In this technique, the weakly held anions with low affinity to LDHs are exchangeable by the desired anions of higher affinity, depending mainly on the electrostatic interaction between the positively charged hosting sheets and the exchanging anions [1][3].

The exchange takes place by stirring the LDH precursors with an excess of the desired anion in a solution [1][3]. The exchange follows one of the two following schemes:



or



In the first scheme, the LDH precursors contain weakly bound anions such as nitrates, chlorides or perchlorates that are easily exchangeable with the anions to be intercalated. While the second scheme, which was firstly proposed by Bish, uses LDH precursors containing anions liable to acidic attack, such as carbonates and carboxylates [1].

There are some factors that should be considered for a successful ionic exchange; first, the affinity of the desired anion for the exchange, which increases with the increase of the ionic charges and the decrease of the ionic radii. Secondly, the solution medium for the exchange, the proper medium would allow the expansion of the LDH interlayer spacing for the exchange to take place. The aqueous medium favors the exchange by inorganic anions, while the organic medium favors the exchange by organic anions. The third factor is the pH of the medium, the low pH favors the exchange of less acidic anions with other more acidic anions from the solution, taking into consideration that at pH lower than 4 the LDH would begin to dissolve. And at last the effect of the divalent and trivalent metal composition in the hydroxide layers expressed as  $M^{2+}/M^{3+}$  ratio, since it affect the charge density of the sheets and the hydration state, and hence affect the exchange with the incoming anions. Other factors such as temperature also has an influence on the exchange, since temperature favors the exchange, but too high temperature would distort the LDH structure [1][7].

### C- Reconstruction

Reconstruction is another common preparation technique, also referred to as regeneration, restoration, rehydration, calcination-rehydration process or simply “structural memory effect”. In this technique the LDH is heated at a high temperature (calcined) to remove the interlayer anions, water molecules and hydroxyl groups, resulting in a mixed metal oxide. The calcined product is then rehydrated with water to regenerate the hydroxyl layers, and the interlayer anions and water molecules based on the memory effect of LDH. During regeneration, the anion of desire in the rehydrating water is incorporated into the interlayer gallery. The reconstruction process is greatly influenced by the pre-calcination temperature. For calcinations at temperatures less than or equal to 550 °C, the reconstruction is complete within 24 hrs, while for calcinations at 750 °C, reconstruction requires 3 days to be complete. At 1000 °C only partial reconstruction is observed. The advantages of this process is the ability to intercalate large guests that are difficult to intercalate by co-precipitation or ion-exchange and it ensures the absence of other competing anions such as the inorganic anions of metal salts. However, reconstruction is more complicated than co-precipitation and ion exchange and produces less crystalline LDH [8].

#### **1.1.3. Post treatment of prepared LDH samples:**

The synthesized LDHs are usually of poor crystallinity with disordered metal hydroxide layers. In the case of co-precipitation, the addition process of salt precursors and alkali is long enough for simultaneous nucleation and aging to take place, resulting in wide size distribution of crystals. Therefore, for an improved uniformity and crystallinity, the prepared precipitate is thermally treated at a temperature range of 273-373 K for few hours or days. The aging takes place via Ostwald ripening, by which large perfect crystallites grow and smaller ones disappear in the solution. Additionally, the produced precipitant should be washed thoroughly with deionized water to remove excess ions that may continue to react with the formed LDH [1][3][6].

#### **1.1.4. Precautions during LDH preparation:**

As mentioned previously, LDHs have very high affinity for carbonate anions, and in case it is not the desired anion, the reaction should take place under nitrogen to exclude atmospheric carbon dioxide. Atmospheric oxygen should be excluded as well, in case the metal cations in the hydroxide layers are liable to oxidation such as divalent manganese, cobalt, iron and trivalent vanadium [1][3].

### **1.1.5. Applications of LDH:**

As mentioned previously, LDHs have been employed in various applications in present and others expected in the future. Their properties can be easily tailored to fit the specifications of any required application. These properties are relevant to their high surface area, high exchange capacity; to intercalate various organic and inorganic guests, high adsorption capacity, thermal stability and reconstruction at mild conditions via “memory effect” [5][9].

LDHs are commonly known for their use in catalysis, in the form of precursors, supports, or as actual catalysts. In addition to their use as adsorbents and exchange materials for water treatment to capture organic and inorganic wastes, specially that they are thermally stable and able to regenerate [10]. The chemical inertness, biocompatibility and null toxicity of LDHs had increased their use in the biological field [2][5]. LDHs are very excellent intracellular carriers, that can efficiently penetrate cell membranes and deliver high amounts of biological molecules into the target cells [11]. They can be used to create either a direct or sustained release dosage forms or as a storage compartments for drugs that are unstable under the influence of sunlight and high temperature. They can protect from gastric ulcers that are caused by some drugs such as anti-inflammatories, because of their barrier property that are similar to that of gastric mucosa, and their acid buffering effect. They enhance the water solubility of some non polar or slightly polar drugs, increasing their bioavailability. LDHs are not limited to drug delivery, but include negatively charged bio-molecules as well, such as single or double stranded DNA and small nucleotide molecules to expand their use in gene therapy, biosensing or even information storage in future approaches [5][9][10].



## 1.2 Graphene

The first attempt to separate graphite layers was introduced by Boehm and co-workers in 1962 via chemical reduction of graphite oxide. In 2004, the thinnest layer unit of graphite, namely graphene (G), was discovered by Geim and co-workers; they received a Noble prize in physics for this discovery. Since then, thin layers of G have grabbed the attention for their exceptional properties, including high electrical conductivity ( $10^4$  S/cm), extraordinary mechanical properties with Young's modulus, Poisson's ratio and fracture strength of 1 TPa, 0.149 GPa and 130 GPa respectively, optical transparency, thermal conductivity ( $5000 \text{ Wm}^{-1} \text{ K}^{-1}$ ), high carrier mobility at room temperature ( $250,000 \text{ cm}^2/\text{Vs}$ ) with charge carrier concentration of  $1.4 \times 10^{13} \text{ cm}^{-2}$  and a huge surface area. These discoveries lead to exploring various means to incorporate G in applications such as in electronic and optoelectronic devices, as photoconductive materials in solar cells, in medical imaging, drug delivery, tissue engineering and as nano-fillers to improve the mechanical properties of some polymeric materials [11][12][13][15].

### **1.2.1. Structure of G:**

G is a building unit for other carbon-based structures, it is rolled into spheres, cylinders or stacked into layers to give fullerenes, nanotubes and graphite respectively [13][14][15][16]. However, the flat sheets of G have outstood these carbon allotropes for its unique properties and features [12].

G is a planar sheet of one-atom thickness ( $\sim 0.33 \text{ nm}$ ). It is composed of  $\text{sp}^2$ -bonded carbon atoms in two dimensional honeycomb Lattice. The unit cell of G lattice in real space comprises two carbon atoms belonging to two different interpenetrated sub-lattices, so that an atom from one sub-lattice is at the centre of the triangle defined by the other sub-lattice with a carbon-carbon inter-atomic length of  $0.142 \text{ nm}$ . This arrangement creates a triangular symmetry rather than a hexagonal one as shown in figure (1-2) [11][12][14]. Each carbon atom in the lattice has three  $\text{sp}^2$ -hybridized orbitals in the same plane, providing the G sheets with its mechanical stability, while the unhybridized p orbital is perpendicular to the molecular plane. The free delocalized  $\pi$  electrons of the unhybridized p orbitals create a high electronic density above and below the 2D G plane, providing it with a highly reactive surface that can immobilize a large number of substances such as metals, drugs, bio-molecules, fluorescent probes and cells [13][15][17].

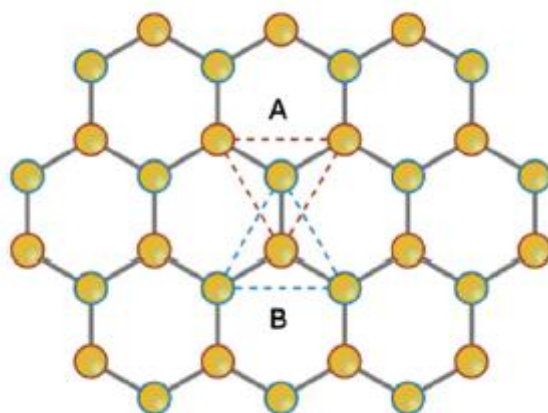


Fig 1-2. G layer consists of two interpenetrated triangular sub-lattice in two different colors, the atom of one sub-lattice (A) is located at the centre of the triangle defined by the other sub-lattice (B) [15].

Although G's unique properties are associated to its single plane sheet, it is difficult to obtain G as a defect-free single layer due to its high surface area. This leads to the formation of irreversible agglomerates or even the restacking of multiple layers via Van der Waals interaction to form graphite again. Therefore, there are many chemical attempts for graphite exfoliation that focus on intercalation, chemical derivatization, thermal expansion, oxidation-reduction and use of surfactants, in order to maintain the inherent properties of G, and to employ it in most of the proposed applications. These chemical attempts produce a set of structures referred to as "G family nano-structures", that include bilayer and multilayer G, graphene oxide (GO) and reduced graphene oxide (rGO), each one has its own surface chemistry, purity, defect density and compositions [11][12][13][14][18].

### **1.2.2. Graphene oxide:**

Surface functionalization of G sheets has been an efficient approach to prevent graphene's agglomeration by introducing small molecules in between layers. Graphene oxide (GO) has been the most widely used form of exfoliated graphite [12][13]. It is a highly oxidized form of G, prepared by strong oxidation of graphite followed by sonication or other dispersion methods to provide monolayer materials, and can be further modified chemically to obtain G-based materials with suitable properties for a specific application [15][19][20].

As shown in figure (1-3), the surface of GO sheets is highly oxygenated bearing epoxides, alcoholic groups, ketone carbonyls and carboxylic groups [15]. The carboxylate

groups at the peripherals provide colloidal stability and pH-dependent negative surface charges, while epoxide (-O-) and hydroxyl (-OH) groups are present on the basal plane, to allow for weak interactions such as hydrogen bonding and other surface reactions. The basal plane also contains free  $\pi$  electrons from the unmodified G areas, which are hydrophobic and can undergo  $\pi$ - $\pi$  interactions. When the carbon atoms covalently bond to these oxygen containing groups, they partially convert  $sp^2$  conjugated system to  $sp^3$ , weakening the van der Waals interactions between the sheets and increase the interlayer spacing of graphite from 0.35 nm to 0.65 nm to be ready for further exfoliation to single layers of GO. The oxidation and the harsh chemical treatments also impart topological defects, vacancies, cracks and edges in G lattice, increasing the chemical reactivity of the surface. The highly negative charged carboxylic and phenolic groups on the surface of GO render it hydrophilic due to their ionization in water to form uniform dispersions, which makes it very attractive for biological applications [13][14][15][18][21].

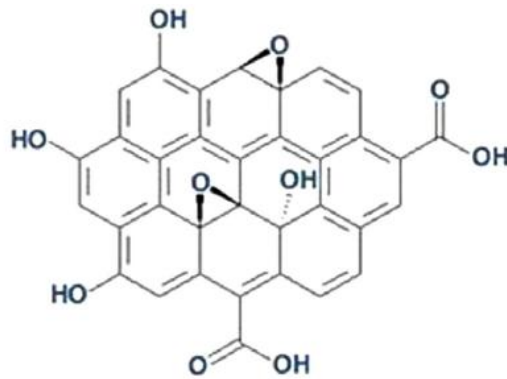


Fig 1-3. Structure of GO sheets [19].

### **1.2.3. GO preparation:**

The most common method used nowadays for the preparation of GO is the Hummers method that was developed by Hummers and Offeman in 1958. The method is very simple, fast and productive. It exposes graphite to strong oxidizing agents to introduce oxygen containing functional groups on both sides of the single graphite sheets [12][14][18][22][23].

#### **A- Hummers method**

The most suitable starting material is the expanded graphite flakes with an average diameter of ~15  $\mu\text{m}$ , because of its availability, cost effectiveness, and surface uniformity to provide a better oxidation and exfoliation performance [18][23].

In this method, oxidation is achieved by adding concentrated sulfuric acid ( $\text{H}_2\text{SO}_4$ ) into a mixture of graphite flakes and  $\text{NaNO}_3$ , all in an ice bath ( $0^\circ\text{C}$ ). This is followed by the addition of  $\text{KMnO}_4$  drop-wise to maintain the reaction temperature below  $20^\circ\text{C}$ , and then warmed to  $35^\circ\text{C}$ . At this temperature range, distilled water is slowly added producing an exotherm, and with the application of an external heat, temperature is maintained at  $98^\circ\text{C}$ . The reaction is then terminated with the addition of water and 30%  $\text{H}_2\text{O}_2$ . The final mixture is purified by sifting, filtering and successive washing with distilled water, 30%  $\text{HCl}$  and ethanol, with the repetition of sifting, filtration, centrifugation and decantation after each wash. Finally it is dried under vacuum at room temperature for 24 hrs [18][24].

There are some disadvantages to the Hummers method, such as the release of toxic gases like  $\text{NO}_2$  and  $\text{N}_2\text{O}_4$ , and the difficulty to remove the oxidation residues (i.e.  $\text{Na}^+$  and  $\text{NO}_3^-$ ) during purification. Moreover, it results in the production of GO with disrupted planes, because  $\text{H}_2\text{SO}_4/\text{HNO}_3$  mixtures act as chemical “scissors” and “drills” for the G planes to facilitate the diffusion of the oxidants [18][22]. Hence, some modifications have been introduced to create a more eco-friendly oxidation method, such as ‘modified Hummers’.

#### **B- Modified Hummers method**

In the improved method, 9:1 mixture of concentrated  $\text{H}_2\text{SO}_4 / \text{H}_3\text{PO}_4$  is added to a mixture of graphite and  $\text{KMnO}_4$ , producing a slight exotherm of  $35\text{-}40^\circ\text{C}$ . The  $\text{NaNO}_3$  is excluded in this method, which is the source of the toxic gases produced in the classic Hummers method, and is compensated for by increasing the amount of  $\text{H}_2\text{SO}_4$  and  $\text{KMnO}_4$ . The  $\text{KMnO}_4$  is a very strong oxidizing agent in acidic media; therefore, it improves the oxidation performance of  $\text{H}_2\text{SO}_4$ . The mixture is then heated to  $50^\circ\text{C}$  and stirred for 12 hours. After cooling to room temperature, the reaction is terminated by pouring the mixture into ice containing 30%  $\text{H}_2\text{O}_2$ . Followed by purification with sifting, filtration, centrifugation and decantation, and successive washing with distilled water,

30% HCl and ethanol. For each wash, the mixture is sifted, filtered, centrifuged and decanted then finally dried under vacuum at room temperature for 24 hours [18][22].

This improved method has some advantages over the unmodified Hummers, such as the low cost and oxidation temperature, it is less exothermic and produces no toxic gases, provides higher yield of GO with a less disrupted basal planes [18][24]. Therefore modified Hummers method is the most preferred approach for graphite oxidation.

#### C- GO reduction

GO has some limitations with respect to its mechanical, electrical and thermal properties; which are altered because of the functional groups that saturate the  $sp^2$  configuration. These groups disrupt the electronic structure, rendering the GO electrically insulating and reduce the charge-carrier concentration and mobility [12][13][14][21][25]. As for the mechanical properties, the Young's modulus is reduced to 0.15-0.35 TPa. In order to restore these properties, GO undergoes reduction to decrease the oxygen content via thermal, chemical or UV treatments in presence of hydrazine or other reducing agents [13][18][21][25]. However, it will not be fully restored due to the additional defects, that are introduced during the reduction process [17].

#### **1.2.4. Applications of G and GO:**

G has many unique properties that make it potentially promising in a large number of applications. The possibility of large scale production of GO and reduced GO has increased the opportunity for their use as reinforcements in polymer matrix composites. That is for their special mechanical, chemical, electrical and barrier properties, and aspect ratio [14][26][27]. These properties can contribute to exceptional features and high performance of the composite, such as gas and moisture barrier properties, electromagnetic shielding, electrical and thermal conductivity, increasing operating temperature level and improving compression strength [12][27].

Nowadays, there is an increased attention towards solar cells that use G as an active medium or as an electrode material, or taking the advantage of its chemical capabilities for energy storage and generation. The revolutionary in the electronics field has also utilized G as a planar channel material in high performance integrated circuits to produce touch screens, light emitting diodes and others [26][27].

However, G has recently expanded its range of applications to include biomedical ones such as in biosensors, tissue scaffolds, drug delivery, gene therapy or as antimicrobial agent. Such applications are made possible because of its relative properties such as large surface area, lateral dimensions, surface chemistry, purity and easy functionalization. It

can be a very promising ultrasensitive electrochemical or biological sensor [14][21][26][27]. Such sensing capability is made possible either via the charge transfer between the G monolayer and the adsorbed molecules, which is eventually translated into chemical responses, or via the functionalization of G with sensitive receptors for the detection of wide range of biological molecules (e.g. glucose, DNA, cholesterol and hemoglobin). In addition, it can serve as a single multi-dimensional measurement device. Moreover, in tissue engineering, the G's unique high elasticity and flexibility have been very promising for its use as a reinforcement for biocompatible films, hydrogels and other types of scaffolds [19][26][27][28].

As for drug delivery, GO disperses well in water and has a good stability in physiological solutions, in addition to a large surface area, making it a good candidate as a drug delivery vehicle that can be given for systematic targeting or local administration [12][21][29]. Its large exposed surface area allows the high loading of a large number of molecules ranging from small drug molecules to big molecules such as antibiotics, DNA, proteins and genes with a good distribution and release profile. The hydrophobicity of G and the untreated edges of GO have increased the loading options to include insoluble drugs via  $\pi$ - $\pi$  interactions and solving another challenge in drug delivery relevant to membrane barrier penetration [19][21][27]. Since the work here focuses on the biomedical applications, a great attention shall be given to its biological interactions, biocompatibility and the limitations for its uses.

### **1.2.5. Biological interaction and toxicity of G and GO:**

#### **A- Biological interaction**

The biomolecular interaction is responsible for the determination of cellular uptake, renal clearance, blood-brain barrier permeability and other biological phenomena and therefore, understanding the properties relevant to the interactions is important to control G's health and safety concerns [19][30].

The mechanisms by which graphene based materials (GBMs) interact with the cell's lipid bilayer, the layer that forms a barrier around all body cells, were introduced by Titov and coworkers. They conducted coarse-grained molecular dynamic (CGMD) simulation on G of different shapes, surface chemistries, different corners or edges, functionalizations and hydrophilic/hydrophobic property, in order to illustrate the dynamic process of G interaction with the lipid bilayer. In all cases the study agrees that G's cellular uptake or penetration takes place via spontaneous localized piercing of the membrane by the most hydrophobic and sharpest edges of G, followed by spontaneous tilting of the G's edges to

maximize its interaction to include the whole surface to achieve full penetration into the membrane interior as shown in figure (1-4). Therefore, the potential for G's interaction to the lipid bilayers is due to its extended two-dimensional surface (5-10 $\mu\text{m}$ ), hydrophobicity and sharp edges or protrusions, that are created during the fabrication and exfoliation processes. Whereas, GO is partially hydrophobic with rough edges and defects, that are produced during the harsh oxidation conditions, allowing it to interact as well with the lipid bilayers [19][30][31].

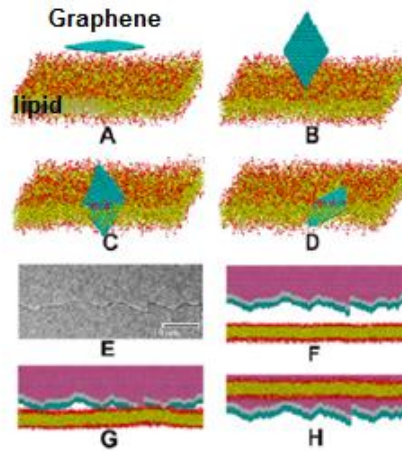


Fig 1-4. Coarse-grained molecular dynamics simulations of interactions between a lipid bilayer, (A-D) represent the small G sheet, and (E-H) represent interaction of larger multilayered G [30].

## B- Toxicity

The effect of GBMs on living systems is very versatile and inconsistent, due to the different fabrication techniques, sizes, shapes, surface charges and functional groups. All of these properties need to be standardized in order to understand the exact mechanism of GBMs toxicity and impact on human health. The effect of GBMs on living cells is generally dependent on their concentration, exposure time and administration route. GBMs given intravenously (I.V) and via inhalation are the most studied: they are found to accumulate mainly in lung, liver and spleen, causing inflammation, pathological changes and apoptosis to the cells [20][32][33][34]. The inflammation is assumed to be due to the release of the reactive oxygen species (ROS) as a defense response against the GBMs, that create a state of oxidative stress and damage the cells, but this mechanism is still unclear. However, the effect is greatly dependent on the given dose: in case of large doses equal or above 50  $\mu\text{g/ml}$  they are found to show an obvious toxicity, while doses below 20  $\mu\text{g/ml}$  fail to show any toxicity [14][32][33]. Size also plays an important role in evaluating the toxicity: sizes as small as  $160 \pm 90$  nm induce high toxicity effects and cell apoptosis at concentrations equal to 200  $\mu\text{g/ml}$ , while large sizes of  $780 \pm 410$  nm

have less toxic effects causing only slight necrosis, respectively. As for medium sized GBMs of  $430 \pm 300$  nm neither apoptosis nor necrosis is induced except for a decrease in cell viability at a dose of  $200 \mu\text{g/ml}$ . As for the studies made on GBMs that are administered orally are very limited. One of these studies detects the presence of large quantities of GBMs in the stomach and the intestines of mice within hours of ingestion, which were undetectable after one week, indicating their fast fecal excretion [14][20]. Another recent study has investigated the presence of G in the form of GO and other carbon nano-particles in the charred parts of roasted meat and in plant charcoal. This is used to prepare an approved medicine for infants' known as "grip water" to treat stomachaches. Hardly any incidents of toxicity have been discovered [35].

Current studies on GBMs toxicity, as claimed by researchers, are so far acceptable, and that the use of small doses may be safe. However, GBMs are more toxic in their free form and their modifications are still essential [34]. These modifications are to improve biocompatibility, solubility and reduce toxicity, and shall include all forms of G, even GO which is the most water soluble and biocompatible amongst all [20][31]. They can be modified with biocompatible, non-toxic materials either via covalent modifications such as atom doping and molecular interactions that further disrupt G's surface structure, or non-covalent modifications such as Van der Waals, H-bonding or electrostatic interactions which produce a more flexible structure without the alteration of their surface structure [17][32]. Examples of successful modifications are poly ethylene glycol (PEG) and dextran-functionalized G and GO that showed no significant toxicity or apoptosis to mice cells via I.V injection at a dose of  $20 \text{ mg/kg}$  or oral intake of  $100 \text{ mg/kg}$  of the mice's weight [33] .



### 1.3 Bisphosphonates

Bisphosphonates (BP) comprise a class of drugs that selectively prevent bone resorption (i.e. bone mass loss), and treat a number of bone diseases, such as menopausal osteoporosis, corticosteroid induced osteoporosis, Paget's disease, malignant hypercalcemia and metastasis, and other osteogenic imperfections [36][37].

They are analogues of the inorganic pyrophosphate: a cellular metabolic byproduct that inhibits crystallization and prevents calcification in connective tissues, urinary tract and other extracellular fluids via its strong binding affinity to mineral crystals. This activity affects the minerals' deposition inside the bone matrix and decreases its density. Therefore, to maintain the mineralization balance and allow for crystal growth, this action is reversed by alkaline phosphatase enzyme, which is present at the cellular linings; it hydrolyses the pyrophosphate before entering the bone and affecting the bone matrix. However, pyrophosphates do bind and promote the stabilization of formed crystals, and if allowed to saturate in the bone matrix, they may increase the crystal deposits and the bone density [38][39][40]. Therefore, non-hydrolyzable synthetic analogues such as the BP, have been developed for therapeutic purpose. As shown in figure (1-5), the chemical structure of BP comprises a carbon atom instead of oxygen which provides stability against hydrolysis by alkaline phosphatase, and it also allows for the presence of two more substituents/side groups than the phosphonate groups ( $R^1$  and  $R^2$ ). The binding strength and potency of BP can be easily tailored by varying  $R^1$  and  $R^2$  side groups respectively as shown in figure (1-6), which depicts their structure-activity relationship [36][37][38].

BP are classified into three generations based on the group at  $R^2$  position. The first generation lacks the nitrogen group such as clodronate and etidronate, the second generation has a primary nitrogen group such as alendronate and ibandronate, while the third generation contains a nitrogen group in a side chain cyclic ring as risedronate and zoledronate [41]. The potency of BP has been improving with each generation and nitrogen-containing bisphosphonates have proven to be the most potent generation and with the highest binding affinity to bone cells [42].

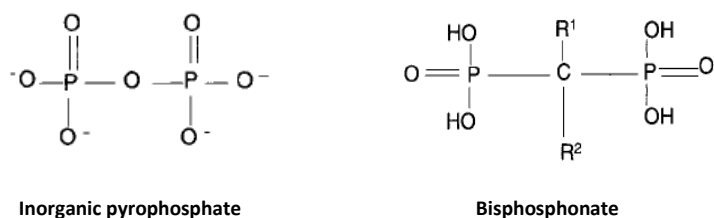


Figure 1-5. The chemical structure of inorganic pyrophosphate and BP [37].

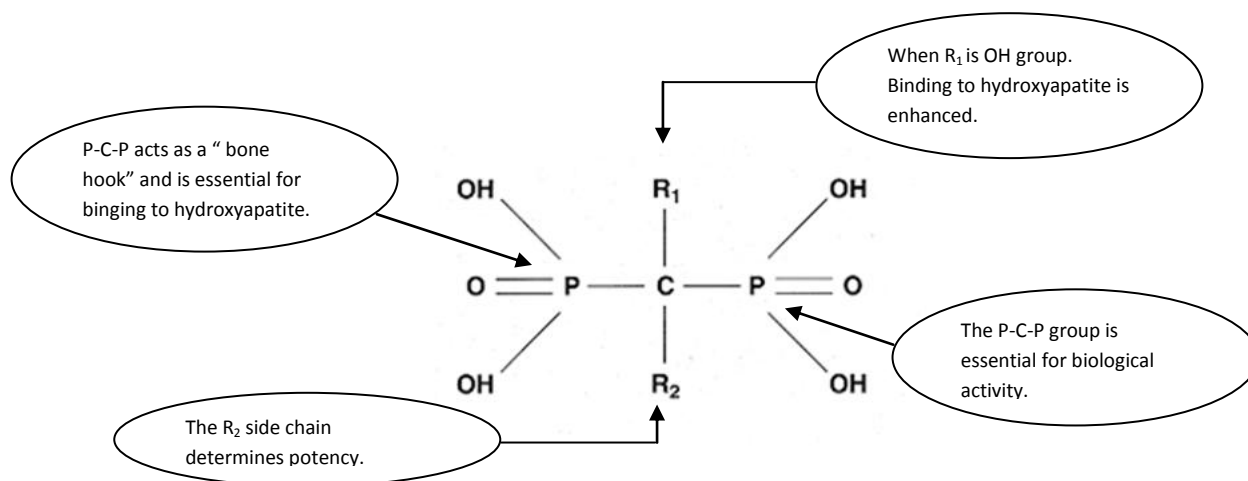


Figure 1-6. The structural-activity relationship of BP [36].

### 1.3.1. Nitrogen containing bisphosphonates:

As mentioned previously, the nitrogen containing bisphosphonates (nBP) are the most potent, because the  $\text{R}^2$  side chain plays an important role in the interaction of BP to the bone target and any slight change in the structure or conformation at  $\text{R}^2$  will dramatically affect the potency [39]. The nBPs' pharmacological effect is not only relevant to their capability to bind and stabilize the mineral crystals, but also they interfere with relevant metabolic pathways due to their structural similarities to active sites of some catalysts such as squalene; a biomedical intermediate for the synthesis of plant and animal sterols (ex. cholesterol). As shown in figure (1-7), they compete with squalene to interact with the farnesyl diphosphate synthase (FPP) in the mevalonate pathway. They therefore inhibit the FPP induced isoprenylation (i.e. the addition of hydrophobic groups to proteins to facilitate attachment to cell membranes) of some GTPase. This controls a number of activities in the osteoclasts' (bone cells that are responsible for resorbing bone minerals). The inhibition of farnesyl diphosphate synthase is dose-dependent: at low

concentrations, the mineral dissolution process is inhibited, at relatively high concentrations osteoclast differentiation is inhibited, while at very high concentrations osteoclast apoptosis (cell death) takes place [42][43].

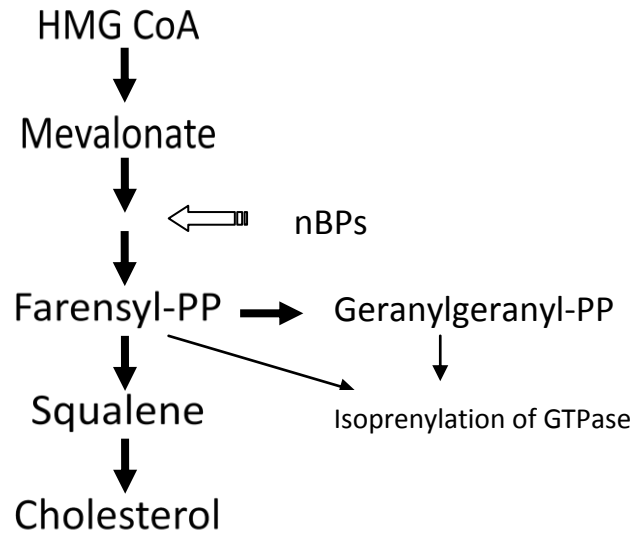


Fig 1-7. Pharmacological action of nBPs [42].

### **1.3.2. Bioavailability of BP:**

BP are administered either intravenously (I.V.) or orally. Although oral BP are more convenient for patients than I.V., they have poor oral bioavailability (<1%) and cause gastrointestinal adverse effects such as oesophagitis and diarrhea, which will need dose adjustments to increase efficacy or lead to discontinuation because of incompliance. They have low oral bioavailability because they are highly polar, negatively charged at physiological pH of the intestine, which lead to unfavorable transport across the epithelial barriers. Their absorption is also affected by food intake and calcium supplements, and despite their high bioavailability at higher pH, they are taken after an overnight fast to prevent food interference [36][41][44][45].

### **1.3.3. Pharmacokinetics of BP:**

The oral absorption of BP across the gastrointestinal tract takes place paracellularly (i.e. passage of molecules between tight junction of the cells), because of their low transport efficiency across the epithelial cells as mentioned previously. The absorbed dose is then distributed equally between the bone from which the drug is slowly released and the kidney for excretion. The amount of drug retained in the bone is partitioned between two drug pools: one at the bone resting surface where the drug is mobilized during the bone turnover into the bone fluid then into the blood, and the other partition is buried deep in the bone matrix. The drug mobilized into the blood is recyclable again into the bone and kidney till the amount is insufficient, while the drug embedded inside the bone remains active until resorption is induced by the newly formed osteoclasts, and that is when an additional dose has to be given to maintain the anti-resorptive efficacy. Although the usual administered doses shows a plateau for the resorption suppression, a higher or more frequent doses are recommended for higher efficiency [37][36][42].

### **1.3.4. Alendronate sodium:**

Alendronate sodium [(4-amino-1-hydroxybutylidene)bisphosphonic acid Monosodium Trihydrate] (figure 1-8), a water soluble nBP. It is the most efficient anti-resorptive agent and potent farnesyl diphosphate inhibitor to-date, and it is the drug of choice in the treatment of hypercalcemia in malignancy cases, postmenopausal osteoporosis and many other musculoskeletal disorders. Its clinical effect is based on increasing bone mineral density and strength, and reducing risk of fracture. Its mechanism of action, bioavailability and pharmacokinetics data are similar to the nBPs. It shows an oral bioavailability averaged 0.75%, with a linear oral absorption increase from 5 to 80 mg dose range. As a result of the addressed issues, many attempts have been made in order to develop new formulations for the alendronate sodium to enhance its bioavailability [37][45][46][47].

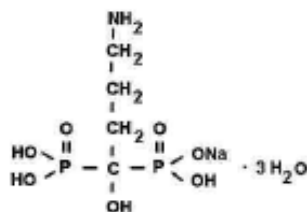


Fig 1-8. The chemical structure of alendronate sodium in trihydrate form [37].

## 1.4. Statement of purpose

The aim of this research work is to prepare a new hybrid nanocomposite of G/GO-LDH, and investigate its use as a drug delivery system for nitrogen containing bisphosphonate (alendronate sodium), this entails:

- Preparation of a hybrid nanocomposite of Zn-Al LDH in its nitrate form with G/GO (G/GO-Zn-Al-NO<sub>3</sub>) using two different M<sup>2+</sup>/M<sup>3+</sup> ratios of LDH (2:1 and 3:1).
- Loading the hybrids with the alendronate sodium with two different techniques: co-precipitation and ion-exchange.
- Characterization of the samples by XRD, FTIR to determine successfully intercalated samples, and mechanism of loading.
- Determination of the loaded drug amounts and the study of the drug release from the hybrids by UV spectroscopy.
- Compare the performance of the hybrid nanocomposite samples with LDH control with respect to drug loading and release.

# **Chapter 2.**

## **Literature Review**

## 2. Literature Review

---

This chapter presents a review of the different approaches that have been developed to improve the delivery of pharmaceutically active molecules, with emphasis on those based on the utilization of LDH and GO as drug delivery platforms. A number of delivery systems that were investigated for improving the unfavorable physiochemical properties of alendronate sodium will also be represented.

### 2.1. LDH intercalated systems

#### **2.1.1. Non Steroidal Anti-Inflammatory Drugs (NSAIDS) intercalated LDHs:**

NSAIDS anti-inflammatory drugs, are commonly used in cases of arthritic rheumatism, osteoarthritis, muscle pain, metastatic bone pain, migraines and many other medical cases. However, they are associated with low solubility, poor delivery control and administration adverse effects; such as gastric and duodenal ulcers. Intercalation of NSAIDS into the LDH matrix, has improved their water solubility and release rate. The LDH has provided an additional advantage by introducing a buffering effect to protect against the ulceration damages [48][49].

The anti-inflammatory fenbufen was intercalated by Evan et al. into Mg/Al and Li/Al LDHs in their nitrate form by co-precipitation under pH 8 [50]. The drug was intercalated successfully as monolayers in the LDH interlayer gallery, and upon increasing the pH from 8 to 12, the amount of intercalated fenbufen was increased, indicating the possible formation of bilayers as suggested by the increased gallery spacing. The Mg/Al LDH system proved to be more effective as a controlled release system, giving a gradual release over time compared to Li/Al LDH [48][50].

Del Arco et al. intercalated fenbufen into Mg/Al LDH and Mg/Al/Fe LDH systems, by co-precipitation and ion exchange, using the chloride LDH form, and by reconstruction using the LDH nitrate form [51]. The intercalation was successful in case of Mg/Al LDH by the three preparation techniques, but fenbufen was only intercalated by co-precipitation and ion exchange in case of Mg/Al/Fe LDH. This was because Fe inhibited the intercalation after the LDH reconstruction. The total drug release was more restrained in case of the Mg/Al/Fe LDH system (only 59% in 1 h), due to the strong interaction between the drug and the hydroxide layers, while the release from the Mg/Al system was complete in only 2 h [48][51]. The study was extended by coating the LDH-drug hybrid

with an enteric coat such as Eudragit® S100, and uniform and smooth microspheres were produced, showing high stability at low pH (<7) [51]. The same results were found by Evans et al., who proved that the strong interaction between the Eudragit® S100 and the LDH further restrained the drug release [48].

Naproxen is another anti-inflammatory that was successfully intercalated by Duan et al. into Mg/Al LDH in its nitrate form by ion exchange under pH 8. The study proved the thermal stability of the system. This was acquired by the naproxen upon intercalation compared to the free form, suggesting an additional advantage of the LDH as a promising delivery system [48][52].

Berber et al. also intercalated the naproxen into Mg/Al LDH by co-precipitation and reconstruction with the LDH chloride form at pH 8. The drug was intercalated more successfully by co-precipitation than by reconstruction, and the drug dissolution in the acidic media was improved compared to the free drug. The same approach was followed by Del arco et al. using the three preparation techniques. The intercalated amount of naproxen was almost the same in case of co-precipitation (44.2%) and ion exchange (46.5%), but very low in case of reconstruction (38.4%) due to possible contamination with interlayer carbonates. The drug dissolution was improved in acidic medium, compared to the free drug and the release was found to be more controlled [48][53][54].

The Zn/Al LDH system was used by Hou and Jin to intercalate naproxen by the ion exchange method [48][55]. The intercalation of the drug was successful, and the interlayer distance increased to 18.78 Å, which is greater than the drug's height (12.20 Å), indicating the arrangement of the drug as overlapped bilayers and high drug loading. They studied the effect of some variables such as the structural charge density, composition and the pH on the amount of the drug loaded, in addition to the effect of using LDH on the drug release rate. The increase of the charge density increased the amount of the drug loaded because of the interaction between the positively charged LDH layers and the negatively charged naproxen. On the other hand, the increase of pH from 6 to 11 caused a linear decrease in the amount of loaded drug, because the charge density decreased with the increase of pH [55]. The composition of the interlayer anions were also of significance, both chlorides and carbonates were investigated as the interlayer anions. It was found that the intercalation was more successful in the case of chlorides because it was more readily exchanged with drug. Finally, the Zn/Al LDH was proved efficient as a controlled release system when compared to free naproxen [48][55].

Ambrogi et al. successfully intercalated the anti-inflammatory ibuprofen and diclofenac in Mg/Al LDH with its chloride form by ion exchange, suggesting their arrangement as monolayers and bilayers respectively, which was indicated by the increased value of the interlayer space compared to the drugs' molecules sizes. They investigated the LDH



capability to control the release of the drug. It was found that the release of ibuprofen and diclofenac in the phosphate buffer solution took place over 24 hours, the slow release being attributed to the rate of phosphate anions' diffusion onto the interlayer gallery and their exchange with the intercalated drug [48][56][57]. They extended their work to prepare enteric-coated microparticles of diclofenac-LDH to protect against gastric attack. The microparticles were prepared by an oil-in-oil solvent evaporation method, using the intercalated LDH and a mixture of Eudragit® S100 and Eudragit® L100 polymers with a ratio of 1:5 or 1:10 w/w. The microparticles combined between the two release strategies: the pH-dependent polymer solubility and the ion exchange release mechanism of the LDH [48][58].

Perioli et al. used the Zn/Al LDH with its bromide form to intercalate diclofenac drug, using the ion exchange mechanism. After the successful intercalation, they studied the effect of the particle size on the drug release [48][59]. The release of the drug from the nano-sized and micro-sized particles were compared, showing no difference of their release and indicating that the ion exchange was the rate-limiting step [59].

Rives et al. intercalated diclofenac and ketoprofen into Zn/Al and Mg/Al LDH systems with its nitrate form by co-precipitation. The increased height of the interlayer gallery in case of the two drugs is 23 Å, and when compared to the drugs' molecular sizes, suggested their arrangement as tilted bilayers. The strong interactions between the drug and the LDH layers proved to be another indication to the thermal stability of the intercalated drug at very high temperature compared to its free form [48][60].

### **2.1.2. GO and drug intercalated LDHs:**

The first attempt for the use of GO/LDH hybrid in biological systems was reported by Zhang et al. (2012). Their objective was to prepare antibiotic-intercalated LDH-GO composite by a simple solvent evaporation method. The delivery system combined the antibacterial activity of GO and its ability to incorporate a variety of drugs, and the LDH's ability to store the drug and control its release. A Mg-Al LDH, with nitrate as the interlayer anion, was used as a precursor into which the benzyl penicillin (BP) antibiotic was intercalated by ion exchange. The as-prepared BP-LDH was then mixed with GO under vigorous shaking and ultra-sonication, relying on the formation of electrostatic interactions between GO and LDH, followed by washing and drying completely. The release of the drug from the hybrid was much slower than that of free LDH and could be adjusted by controlling the GO/BP-LDH ratio: the lower the ratio of GO/BP-LDH the higher the time of the release. As for the biological activity, the hybrid was observed to

show a synergistic antibacterial effect, due to the combined antibacterial activity of the BP and GO, which also increased with the decrease of the GO/BP-LDH [61].

## 2.2. GO based delivery systems

### **2.2.1. Delivery of anticancer drugs:**

The use of chemotherapeutic drugs to treat cancer is challenged by their non-selective cytotoxicity and hydrophobicity, which has imposed the need to develop efficient targeted drug delivery systems [47]. GO serves as a promising drug delivery vehicle as its high surface area is available for variable dynamic interactions with different biomolecules and drugs [62][63].

In 2008, Dai et al. pioneered the development of a modified GO for biological applications. Six-armed polyethylene glycolamine polymer (PEG) was grafted onto the surface of GO to impart biocompatibility and aqueous stability without aggregation. The GO-PEG hybrid was then loaded with the anti-cancer doxorubicin (DOX) via  $\pi$ - $\pi$  stacking and hydrogen bonding at high loading capacity. The PEG shell gave the drug high stability during blood circulation till it reached the tumor, where the drug was released due to its increased solubility in acidic media [63][64]. The tumor-targeting of the GO-PEG-DOX system was based on the fact that the tumor microenvironment is acidic (pH 5.5). On the other hand, PEG acts as a diffusion barrier that can adversely delay the release of the drug. In 2012, Shi et al. solved this issue by developing a GO delivery system with a redox-responsive detachable PEG shell. A cytamine modified PEG (PEG-SS-NH<sub>2</sub>) was grafted onto the surface of GO via the disulphide linkage (NGO-SS-mPEG) [65]. The encapsulated drug was rapidly released from the formulation by selective degradation of the disulphide linkage when exposed to the relevant levels of reductive glutathione (GSH) at the tumor site, imparting higher intracellular concentration of the drug, and consequently increasing the inhibition of cell proliferation [63][65]. Later, Ji et al. developed a simpler method for the preparation of the same hybrid system. The PEG-SH was conjugated to GO-SH via disulphide linkage by using only air as an oxidizing agent. Moreover, they conducted a comparative study of the intracellular drug release and cytotoxicity between NGO-SS-PEG/DOX and NGO-PEG/DOX, to prove that the rapid release of the drug from the NGO-SS-PEG conjugate with a detachable PEG shell was very specific to the tumor's relevant GSH levels, therefore, it showed higher therapeutic effect than that of NGO-PEG. They also reported GO-SS-PEG/DOX as an efficient chemo-photothermal therapy, by demonstrating the effect of photothermia on the release of DOX from both hybrid formulations. The results showed an accelerated release of DOX in the case of NGO-SS-PEG/DOX by heat and hence, the disulphide linkage breakdown [66]. Liu et al., created the 3D version of the

redox-responsive PEGylated G nanocarrier (GON-Cy-ALG-PEG) for the delivery of the anti-cancer DOX. It was prepared by conjugating cytamine modified PEGylated alginate brush to GO, via disulphide linkage. The system succeeded to achieve a targeted delivery of DOX to the tumor site, showing very high cellular uptake, with no obvious toxicity up to 200µg/ml. However, it was recently reported that the disulphide linkage of the detachable PEG shell was also susceptible to degradation by enzymes, which led researchers to take alternative strategies [63].

Gan et al. reported a novel nanocarrier, by covalent functionalization of GO with chitosan (CS). CS is a natural polysaccharide, which is biocompatible and serves as a low immunogenic drug carrier. Its solubility is affected by pH changes: it is poorly dispersible in alkaline pH, but forms homogenous dispersions in acidic pH, which was relevant to the release mechanism of the drug from the GO-CS carrier as a response to the acidic environment of the tumor [63][67]. The GO-CS was demonstrated as a drug carrier for water-insoluble anti-cancer camptothecin, exhibiting a very high aqueous stability and a loading capacity of 20 % (w/w), which was twice that reported in the case of PEGylated GO. The carrier also proved to be non-toxic to healthy cells and with remarkable cytotoxicity to tumor cells [67]. To further increase the targeting property of the GO-CS carrier, Yang et al. incorporated folic acid (FA) to the chitosan carrier (FA-CO), as a targeting molecule for tumor cells with over-expressed folate receptors on their surface. The cellular uptake of DOX was very high when compared to GO-CS [68]. Tang et al. prepared the same hybrid, but in a one-step preparation method. The composite was prepared by combining GO, folic acid and trimethylchitosan (TMC) in a single system to prepare a modified FA with TMC (FTMC), which spontaneously conjugated with GO via self assembly [69].

FA functionalized GO was prepared by Lin et al. by a one-pot synthetic technique, taking the advantage of the self-polymerization of Dopamine (DA). The anti-cancer DOX and the targeting molecule (FA) were immobilized simultaneously during the polymerization on the GO surface, the polymerization was controlled by only pH adjustment and excluding any chemicals or organic solvents; hence this represented a simple, low cost and eco-friendly approach. A 100% loading capacity of the active DOX was achieved, and was released in a sustained manner depending on the dissociation of the H-bonds between GO and DOX [47].

Wu et al. functionalized GO with a different targeting molecule: hyaluronic acid (HA), which is a natural polysaccharide that exists in cellular matrix, connective tissues and body fluids. The hybrid (GO-HA) selectively targeted the delivery of DOX to tumor cells via receptor-mediated endocytosis through receptors such as cluster determinant 44 (CD44) and receptors for hyaluronic-mediated motility, which are highly expressed in tumor tissues. The delivery efficiency was proved by the significant tumor suppression after intravenous injection of mice by 40% and with no significant toxicity or

inflammatory reactions [70]. Song et al. prepared the same hybrid, but instead of loading the DOX onto the prepared GO-HA as in the previous work, the GO was first loaded with DOX via  $\pi$ - $\pi$  stacking and H-bonding, and then conjugated to HA via H-bonding, achieving a loading efficiency of 42.9% and an entrapment efficiency of 69.5% [62].

### **2.2.2. Delivery of active proteins:**

The role of proteins in regulating gene expressions and cellular signals pathways, justifies their potential in cancer therapy. Protein-based therapy has many advantages over the conventional chemotherapy, such as less side effects and less immunogenicity. However, the poor cellular uptake and enzymatic hydrolysis have restricted the use of active proteins in biotherapy. Zhang et al. demonstrated the use of GO functionalized with PEG (GO-PEG), that was previously developed by Dai et al., as a vector for the delivery of active proteins; GO protected the protein from enzymatic hydrolysis and retained its activity till it reached the cells. In this study the GO-PEG was loaded with bovine serum protein (BSA) as a model protein via physisorption to investigate the loading and release behavior. The loading capacity was very high, which was attributed to the high loading surface of GO, with a gradual release of the protein in phosphate buffer solution. As for the stability of the proteins, the GO-PEG/protein complex was investigated versus free protein in presence of digesting enzymes. The complex showed an intact protein, owing to the steric hindrance created by the GO that prevented the digesting enzymes to reach the protein [71].

A different strategy for the delivery of proteins was established by Park et al. A pH-sensitive poly(acrylic acid) (PAA) polymer was grafted to GO surface by in situ radical polymerization to create GO-PAA for the oral delivery of protein in their active form without being degraded. The PAA is a weak anionic polyelectrolyte polymer that is greatly dependant on the surrounding pH: the polymer was protonated at low pH of the upper GIT, causing its shrinkage and protein retention, while at high pH of the intestine it was deprotonated, and swollen by the electrostatic repulsion between the chains, allowing the protein to be released. This complex provided both high loading capacity and protection of the protein via the pH-dependant behavior of the polymer [72].

### 2.3. Alendronate sodium delivery systems

A few approaches were adopted to overcome the unfavorable physiochemical properties of alendronate sodium, such as poor membrane permeability and esophageal irritation. One of such approaches was based on the use of liposomal nanoparticles as a delivery system. The liposome improves the membrane adhesion, permeability and absorption of hydrophilic drugs, but due to its instability against chemical and enzymatic degradation in the intestine, Han et al. coated its surface with chitosan. The positive charges of chitosan created a shield around the liposome preventing acids or enzymes from reaching the liposome's surface, and providing an additional advantage by decreasing the drug's leakage and minimizing contact with the esophagus. The chitosan also interacted with the negatively charged mucus layer of the intestinal epithelial cells, increasing its resident time in the intestine and hence its oral absorption and bioavailability [73].

Enteric coating of the liposomes is another technology that protects against gastric and enzymatic attack. Hosny et al. prepared the enteric coated liposomes: first the liposomes were prepared from a mixture of phosphatidylcholin, cholesterol and lecithin, with the mass ratio of 4:3:1 to achieve the highest encapsulation efficiency (49.39%), integrity and stability, and then the poly(meth)acrylate (Eudragit<sup>®</sup> S100) was added to impart enteric coating. To further enhance the liposomal stability, a negatively or positively-charged enhancer such as stearylamine (SA) and dicetyl phosphate (DO) respectively, were mixed with the liposomal lipid components. The positively charged enhancer (SA) was found to increase the encapsulation efficiency due to the attraction force between its positive charges and the negatively charged alendronate sodium. In the case of the negatively charged enhancer, there was a repulsion force with the negatively charged drug, however, it had an attraction force with the Eudragit positive charges, improving its coating efficiency and showing more resistance to the gastric and enzymatic attacks. Therefore, the negatively-charged enteric-coated liposomes were shown to have optimum features allowing for high bioavailability and protection against esophageal irritation [74].

Polymeric micro particles were also among the systems used to overcome the gastrointestinal adverse effects associated with alendronate sodium oral intake. Cruz et al. prepared polymeric micro-particles by spray drying of alendronate sodium with poly(meth) acrylate (Eudragit<sup>®</sup> S100) and another with a blend of Eudragit<sup>®</sup> S100/methyl cellulose, with mean diameter below 17  $\mu\text{m}$ . Both formulations of micro particles had high encapsulation efficiency, and showed a slow release of the drug, with more delay in presence of methylcellulose. As a consequence of delayed release, the gastrointestinal injuries were almost diminished [46].

The potentials of solid lipid nanoparticles (SLNs) such as high drug loading, drug stability and low toxicity have recently increased their use as a drug delivery system for different administration routes. The SLNs have a lipid matrix that can incorporate hydrophobic as well as hydrophilic drugs, and alendronate sodium were demonstrated by Hadi et al. as the drug model. The alendronate sodium loaded SLNs were prepared by simple hot homogenization technique: emulsification followed by solidification without the use of organic solvents. Very high encapsulation efficiency (70-85%) was achieved, and a sustained release of the drug was also achieved owing to the solid matrix of the nanoparticles [75].

# **Chapter 3.**

## **Theoretical Background**

## 3. Theoretical Background

---

This chapter presents the theories behind the characterization and the analytical techniques used in this work, and which includes X-ray diffraction (XRD), Scanning electron microscopes (SEM), Ultraviolet/Visible (UV/Vis), Fourier Transform Infrared (FTIR) spectroscopy and Zetasizer analyzer.

### 3.1. X-ray diffraction (XRD)

X-rays were discovered by the physicist Wilhelm Röntgen in 1895, followed by Gordon Darwin in 1912 who established the dynamic theory of X-ray scattering by a crystal lattice. X-rays are electromagnetic radiations that lie in between gamma and ultraviolet radiations in the electromagnetic spectrum. They have a wavelength range of 0.1-100 Å, which is almost in the same range as that of the size of atoms, making them eligible for studying and characterizing materials at the atomic level. XRD is used to obtain structural information of crystalline samples such as unit cell lattice parameters, crystal phase composition, degree of crystallinity, residual stress, texture and orientation [76][77][78]. To have a complete understanding of the technique, some important principles are to be discussed first.

#### **3.1.1. Principle of XRD:**

##### A- X-ray generation

X-rays are electromagnetic radiations that occur whenever an electric charge accelerate or decelerate. The wavelength used for the crystallographic detection is 0.5-2.5 Å, which is associated with very high energy that enables the X-rays to penetrate through the sample and detect the smallest inter-atomic distances, and that what makes it a very powerful detection tool. Figure (3-1) is a Bohr model of an atom to explain the generation of X-rays. The nucleus is surrounded by shells hosting electrons, and when a beam of electrons hits the target material at a very high speed, an electron in an inner shell (K-shell for example) is ejected, leaving behind a positive hole which is then filled by an higher energy electron (from the L or M shells for example). This electronic transition produces two types of X-rays known as:  $K_{\alpha}$  X-rays which are of very high intensity, and  $K_{\beta}$  X-rays



which are of lower intensity.  $K_{\alpha}$  and  $K_{\beta}$  reflect the transitions of electrons from L- to K-shell and from M- to K-shell respectively, and are very characteristic of the atomic structure of the target material [77][79]. Table (3-1) shows the commonly used target materials and their wavelengths.

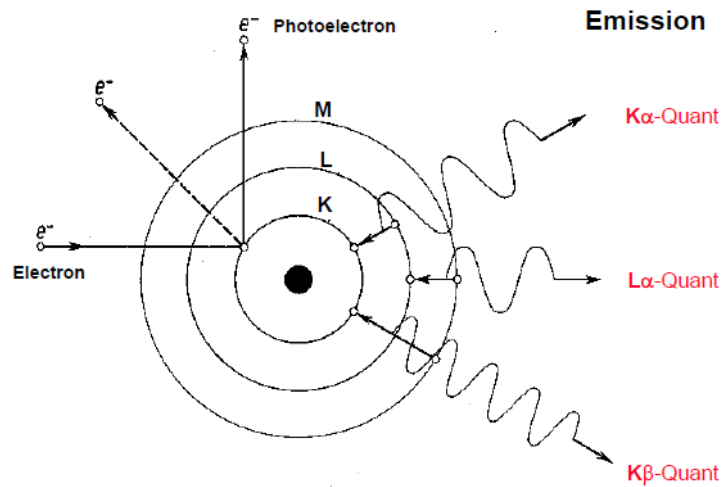


Fig 3-1. Diagram of X- ray generation [70].

Table 3-1. Target materials used in X-ray tubes and their characteristic wavelengths [79].

Element	Wavelength (Å)
Mo	0.7107
Cu	1.5418
Co	1.7902
Fe	1.9373
Cr	2.2909

### B- Crystals

Solid matter is classified into amorphous and crystalline solids. Amorphous solids lack order in the arrangement of their units, which can be atoms, ions or molecules. On the other hand, crystalline solids, which represents 95% of all solid materials, have their units arranged in periodic arrays with long-range order. The unit cell is the smallest volume

element, when repeated in three dimensions, defines the crystal structure. The unit cell is described by three main axes: a, b and c where  $\alpha$ ,  $\beta$  and  $\gamma$  represent the angles in between, as shown in figure (3-2). The variation in these parameters gives rise to seven different shapes of unit cells as in table (3-2) [76][78][80].

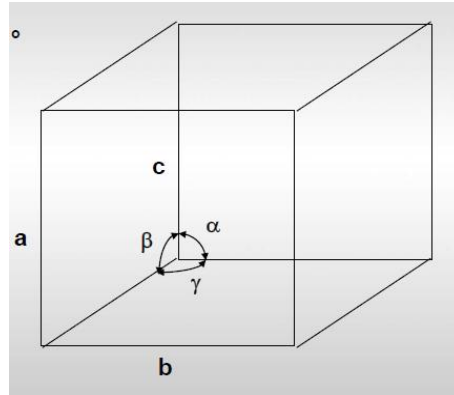


Fig 3-2. Three dimensional unit cell [76].

Table 3-2. Different shapes of unit cells and their possible axis systems [80].

Crystal system	Axis system
<b>Cubic</b>	$a=b=c, \alpha=\beta=\gamma=90^\circ$
<b>Tetragonal</b>	$a=b \neq c, \alpha=\beta=\gamma=90^\circ$
<b>Hexagonal</b>	$a=b \neq c, \alpha=\beta=90^\circ \gamma=120^\circ$
<b>Rhombohedral</b>	$a=b=c, \alpha=\beta=\gamma \neq 90^\circ$
<b>Orthorhombic</b>	$a \neq b \neq c, \alpha=\beta=\gamma=90^\circ$
<b>Monoclinic</b>	$a \neq b \neq c, \alpha=\gamma=90^\circ \beta \neq 90^\circ$
<b>Triclinic</b>	$a \neq b \neq c, \alpha \neq \beta \neq \gamma \neq 90^\circ$

When parallel planes of atoms are intersecting the unit cell, they define orientations and inter-planar distances through the Miller indices (hkl), which represent the reciprocals of the intersections of each of the three axes in the unit cell. For example, in figure (3-3), planes that cut the x-axis at  $a/2$ , b-axis at b and c-axis at  $c/3$ , are described by the Miller indices (213) [79][80].

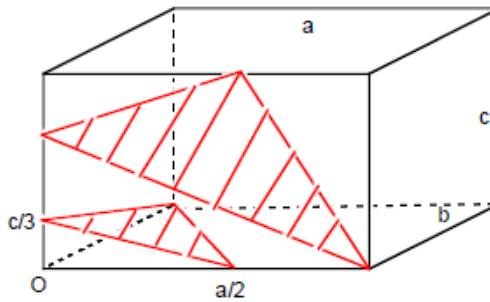


Fig 3-3. Parallel planes of atoms intersecting the unit cell [77].

- X-ray scattering:

The units in a crystal are arranged in long-range periodic arrays, and upon hitting a crystalline matter X-rays cause the electrons surrounding each atom in the periodic arrays to oscillate, scattering the radiation. This scattered radiation is in phase, and constructive interference is obtained, resulting in waves of high intensity [79][76][80][81]. These diffraction patterns give information about the units arrangement within a crystal, helping elucidate the crystal structure and presenting a fingerprint for each crystalline material [78][81].

- Bragg's law:

Constructive interference of diffracted rays occurs when meeting certain geometric conditions. This is expressed by Bragg's law. The relationship between the diffraction angles, X-ray wavelength and inter-planar space is represented as follows in equation (1) [78]:

$$n\lambda = 2d \sin\theta \quad \text{eq.1}$$

where, n is the order of reflection (n=1),  $\lambda$  is the wavelength of the X-ray, d is the distance between parallel planes, and  $\theta$  is the angle of incident ( which is equal to angle of reflection) [78].

The application of Bragg's law is schematically presented in Figure (3-4). The incident and reflected rays form an angle ( $\theta$ ) with the parallel planes separated by a spacing "d". for the reflected rays to be in phase, the length difference between their paths must be a multiple of their wavelength [76][78][79].

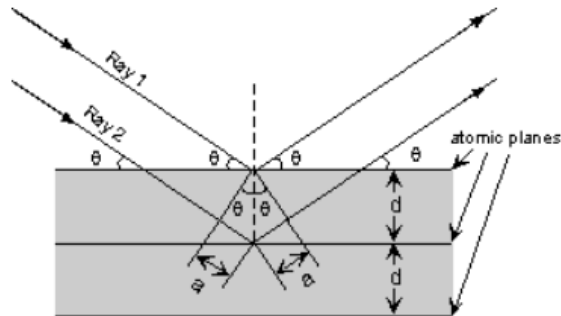


Fig 3-4. X-ray reflection from two parallel planes [81].

### **3.1.2. Instrumentation of XRD:**

In X-ray powder diffraction, the sample should be grounded well into a fine and smooth powder to have a homogenous and randomly oriented sample crystals, to obtain a random distribution of all the possible planes that contribute to the production of constructive reflections of the crystal structure. Large non-randomly oriented crystal sample will give rise to variation of peak intensities [78][79][80][81].

The typical geometry used for powder XRD is the Bragg-Brentano one, presented in Figure (3-5). The X-ray tube is stationary, the sample rotates at an angle theta ( $\theta$ ) from the X-ray tube, while the detector rotates at an angle 2-theta ( $2\theta$ ) from the X-ray tube, detecting the diffracted beams and recording the high intensity of constructive interference when it occurs as per Bragg's law (eq.1). When X-ray intensity is plotted against the angle  $2\theta$ , as shown in Figure (3-6), the high intensity signals are those where Bragg's law is met, and which correspond to X-rays constructively reflected from planes with different "d" values. The dimensions of the unit cell can also be determined [78][79][80].

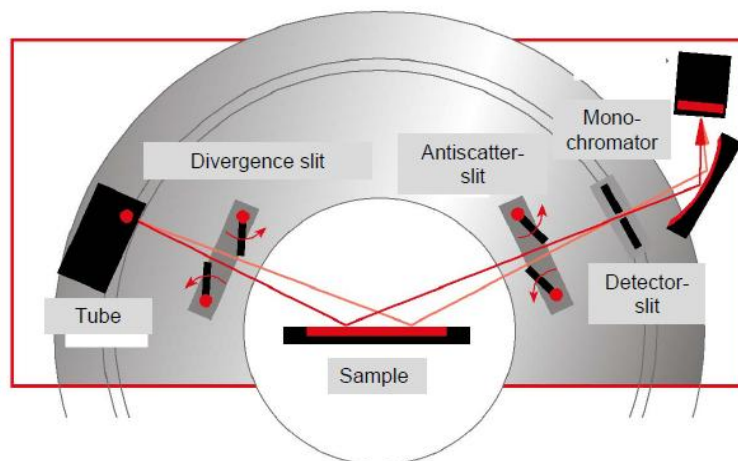


Fig 3-5. The Bragg-Brentano geometry [76].

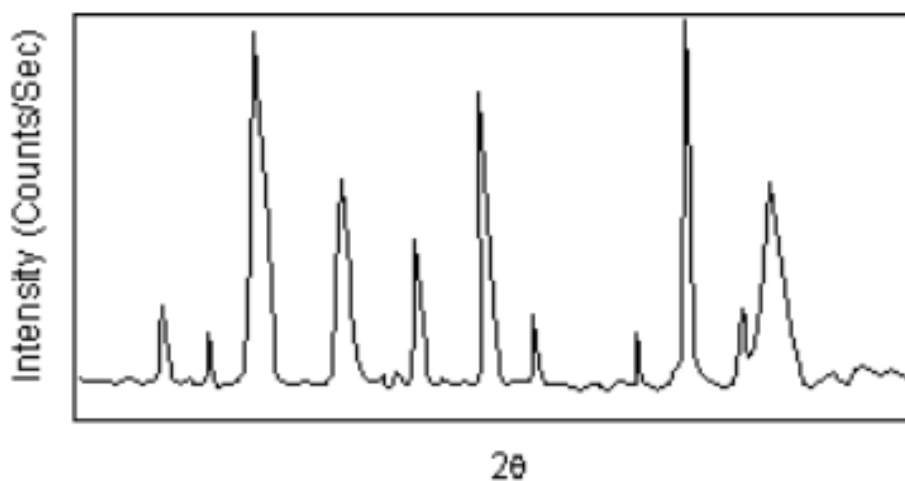


Fig 3-6. An example of XRD chart [79].

## 3.2. Ultraviolet/Visible (UV/Vis) spectroscopy

### 3.2.1. Principles of UV/Vis spectroscopy:

The absorption of electromagnetic radiation in the UV or Vis range causes an energy change ( $\Delta E$ ) in the valence electrons of a molecule or an atom, leading to electronic transitions when  $\Delta E$  of the transition corresponds to the energy of the incoming radiation. In this case, the incident radiation of this energy value will be absorbed by the sample, and the remaining radiation will be transmitted [82][83][86].

Absorbance is the measure of this absorbed radiation and is directly proportional to the amount of absorbing species (atoms, ions or molecules) in a sample. This relation is expressed by the Beer-Lambert as follows in equation (2):

$$A = \epsilon \times c \times d \quad \text{eq.2}$$

Where ( $\epsilon$ ) is the molar absorption coefficient, a material specific constant, ( $c$ ) is the concentration of the absorbing species in the sample and ( $d$ ) is the path length of the radiation through the sample [82][83][86]. This relation then allows the determination of unknown concentrations using calibration curves constructed using known concentrations. Beer-Lambert law (eq.2) however is only applicable in low concentration ranges, and at higher concentrations, the linearity between Absorbance and concentration no longer holds.

### **3.2.2. Instrumentation of UV/Vis spectroscopy:**

There are two types of UV/Vis spectrophotometers: single-beam and double-beam spectrophotometers. The simple single-beam set up as shown in figure (3-7) has a single optical path from the source to the detector, using a fixed-wavelength monochromator. It requires calibration every time before measuring the sample. The advantage of this set up is that it is relatively inexpensive and easily transported, but on the other hand the recalibration process is time-consuming and the spectrophotometer is less accurate than the double-beam spectrophotometer [83]. It is therefore useful for measurements at a particular value of wavelength.

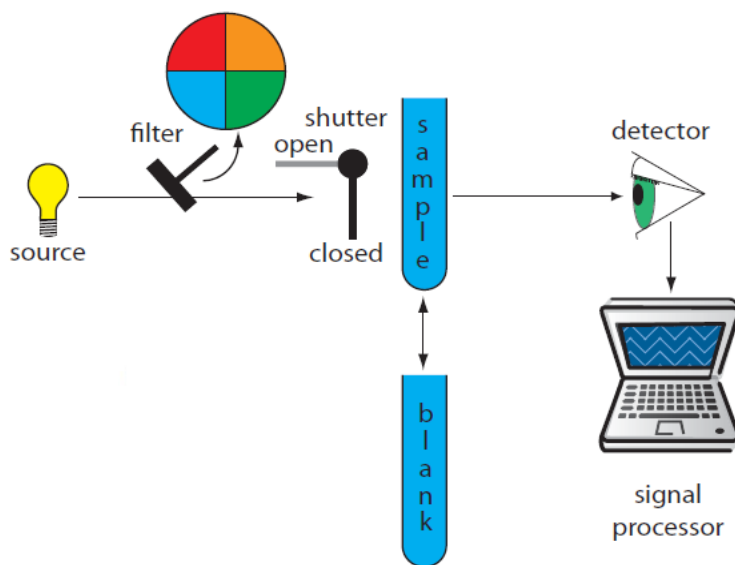


Fig 3-7. Schematic diagram of single-beam spectrophotometer setup [83].

As for the double-beam spectrophotometer in figure (3-8), the setup comprises the radiation source, followed by a monochromator to select the required wavelength falling onto the sample. The beam is split into two equal parts by a half mirror to simultaneously pass through a blank and the sample. The detector collects both beams, determining the sample Absorbance at this particular wavelength. When the Absorbance is plotted against wavelength values as in figure (3-9), the Absorbance spectrum of the sample is obtained where the wavelength of the highest Absorbance represents  $\lambda_{\max}$ , which is characteristic for each substance. The double-beam setup is more expensive but more versatile and accurate than the single-beam setup [82][83][86].

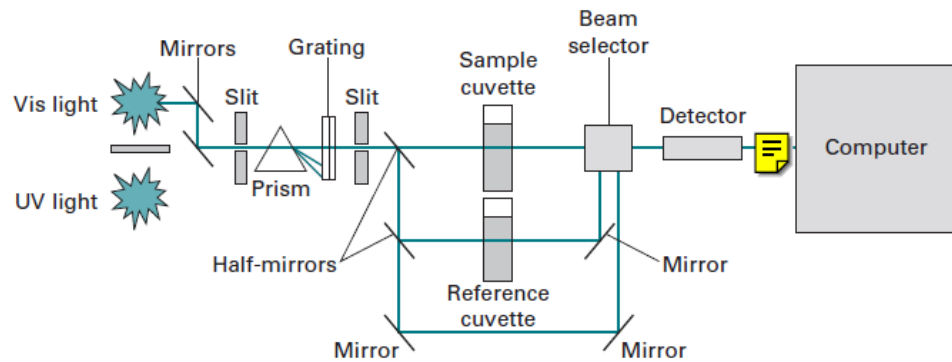


Fig 3-8. Schematic diagram of double-beam spectrophotometer setup [82].

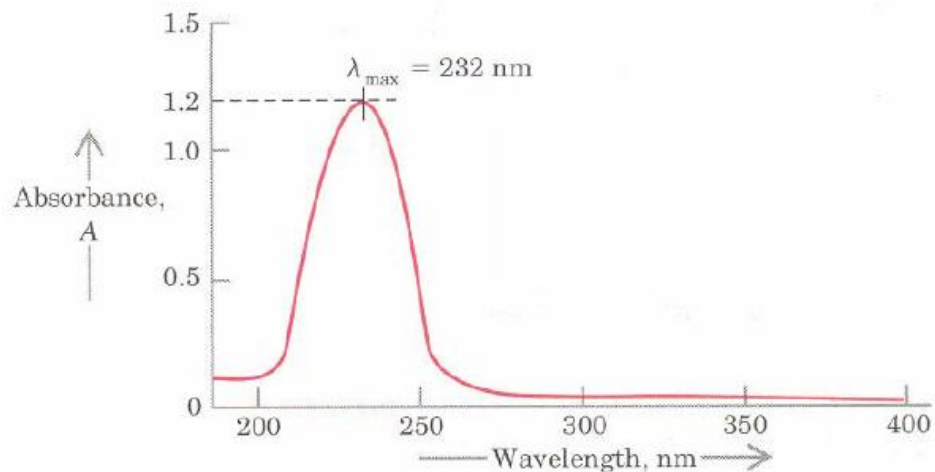


Fig 3-9. An example of a UV spectrum [86].

### 3.3. Fourier transform Infrared (FTIR) spectroscopy

#### **3.3.1. Principles of FTIR:**

FTIR spectroscopy gives important information about the sample's identity and the number of components in a sample mixture [87]. For a sample to absorb IR radiation, the radiation must induce molecular vibration associated with a change in the dipole moment of a molecule in the sample. When the energy of the molecular vibration is equal to that of the IR radiation, absorption takes place. A general model in figure (3-10) represents the molecular system as atoms connected to each other by a spring-like bonds that expand and contract as a response to the vibrational frequencies [90][91].

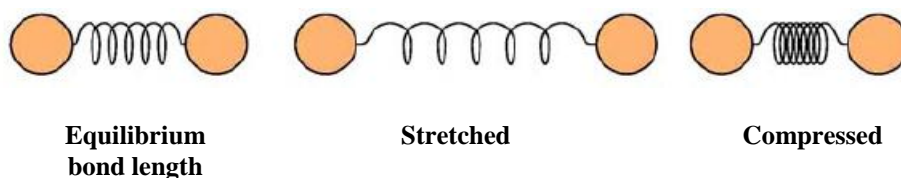


Fig 3-10. Changes in the dipole moments of a diatomic molecule [91].

The atoms are continuously moving relative to each other around their central atom in two common vibrational modes: stretching and bending. In the stretching mode, a change in the bond length takes place. Stretching can be classified into symmetric (in-phase stretching) and asymmetric (out-of-phase stretching) modes (figure 3-11.a). In bending modes, a change in the angles between the atoms occurs. Bending is classified into rocking, scissoring, wagging and twisting (figure 3-11.b). Since the change of the molecular dipole moment is a must for IR-radiation absorption to take place, the greater the change, the higher is the absorption intensity. The stretching mode represents the most detectable and useful peaks in the IR spectrum, because stretching the bonds between two atoms of different electronegativities greatly changes the dipole moment [90][91][92].



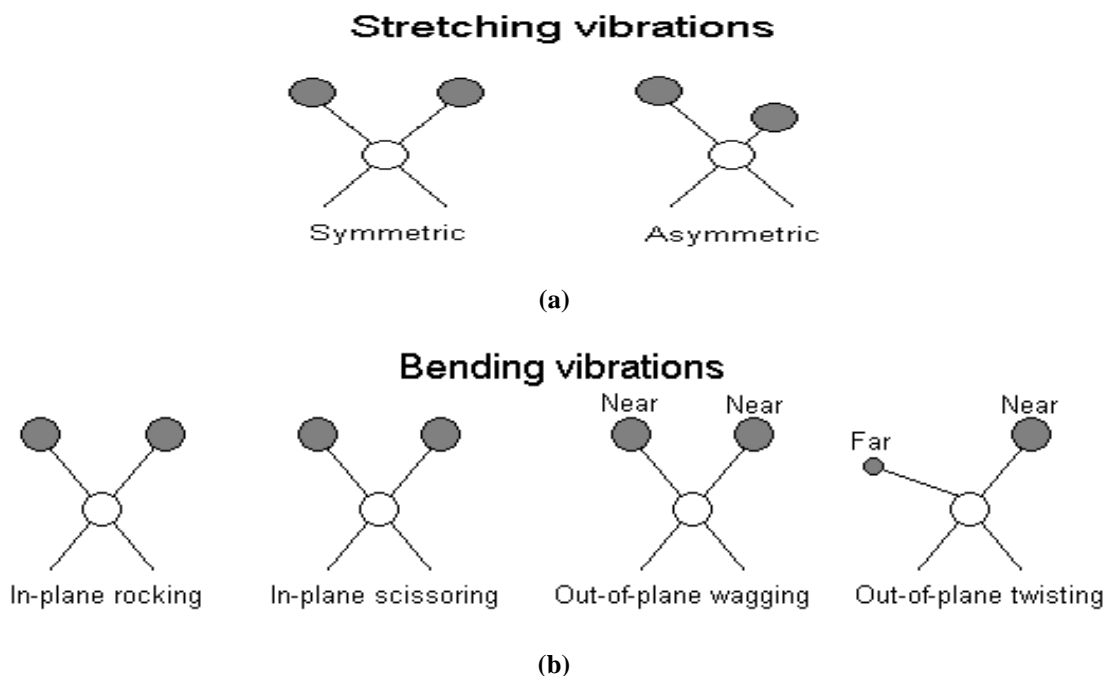


Fig 3-11. Stretching (a), and bending vibration (b) modes [93].

The frequency of the vibrational modes can be calculated mathematically when the stretching vibration is approximated by Hooke's law, that is derived from the simple harmonic oscillator model. The frequency ( $\nu$ ) of the vibration is related to the force constant ( $k$ ) of the spring and the reduced masses of the atoms ( $\mu$ ) as follows in equation (3) [88][89][90]:

$$\nu = \frac{1}{2\pi} \sqrt{\frac{k}{\mu}} \quad \text{eq.3}$$

The value of the reduced masses is calculated as follows from equation (4) where  $m_1$  and  $m_2$  are the masses of involved atoms [88][89][90]:

$$\mu = m_1 m_2 / (m_1 + m_2) \quad \text{eq.4}$$

And to have a direct use of the wavenumber values of the vibrational frequencies, the first equation is modified as follows in equation (5):

$$\bar{\nu} = \frac{1}{2\pi c} \sqrt{\frac{k}{\mu}} \quad \text{eq.5}$$

where  $\bar{\nu}$  is the wavenumber and  $c$  is the speed of light [88][89][90].

When applied to a molecule in a sample this model leads to different vibrational modes of the different functional groups constituting the molecule. This leads to the absorption of the radiation of energies equal to the energies of each of these vibrational modes, leading

to a spectrum for the sample, with absorption bands characteristics of the different functional groups present and their structural arrangement. In this respect a IR spectrum of a species helps elucidate structural details [90][91].

### 3.3.2. Instrumentation of FTIR:

FTIR spectrophotometry (figure 3-12) relies on an “interferometer”, which by turn is equipped with a beam splitter that splits the incident infrared beam into two: one reflects off of a fixed flat mirror at a fixed path length and the other from a mirror that moves at short distances to create a path difference between the two beams. These two reflected beams are then combined and interfered via the interferometer to include every single data about the incoming infrared frequency in a simultaneous fast manner. The produced signal is interpreted, through the application of a Fourier Transform resulting in a spectral plot of intensity versus wavenumber/frequency, reflecting the absorbing species structural information [87][95].

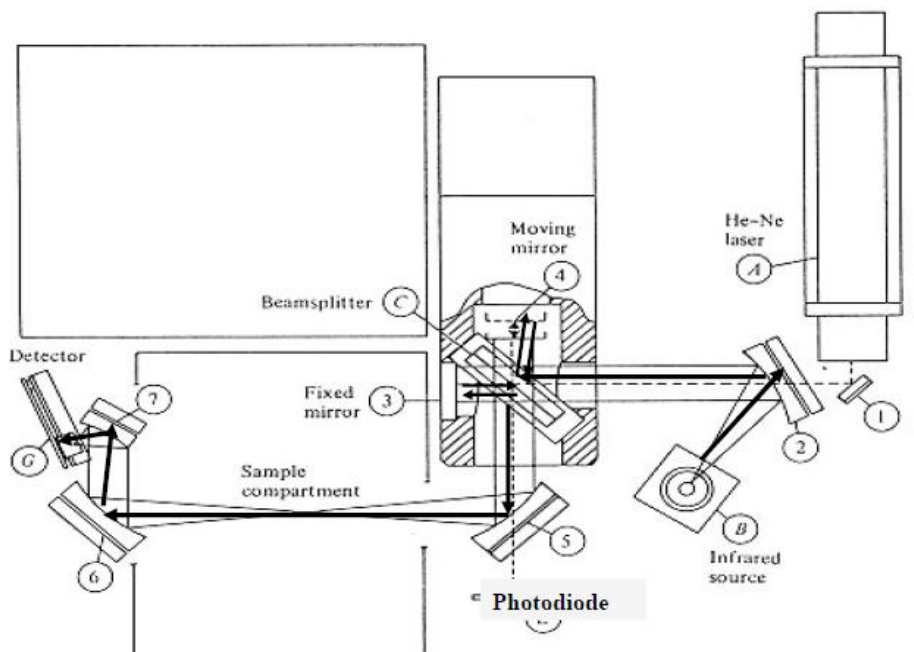


Fig 3-12. Principle of FTIR spectrometer operation [95].

The analyzed samples could be a liquid, solid or gas. Sample holders (for liquids and gases) must be IR transparent and are typically composed of an alkaline metal halide. Solid samples are typically prepared by the KBr pellet technique where a mixture of 2-3 mg of the sample with 0.5-1 g of KBr is pressed into a transparent disk [96].

### 3.4. Scanning Electron Microscopy (SEM)

The SEM was invented 50 years ago, and now is a widely used scientific technique in metallurgy, geology, biology, medicine and many other fields, since it is capable of providing a nano-scale resolution with a good depth of field, giving information about the morphology, structures and chemical compositions and many other features [97][98].

#### **3.4.1. Principles of SEM:**

The SEM generates an accelerated beam of electrons from a suitable cathode source that passes through a set of condenser and objective lenses to decrease its cross section. The spot-like electron beam scans the surface of the sample in a vacuumed atmosphere, and an image is formed by collecting various signals reflected from the different interactions between the electron beam and the sample [97][98][99].

There are two types of interactions that are responsible for an image formation: elastic and inelastic interactions. In the elastic interactions, electrons are generated from the back scattering of the incident electron beam by the outer electrons of a sample specimen having the same energy, at an angle greater than  $90^\circ$ , and giving an image of the sample's depth. In inelastic interaction, the incident electron beam interacts with the specimen's outer electrons, leading to the generation of secondary electrons from a depth of 5 nm below the surface, giving an image of the sample surface. In addition, other signals generated from the interaction between the electron beam and the sample such as X-ray emission, Auger electrons and cathodoluminescence can be used for additional compositional information about the sample, as shown in figure (3-13) [99][100][101].

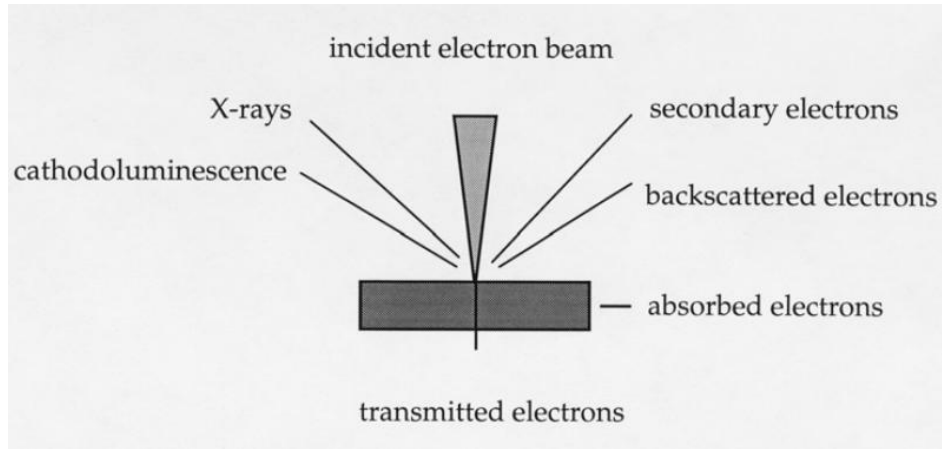


Fig 3-13. Illustration of the different signals obtained from hitting the sample specimen with the incident electron beam [99].

### **3.4.2. Instrumentation of SEM:**

The SEM (figure 3-14) is equipped with an electron gun that produces an electron beam at a high voltage, with a small spot size and low energy dispersion. The electron beam then passes through the anode aperture into a lens system that focuses it onto the sample. The sample is placed in a chamber at high vacuum so as to prevent specimen contamination and interference of gas phase scattering. To obtain a clear image, the samples must be electrically conductive; because they exhibit high electron density, increasing the emission of secondary electrons, that are responsible for producing a strong image, and otherwise, it is sputter-coated with a conductive metal such as gold, silver or palladium [97][100][101].

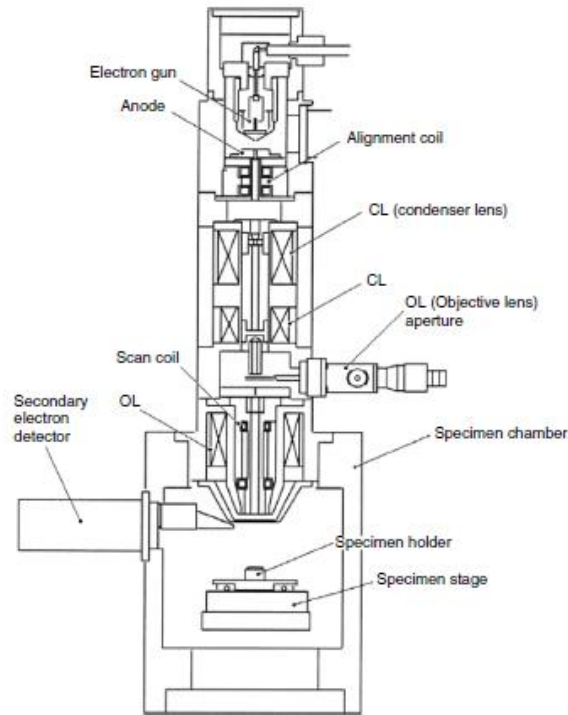


Fig 3-14. Diagram of the scanning electron microscope (SEM) [100].

## 3.5. Zetasizer analyzer

### 3.5.1. Principle of Zetasizer:

The Zetasizer analyzer is capable of measuring both the size and zeta potential of a particle.

The zetasizer measures the zeta potential, by applying an electric field to the liquid in which the particles are suspended (electrophoresis). These particles would move towards the electrode of opposite charges (attractive force), and the viscosity of the liquid surrounding the particles will act as an opposing force, resulting in an equilibrium state, that ends up in the particles moving at a constant velocity. This velocity is known as electrophoretic mobility, which is measured directly by an equipped laser technique called Laser Doppler Velocimetry (LDV) [102][103]. The electrophoretic mobility is translated to zeta potential by applying Henry's law (equation 6) as follows:

$$U_E = \frac{2\varepsilon z f(ka)}{3\eta} \quad \text{eq.6}$$

Where,  $z$  is the zeta potential,  $U_E$  is the electrophoretic mobility,  $\epsilon$  is dielectric constant,  $\eta$  viscosity, and  $f(ka)$  is Henry's function ( $\approx 1$ ) [102][103].

As for particles' size function, which is the main concern in this research is to be elaborated in details. The zetasizer measures the particle sizes via dynamic light scattering (DLS) technique, which measures the particles' Brownian motion (collision of particles with the surrounding liquid) and relates it to their sizes. It begins by directing a laser onto the particles, which by turn scatters the light. The scattered light is then collected at a screen held close to the particles, to give a speckle pattern of bright and dark areas as in figure 3-15. To determine the particle sizes, the DLS compares first the intensity signals of a particular part of the speckle at a time point ( $t$ ), to another signal at a later time ( $t + \delta t$ ), but over a very small time scale in the order of 1 to 10's milliseconds, in order to have a good correlation between the signal intensities over time. However, the suspended particles are not stationary due to Brownian motion, which leads to fluctuation of the intensities of the bright and dark areas in the speckle pattern. Therefore, the size particle is related to the rate of correlation decay: where small particles have fast correlation decay than large ones as seen in figure 3-16, because of their motion speed differences [102][103].

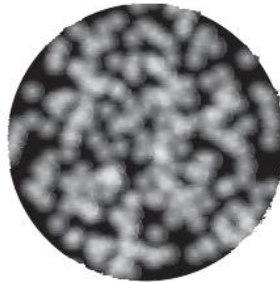


Fig 3-15. A screen with a speckle pattern of bright and dark areas [102].

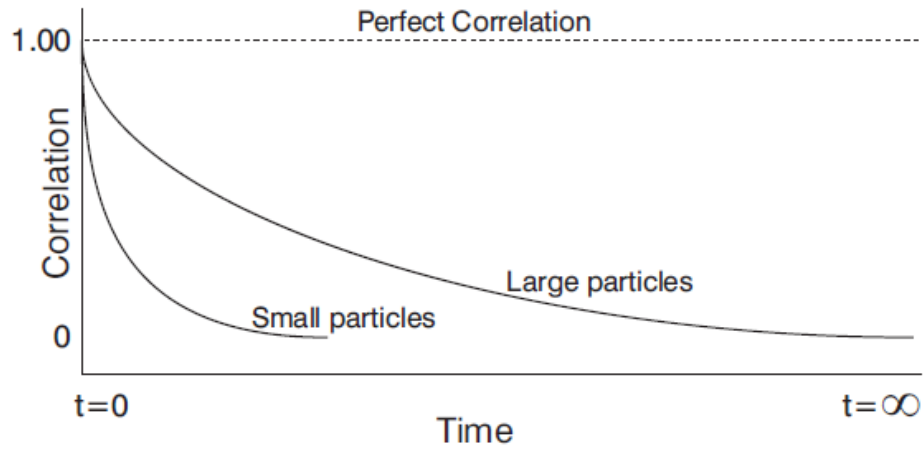


Fig 3-16. Correlation function of small and large particles over time [102].

The Zetasizer software uses algorithm to use the collected information of the correlation function to calculate the size distribution and displays it in the form of a graph as shown in figure 3-17, where X-axis represents the size distribution and Y-axis represents the relative intensity of scattered light [102][103].

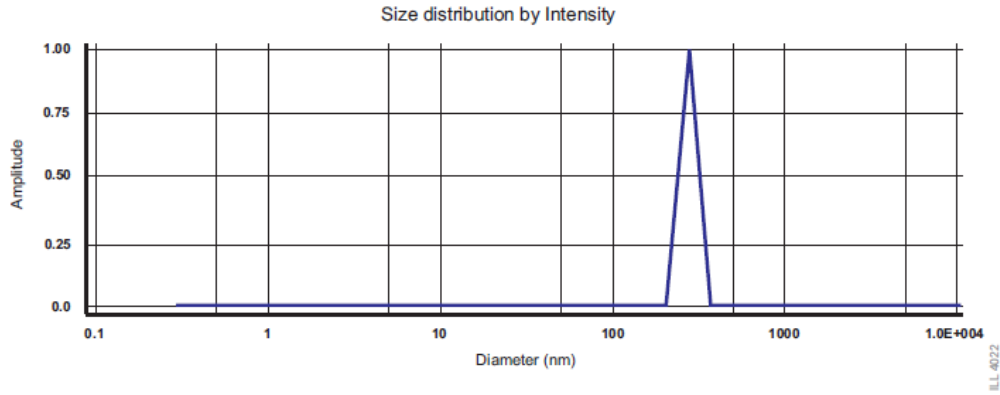


Fig 3-17. A typical size distribution graph [102].

### 3.5.2. Instrumentation of Zetasizer:

The DLS system consists of six main parts (figure 3-18): the laser source, which illuminate the particles that are suspended inside a cell. The intensity of the scattered light is then measured by the detector. However, the intensity of light should be within a certain range for the detector to measure, therefore, the system is equipped with an attenuator to adjust the intensity of the scattered light. The scattered light is then passes to a digital signal processor know as a correlator; which detects the correlation between the signal intensities at successive time intervals. The correlation information is then transferred to the computer to produce a size distribution related data [102][103].

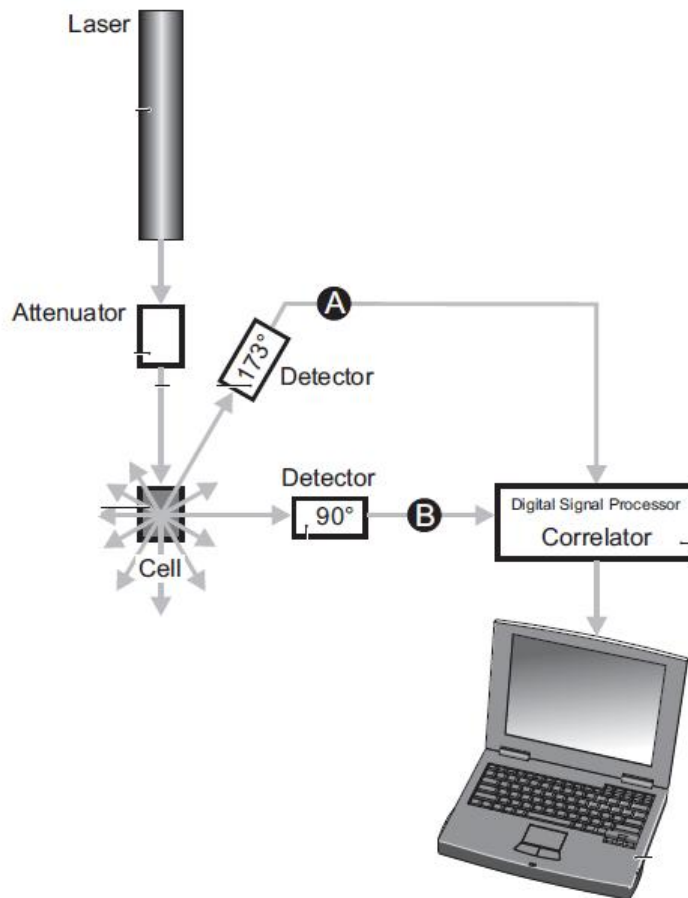


Fig 3-18. A schematic description of the Zetasizer analyzer [102].



# **Chapter 4.**

## **Materials and Methods**

## 4. Materials and Methods

---

### 4.1. Materials

High purity materials were purchased. Zinc nitrate hexahydrate (98%), Aluminum nitrate nonahydrate ( $\geq 98\%$ ), Sodium hydroxide ( $\geq 98\%$ ), sulfuric acid (95-97%), hydrochloric acid (37%), potassium permanganate ( $> 99\%$ ), copper sulphate pentahydrate ( $> 98\%$ ), acetic acid (99.8%) and Phosphoric acid (85 %) were purchased from Sigma-Aldrich (Germany). Graphene nanopowder (11-15 nm) was purchased from SkySpring Nanomaterial (USA). Hydrogen peroxide (30%) was purchased from Merck (Germany), sodium acetate trihydrate (99.7%) was purchased from Fischer scientific, and ethanol (99.9%) was purchased from Carlo Erba (Italy). Alendronate sodium in trihydrate form (97%) was purchased from Alfa Aesar (Germany).

### 4.2. Preparation of pristine LDHs

Two different cationic ratios of Zn-Al LDH: ( $\text{Zn}^{2+} : \text{Al}^3+$ ) of 2:1 and 3:1, in their nitrate forms were prepared, by co-precipitation, following the procedure described elsewhere [104]:

The two Zn-Al- $\text{NO}_3$  LDH systems were prepared by mixing 0.1 M  $\text{Zn}(\text{NO}_3)_2 \cdot 6 \text{H}_2\text{O}$  with 0.1 M  $\text{Al}(\text{NO}_3)_3 \cdot 9 \text{H}_2\text{O}$ , with ratios of 2:1 (30 ml:15 ml) or 3:1 (30 ml:10 ml). The mixture was then co-precipitated at room temperature and while maintaining the pH at 7, by the drop-wise addition of 2 M NaOH [1][6]. The mixture was magnetically stirred throughout the reaction, with nitrogen gas bubbling into the mixture solution to expel any dissolved carbon dioxide and thus preventing the intercalation of carbonate ions. The produced precipitate was then filtered using Whatman® filter paper, grade 1, with 11  $\mu\text{m}$  pore size, followed by washing several times with de-ionized water to remove any impurities. The precipitate was then dried at 80°C overnight. This resulted in samples Zn<sub>2</sub>-Cp and Zn<sub>3</sub>-Cp for the 2:1 and 3:1  $\text{Zn}^{2+} : \text{Al}^{3+}$  LDH compositions respectively.

### 4.3. Oxidation of G powder

The oxidation of G followed the modified Hummer's method with slight modifications [18]. A 9:1 mixture of concentrated  $\text{H}_2\text{SO}_4/\text{H}_3\text{PO}_4$  (360 ml:40 ml) was added to a mixture of G (3 g.) and  $\text{KMnO}_4$  (18 g.). The mixture was heated to  $50^\circ\text{C}$ , and then magnetically stirred for 12 hours. The mixture was then cooled to room temperature, poured to 400 ml of crushed ice (to have a mixture of the ice, G and acids), and then 3 ml of 30%  $\text{H}_2\text{O}_2$  was added to it. It was then passed through a metal sieve (pore size:  $300\ \mu\text{m}$ ) to remove any impurities or aggregates, centrifuged (Fischer Scientific Centrifuge Model 228) for one hour at 1129 rpm ( $\text{RCF} (10)=1.12 \times \text{Radius}(7\text{mm}) \times (\text{rpm}/1000)^2$ ), and the supernatant was decanted. A purification process was then carried out on the solid product by successive washing with 200 ml deionized water, 200 ml 37% HCL, and twice with 200 ml ethanol. After each wash, the mixture was centrifuged and the supernatant was decanted. The resultant solid material was dried in a vacuum oven overnight [18].

### 4.4. Preparation of G and GO/LDH hybrids

Hybrids of G and GO/Zn-Al- $\text{NO}_3$ , were prepared by co-precipitating the LDH in the presence of a dispersion of the G or GO. The choice of weight percentage (% w/w) of G or GO in total hybrid weight, and the concentration of the intercalating solution were based on their effect on the crystallinity of the LDH hybrid.

#### **4.4.1. Determining the optimum GO weight percentage in the hybrid (%w/w):**

In this step, different % wt of GO were intercalated into the co-precipitated Zn-Al- $\text{NO}_3$  LDH with cationic ratio ( $\text{Zn}^{2+}/\text{Al}^{3+}$ ) of 2:1.

#### **Procedure**

**Solutions A:** 10 mg, 30 mg, or 70 mg of GO were first sonicated in small volumes of deionized water, till complete dispersion was achieved and a light brown suspension was obtained. The volumes were then completed to 250 ml with deionized water.

**Solution B:** A mixture of the metal cations was prepared with 0.1 M Zn (NO<sub>3</sub>)<sub>2</sub>.6 H<sub>2</sub>O and ml 0.1 M Al (NO<sub>3</sub>)<sub>3</sub>.9 H<sub>2</sub>O with a ratio of 2:1 (30 ml:15 ml).

Solution B was then added drop wise to each of solutions A together with dropwise addition of 2 M NaOH at room temperature and while maintaining a pH 7 [1][6]. The mixtures were magnetically stirred throughout the reaction, with nitrogen gas bubbling into the mixture solution to expel any dissolved carbon dioxide and avoid the intercalation of carbonate ions. The produced precipitates were then filtered using Whatman® filter paper, grade 1, with 11 µm pore size, washed several times with de-ionized water to remove any impurities and dried overnight in the oven at 80°C. This resulted in LDH-GO hybrids with 2 % wt (for 10 mg GO dispersed in solution A), 6.2 % wt, (for 30 mg GO dispersed in solution A), and 13.4 % wt (for 70 mg GO dispersed in solution A) of GO.

The 2 % wt GO showed the best XRD results, regarding the crystallinity of the LDH as would be discussed in the following chapter, and was thus chosen for the preparation of all LDH-GO and LDH-G hybrid samples.

#### **4.4.2. Determining the optimum volume for the G and GO dispersion solutions for the preparation of the LDH-G and LDH-GO hybrids:**

The LDH hybrid composition as selected to be 2% (w/w) in G or GO, as explained above. Different volumes for the G and GO dispersion solutions were investigated for the formation of the LDH-G and LDH-GO hybrid to identify the optimum volumes. Both metal cationic ratios (Zn<sup>2+</sup>:Al<sup>3+</sup>) of 2:1 and 3:1 for the LDH were used. Table 4-1, summarizes the amounts and volume for different samples used in this investigation.

Table 4-1. G and GO/Zn-Al-NO<sub>3</sub> hybrids prepared with different concentrations of the G and GO suspension/solution.

Molar ratio (M <sup>2+</sup> : M <sup>3+</sup> ) for the LDH	Amount of dispersed G (mg/ml)				Amount of dispersed GO (mg/ml)			
	0.04	0.1	0.2	0.4	0.04	0.1	0.2	0.4
2:1	Zn <sup>2+</sup> - G.04-Cp	Zn <sup>2+</sup> - G.1-Cp	Zn <sup>2+</sup> - G.2-Cp	Zn <sup>2+</sup> - G.4-Cp	Zn <sup>2+</sup> - GO.04-Cp	Zn <sup>2+</sup> - GO.1-Cp	Zn <sup>2+</sup> - GO.2-Cp	Zn <sup>2+</sup> - GO.4-Cp
3:1	Zn <sup>3+</sup> - G.04-Cp	Zn <sup>3+</sup> - G.1-Cp	Zn <sup>3+</sup> - G.2-Cp	Zn <sup>3+</sup> - G.4-Cp	Zn <sup>3+</sup> - GO.04-Cp	Zn <sup>3+</sup> - GO.1-Cp	Zn <sup>3+</sup> - GO.2-Cp	Zn <sup>3+</sup> - GO.4-Cp

Procedure:

**Solutions A:** different amounts of G or GO were used for the suspension in different volumes: 0.04, 0.1, 0.2, 0.4 mg/ml in 250, 100, 50 and 25 ml volumes respectively. The G or GO was first sonicated in small volume of deionized water to obtain a homogenous suspension, free of agglomerates in case of G, and a clear light brown suspension in case of GO, and then the volumes were completed with deionized water.

**Solution B:** a mixture of the metal cations was prepared with 0.1 M Zn (NO<sub>3</sub>)<sub>2</sub>.6 H<sub>2</sub>O and ml 0.1 M Al (NO<sub>3</sub>)<sub>3</sub>.9 H<sub>2</sub>O with a ratio of 2:1 (30 ml:15 ml) or a ratio of 3:1 (30 ml:10 ml).

Solution B was added dropwise to each of solutions A together with dropwise addition of 2 M NaOH at room temperature and while maintaining a pH 7 [1][6]. The mixtures were magnetically stirred throughout the reaction, with nitrogen gas bubbling into the mixture solution to expel any dissolved carbon dioxide and avoid the intercalation of carbonate ions. The produced precipitates were then filtered using Whatman® filter paper, grade 1, with 11 µm pore size, washed several times with de-ionized water to remove any impurities and dried overnight in the oven at 80°C. This resulted in LDH-G and LDH-GO hybrids with 2 % wt of G or GO, as per Table (4-1).

As the different volumes of G or GO dispersion solutions did not show any impact on the hybrid samples produced, regarding differences in crystallinity (as would be discussed in

the following chapter), the largest solution volume (corresponding to the lowest dispersion concentration) would be therefore used. This larger volume would ensure easier dissolution of the drug to be loaded in these hybrids.

## 4.5. Loading of alendronate sodium

Alendronate sodium was loaded into the different host systems: pristine Zn-Al-NO<sub>3</sub> LDHs and the LDH-G and LDH-GO hybrids, and the different loading efficiencies of each of the systems investigated. Drug loading was conducted by co-precipitation and ion-exchange, as described elsewhere [104].

### 4.5.1. Co-precipitation:

Table 4-2 The intercalated systems with alendronate sodium prepared by co-precipitation.

Drug's name	Drug's molar concentration	Molar ratio (M2+: M3+)	Intercalated system	Sample code
Alendronate sodium	0.002 M	2:1	Zn-Al-NO <sub>3</sub>	A-Zn2-Cp
			Zn-Al-NO <sub>3</sub> /G	A-Zn2-G-Cp
			Zn-Al-NO <sub>3</sub> /GO	A-Zn2-GO-Cp
		3:1	Zn-Al-NO <sub>3</sub>	A-Zn3-Cp
			Zn-Al-NO <sub>3</sub> /G	A-Zn3-G-Cp
			Zn-Al-NO <sub>3</sub> /GO	A-Zn3-GO-Cp

#### Procedure:

##### **A- Preparation A-Zn2-Cp and A-Zn3-Cp hybrids:**

**Solution A:** known amount of alendronate sodium (0.0005 moles) was dissolved in a total volume of 250 ml of deionized water to have a drug concentration of approximately 0.002 M.

**Solution B:** a mixture of metal cations was prepared with 0.1 M Zn (NO<sub>3</sub>)<sub>2</sub>.6 H<sub>2</sub>O and 0.1 M Al (NO<sub>3</sub>)<sub>3</sub>.9 H<sub>2</sub>O with a ratio of 2:1 (30:15 ml) for A-Zn2-Cp, or a ratio of 3:1 (30:10 ml) for A-Zn3-Cp.

Solution B was added dropwise to solution A together of dropwise addition of 2 M NaOH at room temperature and while maintaining a pH 7 [1][6]. The mixtures were magnetically stirred throughout the reaction, with nitrogen gas bubbling into the mixture solution to expel any dissolved carbon dioxide and avoid the intercalation of carbonate ions. The produced precipitates were then filtered using Whatman® filter paper, grade 1, with 11 µm pore size, washed several times with de-ionized water to remove any impurities and dried overnight in the oven at 80°C. This resulted in samples A-Zn2-Cp and A-Zn3-Cp as presented in Table (4-2).

**B- Preparation of A-Zn2-G-Cp, A-Zn3-G-Cp, A-Zn2-GO-Cp, and A-Zn3-GO-Cp:**

**Solution A:** a known amount of alendronate sodium (0.0005 moles) was dissolved in a total volume of 250 ml of deionized water to have a drug concentration of approximately 0.002 M. An amount of G or GO was dispersed in the drug solution to result in a 2% wt of G in the LDH-G hybrid or of GO in the LDH-GO hybrid. The mixtures were sonicated till a homogenous, agglomerate-free suspension was produced in the case of G, and a clear light brown solution was obtained in the case of GO. The mixture was then left to stir for 24 hours.

**Solution B:** a mixture of metal cations was prepared with 0.1 M Zn (NO<sub>3</sub>)<sub>2</sub>.6 H<sub>2</sub>O and 0.1 M Al (NO<sub>3</sub>)<sub>3</sub>.9 H<sub>2</sub>O with a ratio of 2:1(30 ml:15 ml) for A-Zn2-G-Cp and A-Zn2-GO-Cp or a ratio of 3:1 (30 ml:10 ml) for A-Zn3-G-Cp and A-Zn3-GO-Cp.

Solution B was added dropwise to solutions A together of dropwise addition of 2 M NaOH at room temperature and while maintaining a pH 7 [1][6]. The mixtures were magnetically stirred throughout the reaction, with nitrogen gas bubbling into the mixture solution to expel any dissolved carbon dioxide and avoid the intercalation of carbonate ions. The produced precipitates (containing the drug) were then filtered using Whatman® filter paper, grade 1, with 11 µm pore size, washed several times with de-ionized water to remove any impurities and dried overnight in the oven at 80°C. This resulted in samples A-Zn2-G-Cp, A-Zn2-GO-Cp, A-Zn3-G-Cp and A-Zn3-GO-Cp as presented in Table (4-2).

#### 4.5.2. Ion- exchange:

Table 4-3. The intercalated systems with alendronate sodium prepared by ion-exchange.

Drug's name	Drug's molar concentration	Molar ratio (M <sub>2</sub> <sup>+</sup> : M <sub>3</sub> <sup>+</sup> )	Intercalated system	Sample code
Alendronate sodium	0.01 M	2:1	Zn-Al-NO <sub>3</sub>	A-Zn2-IE
			Zn-Al-NO <sub>3</sub> /G	A-Zn2-G-IE
			Zn-Al-NO <sub>3</sub> /GO	A-Zn2-GO-IE
		3:1	Zn-Al-NO <sub>3</sub>	A-Zn3-IE
			Zn-Al-NO <sub>3</sub> /G	A-Zn3-G-IE
			Zn-Al-NO <sub>3</sub> /GO	A-Zn3-GO-IE

#### Procedure:

A known amount of alendronate sodium (0.0005 moles) were dissolved in a total volume of 50 ml of deionized water to have a drug concentration of approximately 0.01 M. It is important to note that a smaller total volume with a higher concentration of the drug was used for the ion-exchange (as compared with that used for co-precipitation) in order to allow for an efficient ion-exchange process.

Portions of 100 mg of previously prepared Zn<sub>2</sub>-Cp, Zn<sub>3</sub>-Cp, Zn<sub>2</sub>-G.04-Cp, Zn<sub>2</sub>-GO.04-Cp, Zn<sub>3</sub>-G.04-Cp and Zn<sub>3</sub>-GO.04-Cp were dispersed in the drug solution and sonicated till complete dispersion (when a white suspension is formed and no solid residues), the pH was then adjusted to 7 by the dropwise addition of 2 M NaOH [1][6]. The mixtures were magnetically stirred under nitrogen bubbling into the mixture for 24 hours to allow ion-exchange to take place. The produced suspensions were then vacuum filtered through a Whatman® nylon filter membrane of pore size 0.45 µm, in order to prevent the loss of the low yield precipitates, which were then dried overnight in the oven at 80 °C. This resulted in samples A-Zn<sub>2</sub>-IE, A-Zn<sub>2</sub>-G-IE, A-Zn<sub>2</sub>-GO-IE, A-Zn<sub>3</sub>-IE, A-Zn<sub>3</sub>-G-IE, and A-Zn<sub>3</sub>-GO-IE, as presented in Table (4-3).



## 4.6. Characterization

The pristine LDHs, LDH-G, LDH-GO systems, and the drug-loaded systems were characterized by XRD, FTIR, SEM, and Zetasizer analyzer, while the loaded and released drug from the systems were quantified by UV/Vis spectrophotometry.

### **4.6.1. Powder X-ray Diffraction (PXRD):**

The powder X-ray diffraction patterns of the samples were obtained using a D8 Bruker X-ray diffractometer, which was operated at 40 KV and 30 mA, and using Cu as the anode target, producing  $K\alpha$ -X-rays of high intensity with a wavelength of 0.1542 nm. The patterns were detected at 2-theta range between 3° to 80° with a step size of 0.030°, and a step time 3 seconds.

### **4.6.2. Fourier Transform Infrared Spectroscopy (FTIR):**

The FTIR spectra of the samples were obtained using a Thermo-scientific Nicolet 380 Fourier Transform Infrared spectrophotometer, using the KBr pellet method. The KBr pellets were prepared by grinding and mixing a ratio of 1:100 (sample mass: KBr mass), which was then compressed by a hydraulic pressure at a pressure of 1400 KPa. The FTIR spectra obtained presented a plot of wave number (4000-500  $\text{cm}^{-1}$ ) against % transmittance.

### **4.6.3. Scanning Electron Microscope (SEM):**

The morphological images of the samples were obtained by using Leo Zeiss supra field emission scanning electron microscope (FESEM). The instrument was operated at 23 KV. The samples were conductive due to the presence of Zn and Al metals in the LDH and graphene, and therefore, there was no need for a coating layer.

### **4.6.4. Ultraviolet/Visible (UV/Vis) spectroscopy:**

The amount of drug loaded or released was quantified using a Varian Cary 500 UV-Vis NIR double-beam spectrophotometer. The absorbance of the drug loaded was detected at  $\lambda_{\text{max}}$  of 228 nm, while that of released drug was detected at 233 nm. The drug solution concentration values were determined from pre-constructed calibration curves (please refer to Appendix A).

Alendronate sodium lacks a detectable chromophore, which makes it difficult to be directly detected. However, since, alendronate sodium exhibits a metal-complexing property, derivatization of alendronate sodium by introducing a UV- active metal is typically used to allow its spectroscopic detection. Alendronate sodium forms a stable complex with copper (II) ( $\text{Cu}^{2+}$ ) ions, in acidic medium, having a 1:1 stoichiometry, that is detectable by UV/Vis spectrophotometry, which is presented as follows in equation (7):



Where ABP stands for alendronate sodium bisphosphonates [107][108]. As long as the concentration of the alendronate sodium in the sample is higher than that of  $\text{Cu}^{2+}$ , the increase in the absorbance is proportional to the increase in concentration of ABP-Cu complex, but at higher concentration of  $\text{Cu}^{2+}$ , alendronate sodium is saturated with  $\text{Cu}^{2+}$ , and the increase in absorbance is only proportional to the increase in the concentration of  $\text{Cu}^{2+}$  [108]. However, at constant concentration of  $\text{Cu}^{2+}$ , the saturation effect is negligible over a limited concentration range of alendronate sodium, and a linear relation between the absorbance and the concentration of alendronate sodium is obtained. Therefore, for the determinations here, the drug was derivatized as described by Walash et al. [107]. 2 ml of a 2 mM copper (II) sulfate solution together with 2 ml of 5 mM acetate buffer (pH 5, adjusted with acetic acid) were added to 2 ml of the alendronate sodium solution. The volume was completed to 25 ml using deionized water. In case of concentration determination in SGF (simulated gastric fluid), 2 ml of SGF were added to the solution mixture before completing to 25 ml. The concentration of alendronate sodium solutions to be detected were always kept in the range of 2-40  $\mu\text{M}$  [107][108].

#### **4.6.5. Zetasizer analyzer**

The particles size of the prepared samples were determined by Zetasizer analyzer (Image 3-1) (Nano-ZS90) from Malvern Instruments. Very small amount of the sample powder were dispersed in about 1ml deionized water and then analyzed by dynamic light scattering, with 90° scattering optics at room temperature.

## 4.7. Determination of alendronate sodium loading

The loaded amount of drug, which includes both intercalated and adsorbed species, was determined based on the fact that LDH is degradable in acidic media (stomach), and therefore, the loaded drug could be recovered and detected after dissolving the LDH in acid [105]. A known mass (50 or 100) mg of the drug-loaded systems were dissolved in a 10 ml of stimulated gastric fluid (SGF). The SGF stock was prepared according to the United States pharmacopeia (USP) 29: 2 g sodium chloride and 7 ml HCl were mixed together and the volume completed to 1000 ml by deionized water. The final pH was 1.2. The free drug was then detected by UV/Vis spectrophotometer at  $\lambda_{\text{max}}$  228 nm, and the concentration was determined using a pre-constructed calibration curve in SGF (please refer to Appendix A), following the procedure described in section 4.6.4.

## 4.8. In- vitro drug release

The in-vitro release study of alendronate sodium was performed in water medium as described in USP 29 for alendronate sodium solid dosage form. The dissolution procedure, needed to apply sink conditions. These are defined in the USP 29 as the volume of medium at least three times that required to form a saturated solution of the drug. Taking in consideration that the solubility of alendronate sodium in water is 10 mg/ml [106], a known mass of the loaded system (50 to 100 mg with predetermined drug loaded amounts) was suspended in 10 ml deionized water, and placed in a thermostated water bath shaker at 37 °C and 50 strokes/min. The absorbance of the released drug was detected at different time intervals (0.16, 0.5, 1, 2, 4, 6, 18, and 24 hrs) with UV/Vis spectrophotometer at  $\lambda_{\text{max}}$  233 nm, and the concentration was determined using a pre-constructed calibration curve in deionized water (please refer to Appendix A), following the procedure described in section 4.6.4.

# **Chapter 5.**

## **Results and Discussion**

# 5. Results and Discussion

---

## 5.1. Pristine LDHs

### 5.1.1. XRD:

Figure 5-1 presents the XRD spectra for Zn<sub>2</sub>-Cp and Zn<sub>3</sub>-Cp, showing their successful preparation by co-precipitation, that is emphasized by the presence of the characteristic reflections for LDHs. These reflections are divided into two main types: strong basal and intense reflections at low 2θ angles, and other asymmetric broader reflections at higher 2θ angle values [1][6][109]. The sharp reflections are associated to diffraction by planes (003), (006), and (009). The basal spacing  $d_{(003)}$ , which is equal to one interlayer distance plus the thickness of one brucite-like layer can be calculated directly from the peak position of the (003) peak using Bragg's law (equation.1, sector 3.1.1). Thus, the exact interlayer distance is easily calculated by subtracting the thickness of the brucite-like layer (estimated as 4.77 Å as stated by Miyata) [110]. These reflections are also useful in calculating the lattice parameter (c) from either the position of the first peak (equation 8 and 9):

$$c = 3d_{(003)} \quad \text{eq.8}$$

or the average of the three peak positions:

$$c = d_{(003)} + 2d_{(006)} + 3d_{(009)} \quad \text{eq.9}$$

The (009) reflection is usually overlapped with non basal reflections and broad due to disorders of the interlayer anions and water molecules. While the reflections at higher angle values (around  $2\theta \approx 60^\circ$ ), are useful for the determination of the lattice parameter (a): as  $a = 2d_{(110)}$ ; whose value is equal to the distance between two metal cations, and thus, reflecting the radii of the cations [1]. As for the characteristic reflections at the intermediate angles: (012), (015) and (018), these are used to determine the stacking sequence of the layers, and with the values of a and c, are indexed as 3R stacking polytype with hexagonal symmetry [1].

The prepared samples showed the as-mentioned characteristic reflections, agreeing with literature [111], and their lattice parameters, d-spacing and interlayer distances are summarized in table (5-1). The (003) reflection in the case of Zn<sub>2</sub>-Cp had shifted slightly to a lower  $2\theta$  ( $\approx 9.7^\circ$ ) than that of Zn<sub>3</sub>-Cp ( $\approx 10.3^\circ$ ), giving d-spacing values of 9.1 Å and 8.6 Å respectively. Since, c value is greatly dependent on the size, charge and the orientation of the interlayer anions, it increases with the increase of the interlayer distance. In this case, the increase in the basal spacing was due to the decrease of the

metal cations ratio (high x value), indicating higher positive charge density in the brucite-like layers, accommodating more nitrate anions to neutralize the positive charges. These cannot fit in a parallel manner in the interlayer space and hence, are tilted, giving slightly larger d-spacing and c value [111][112]. The increase of the charge density in sample Zn2-Cp is also reflected on the increase of the peaks' intensities compared to sample Zn3-Cp, with a very good agreement with literature reported by Seftel et al [112]. On the other hand, the value of parameter (a) for both samples is almost the same, which indicates its independency of the metal cationic ratio [6].

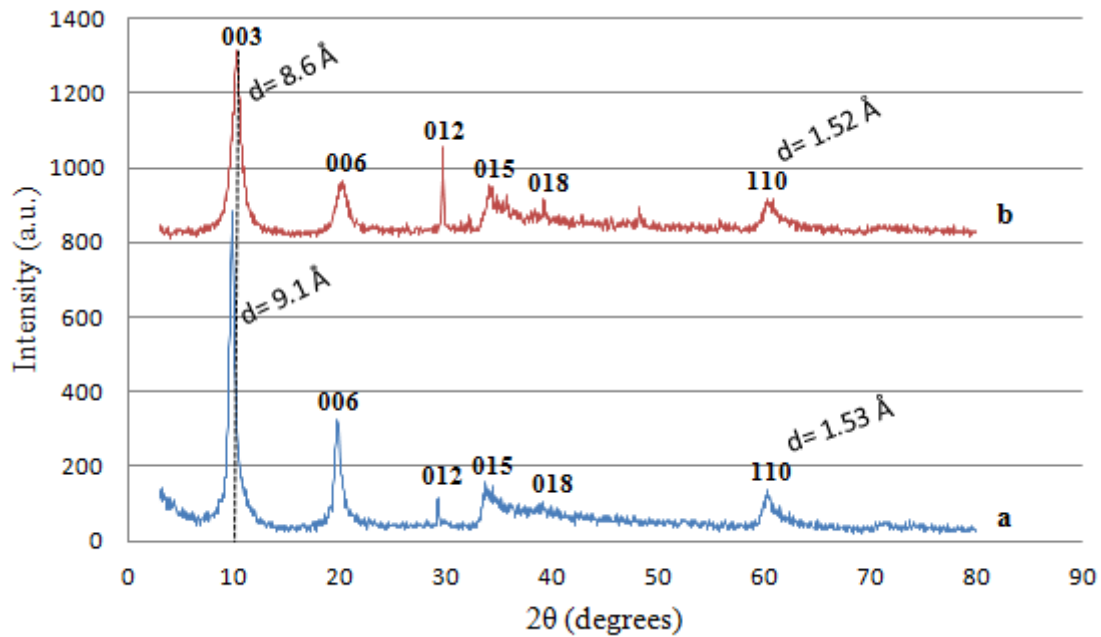


Fig 5-1. XRD patterns of Zn2-Cp (a), and Zn3-Cp (b).

Table 5-1. The lattice parameters, d-spacings and interlayer distances of Zn2-Cp and Zn3-Cp.

Sample	d spacing (Å)		Lattice parameters (Å)		Interlayer distance (Å)
	d(003)	d(110)	c	a	
Zn2-Cp	9.1	1.53	27.3	3.06	4.33
Zn3-Cp	8.6	1.52	25.8	3.04	3.83

### 5.1.2. FTIR:

Figure 5-2 shows the IR spectra of Zn<sub>2</sub>-Cp and Zn<sub>3</sub>-Cp. Both show a broad absorption band at around 3400 cm<sup>-1</sup>, which is attributed to the stretching vibrations of the hydroxyl groups (O-H) in the brucite-like layers or the adsorbed water molecules [6][113]. The peak 1612 cm<sup>-1</sup> is due to the H-O-H bending vibration of the interlayer water molecules. A very sharp characteristic peak at 1384 cm<sup>-1</sup> is attributed to the nitrate group vibration [113]. Peaks showing at low frequency regions: around 800, 600 and 426 cm<sup>-1</sup>, are attributed to vibrations of the metal-oxygen (M-O) and metal-oxygen-metal (M-O-M) bonds in the brucite-like layers [113].

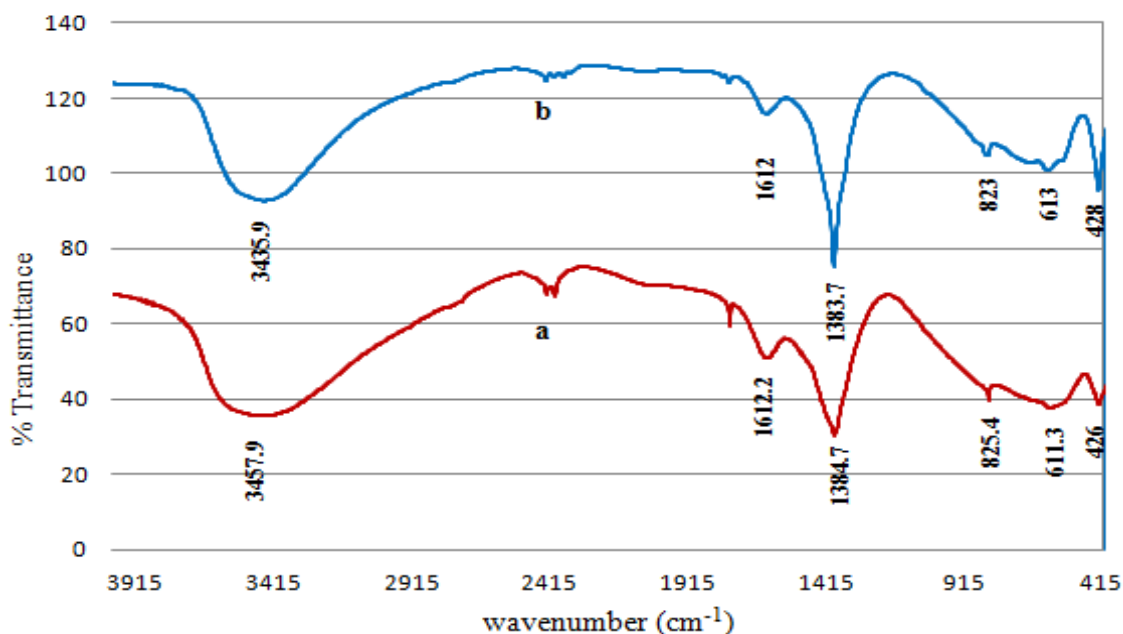


Fig 5-2. FTIR spectra of Zn<sub>3</sub>-Cp (a) and Zn<sub>2</sub>-Cp (b) pristine LDHs.

### 5.1.3. SEM:

Figure 5-3 shows the SEM image of the general structure of Zn-Al-NO<sub>3</sub> LDHs, clearly showing the flake-like structure of the layers [114].

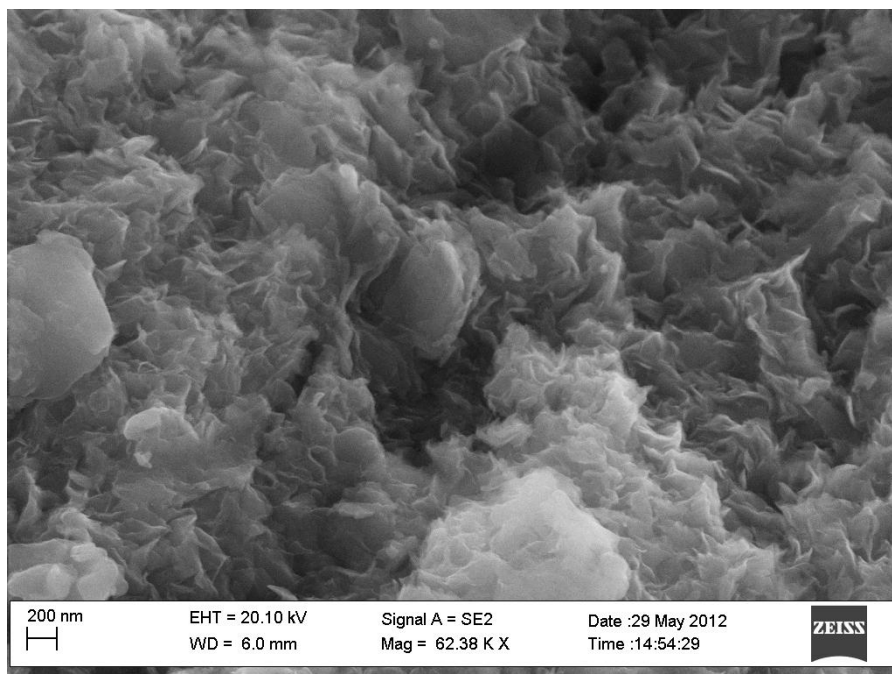


Fig 5-3. SEM image of pristine Zn-Al-NO<sub>3</sub> LDH.



## 5.2. Oxidation of G powder

### 5.2.1. XRD:

The successful oxidation of G into GO sheets, using improved Hummer's method, was proven by the appearance of GO characteristic XRD reflections as shown in figure (5-4). Prior to oxidation, the G showed a very sharp (002) peak at  $2\theta \approx 26.15^\circ$ , having an interlayer spacing of 3.4 Å. Post-oxidation, the (002) peak was greatly shifted to a lower  $2\theta$  value of  $9.1^\circ$ , having an interlayer spacing of 9.7 Å. This increase in the interlayer spacing is attributed to the introduction of oxygenated functional groups at both sides of the G sheets. The small broad peaks at higher  $2\theta$  values indicate the presence of traces from the starting G powder [17][21][23].

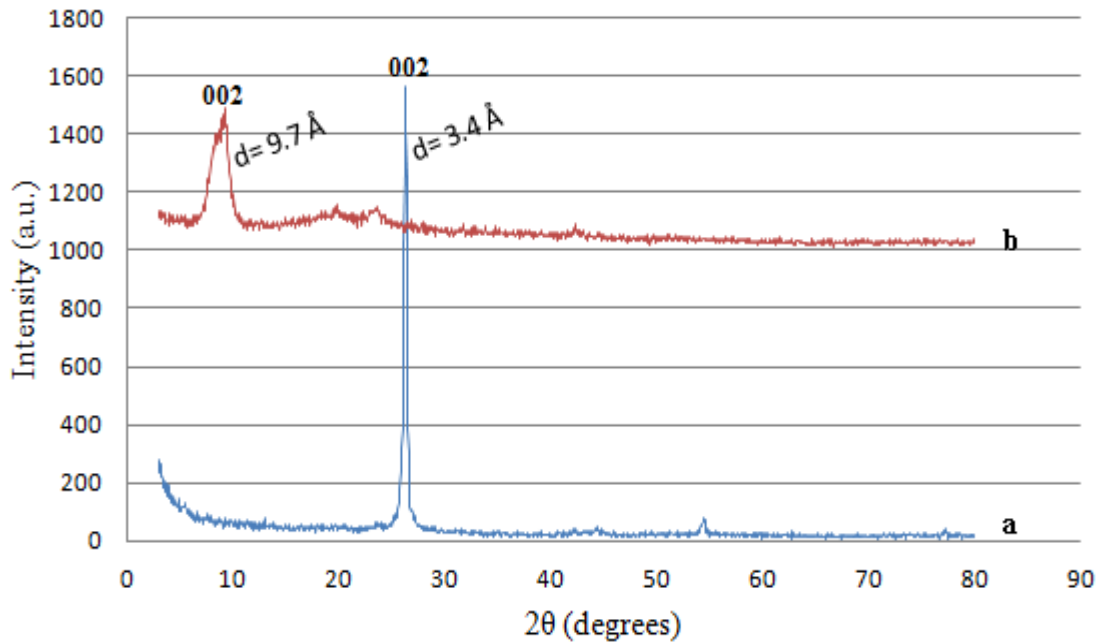


Fig 5-4. XRD patterns of G (a), and GO (b).

### 5.2.2. FTIR:

As shown in figure 5-5, some important vibration bands appeared upon G oxidation, that are related to the introduced oxygenated groups. These vibrations are: O-H stretching vibration, appearing at around  $3400\text{ cm}^{-1}$ . These hydroxyl groups are attributed to both carboxylic acid groups (COOH) and adsorbed water molecules, the band at  $1612\text{ cm}^{-1}$  is also an indication of the O-H bending vibration of the adsorbed water molecules. Bands appearing at  $1726\text{ cm}^{-1}$  is attributed to C=O stretching vibrations, from COOH, ketone or quinone groups. C-O vibration appears at  $1228\text{ cm}^{-1}$ , and C-O-C stretching vibration appears at  $1170\text{ cm}^{-1}$  [20][21][23].

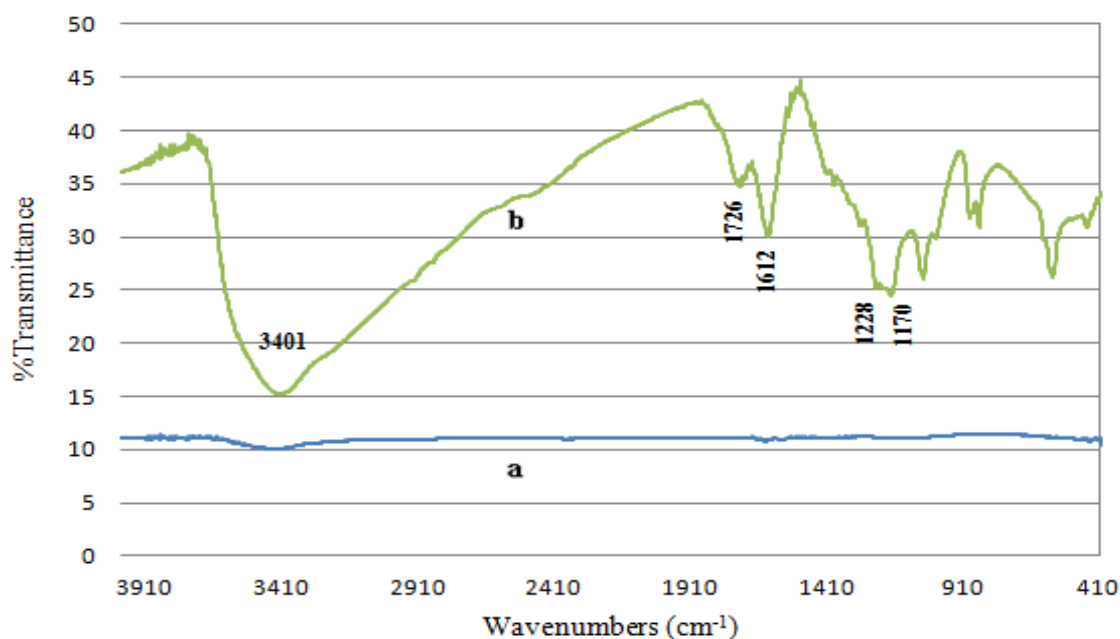


Fig 5-5. FTIR spectra of G (a) and GO (b).

### 5.2.3. SEM:

Figure 5-6 represents the SEM images for the surface morphology of G prior and post oxidation. Prior oxidation, G, showed aggregations of several stacked layers, giving rise to a rough surface appearance. While, post-oxidation the surface of GO sheets was smoother, showing less aggregates, and very few stacked layers; which indicates the successful exfoliation of the G by its oxidation [17][20][21][23].

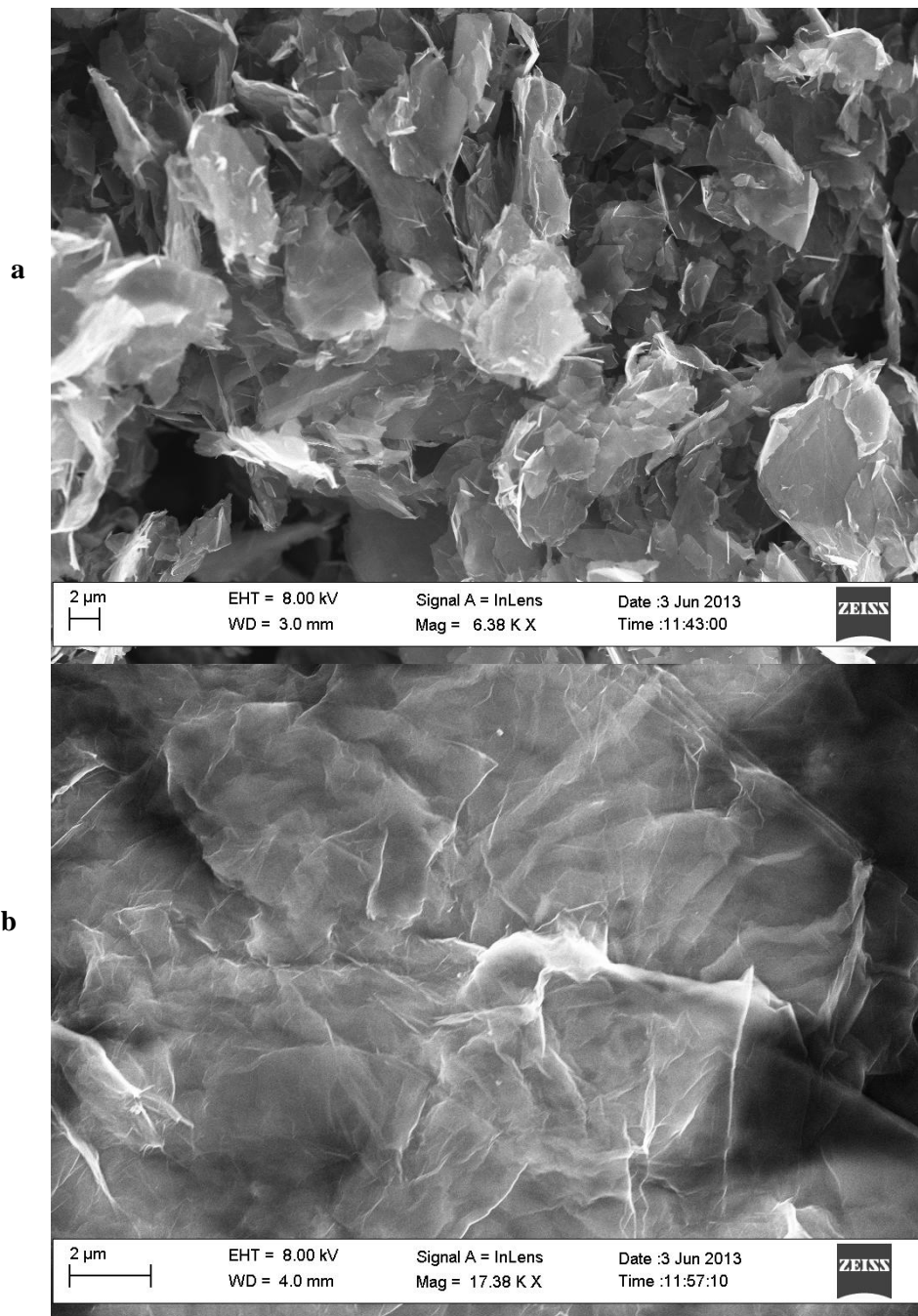


Fig 5-6. SEM images of G (a), and GO (b).

### 5.3. Preparation of G/GO-LDH hybrids

#### **5.3.1. Determining the optimum GO weight percentage in the hybrid (%w/w):**

Figure 5-7 shows the XRD patterns of GO-LDH hybrids, prepared using LDH with  $M^{2+}/M^{3+}$  ratio of 2:1 and different % wt of GO (2, 3.2, and 13.4 % wt). The intensity of the reflections at plane (003) and (006) become less intense and broader with the increase of the % wt of GO (2, 6.2, and 13.4 % wt respectively), which indicates that the GO affects the crystallinity (layer stacking) of the LDH. Therefore, the 2 % wt, was the percentage of choice for both G and GO to be incorporated in all G/GO-LDH hybrid samples as will be shown in the following parts. This minimizes the use of G or GO in the nanocomposite.

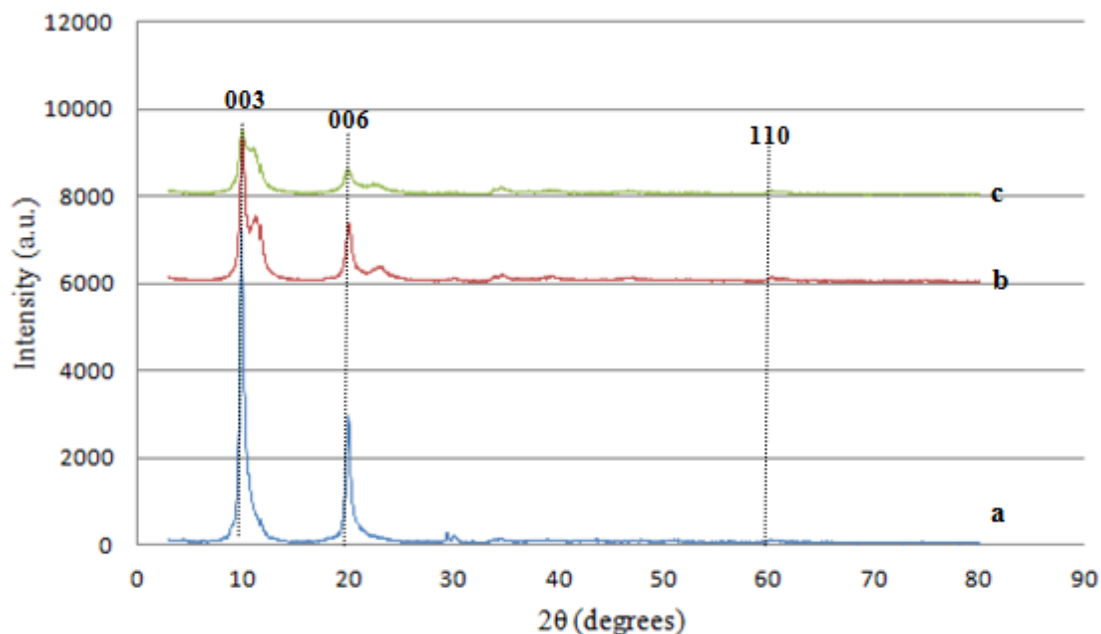


Fig 5-7. GO-LDH hybrids prepared with GO: 2 % (a), 6.2 % (b) and 13.4 % w/w (c).

### **5.3.2. Determining the optimum solution volume for the G and GO dispersion for the preparation of the LDH-G and LDH-GO hybrids:**

#### **A- XRD**

Figures 5-8 to 5-11 present the XRD patterns of G/GO-LDH hybrids, prepared by co-precipitation using different G/GO concentrations (mg/ml) of a fixed amount of G or GO (2 % wt), with LDH of metal cations ratio ( $M^{2+}/ M^{3+}$ ) of 2:1 and 3:1. The values of calculated d(003), d(110) and interlayer spaces of all samples are summarized in table 5-2. For samples prepared using LDH of  $M^{2+}/ M^{3+}$  (2:1), neither the change of G nor the GO concentration has a noticeable effect on the value of d(003), interlayer space, or d(110). Same findings were observed among samples prepared by LDH of  $M^{2+}/ M^{3+}$  ratio (3:1); the LDH parameters has not been affected by either G or GO. In addition the change of the  $M^{2+}/ M^{3+}$  ratio of the LDH is of insignificance as well, but very slight increase of the interlayer space in case of 2:1 was observed, because of the higher positive charge density in the brucite-like layers that accommodates more nitrate anions for neutralization, causing this slight increase [111][112]. When the hybrids were compared to pristine LDH (2:1 and 3:1) controls, the G and GO reflections disappeared and were found to superimpose with those of the LDHs, because G and GO were incorporated in a small weight percentage from the total hybrid weight.

All of the previous observations generally indicate that no intercalation of G or GO has taken place, and the hybrid is rather formed via adsorption on LDH surfaces. Moreover, the intensities of the peaks, which are related to the crystallinity of the LDH samples are not affected by the presence of G or GO.

Based on the above, hybrid samples with the lowest concentration of G or GO (0.04 mg/ml) were chosen for drug loading. This has two advantages: it minimizes the effect of G or GO on the LDH formation, and also ensures minimal possibilities of agglomeration between G or GO in the hybrid samples.

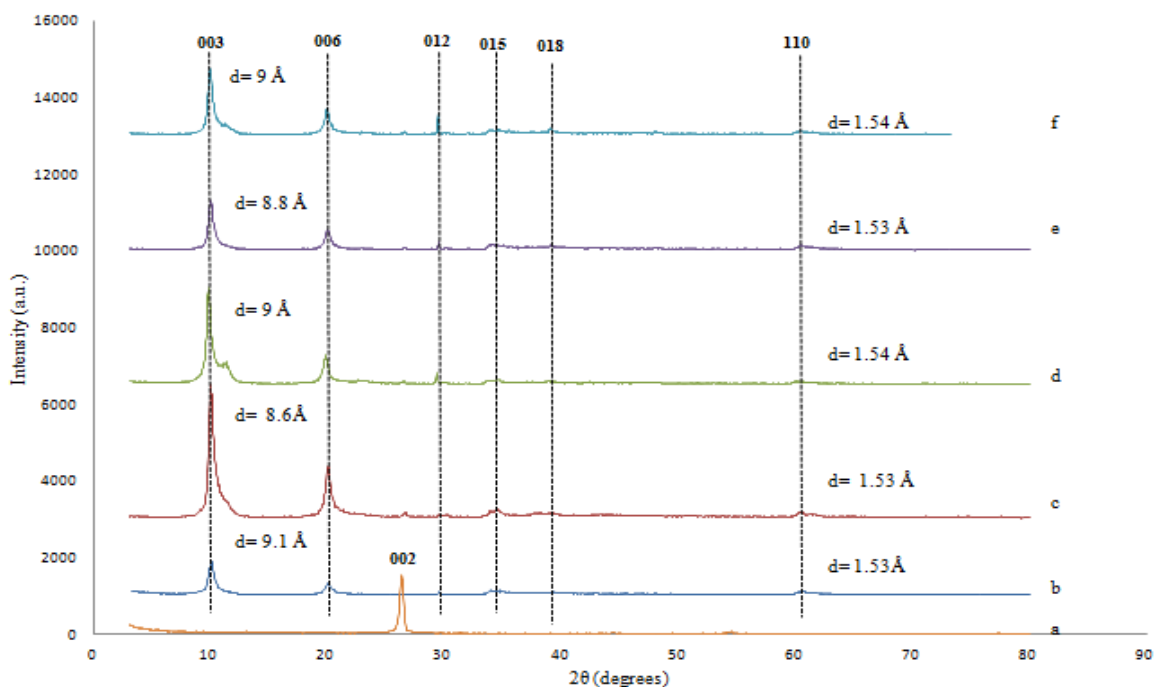


Fig 5-8. XRD patterns of G (a), Zn<sub>2</sub>-Cp (b), Zn<sub>2</sub>-G.04-Cp (c), Zn<sub>2</sub>-G.1-Cp (d), Zn<sub>2</sub>-G.2-Cp (e), and Zn<sub>2</sub>-G.4-Cp (f).

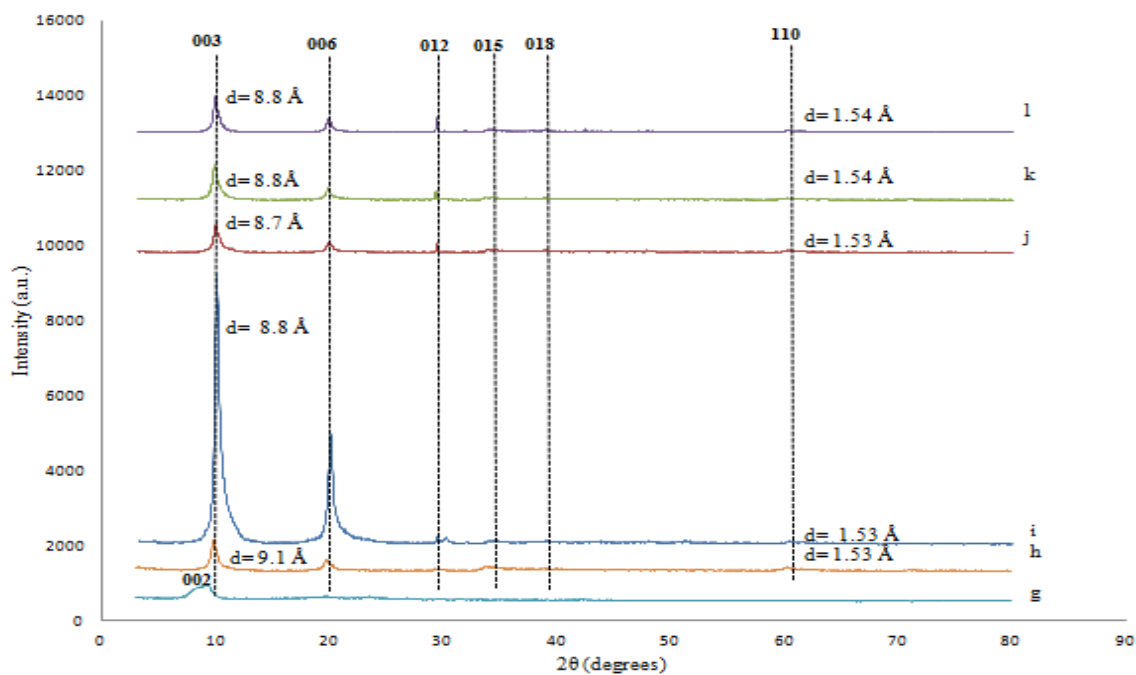


Fig 5-9. XRD patterns of GO (g), Zn<sub>2</sub>-Cp (h), Zn<sub>2</sub>-GO.04-Cp (i), Zn<sub>2</sub>-GO.1-Cp (j), Zn<sub>2</sub>-GO.2-Cp (k), and Zn<sub>2</sub>-GO.4-Cp (l).

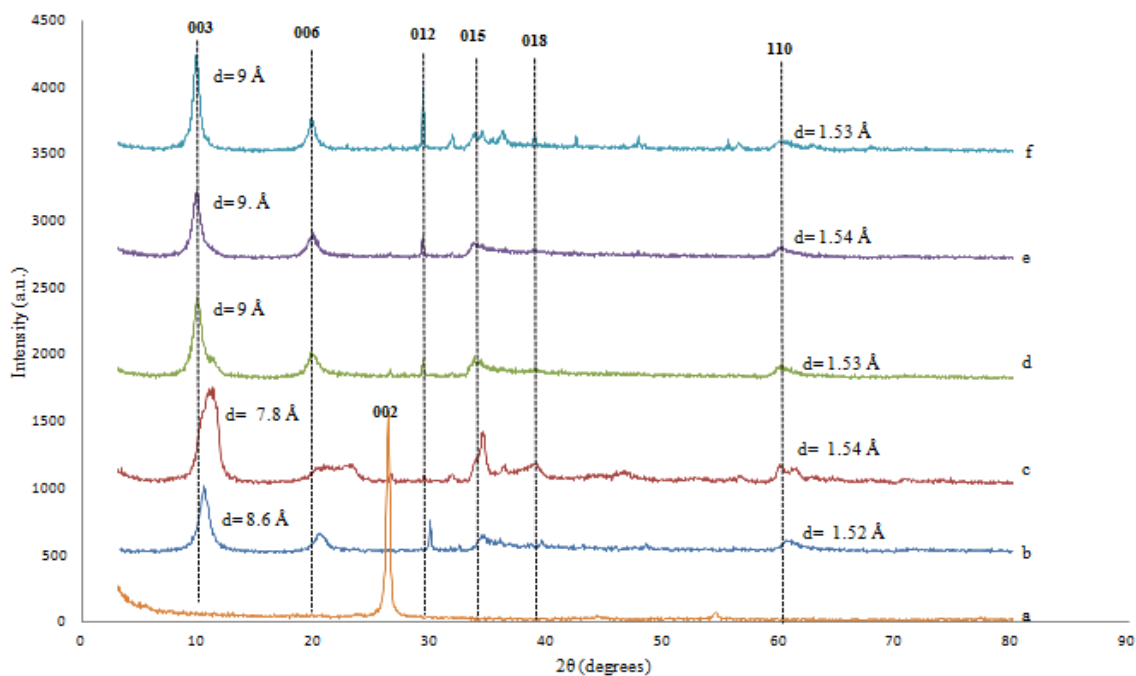


Fig 5-10. XRD patterns of G (a), Zn3-Cp (b), Zn3-G.04-Cp (c), Zn3-G.1-Cp (d), Zn3-G.2-Cp (e), and Zn3-G.4-Cp (f).

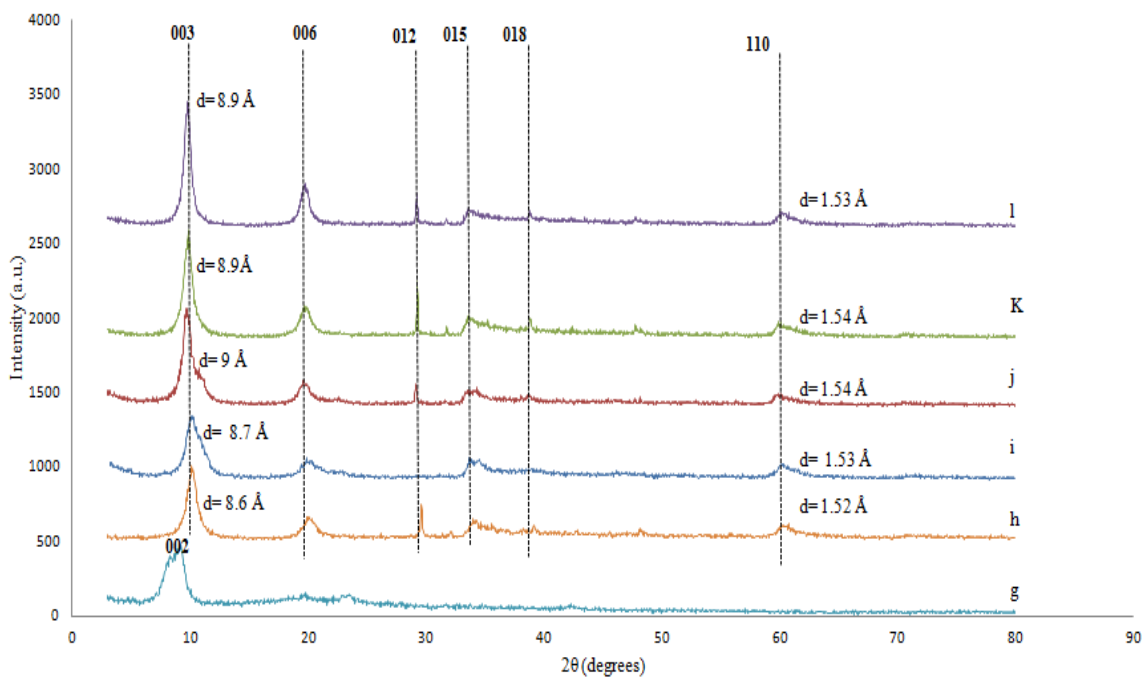


Fig 5-11. XRD patterns of GO (g), Zn3-Cp (h), Zn3-GO.04-Cp (i), Zn3-GO.1-Cp (j), Zn3-GO.2-Cp (k), and Zn3-GO.4-Cp (l).

Table 5-2. The calculated d-spacings and interlayer spaces of prepared G/GO-LDH hybrids, with different concentrations of G and GO (mg/ml) and metal cations ratio of LDH.

Sample	d-spacing (Å)		Interlayer space (Å)	Sample	d-spacing (Å)		Interlayer space (Å)
	d (003)	d (110)			d (003)	d (110)	
Zn2-G.04-Cp	8.6	1.54	3.89	Zn2-GO.04-Cp	8.8	1.53	4.03
Zn2-G.1-Cp	9.0	1.53	4.29	Zn2-GO.1-Cp	8.7	1.53	3.99
Zn2-G.2-Cp	8.8	1.54	4.10	Zn2-GO.2-Cp	8.8	1.54	4.03
Zn2-G.4-Cp	9.0	1.53	4.23	Zn2-GO.4-Cp	8.8	1.54	4.03
Zn3-G.04-Cp	7.8	1.54	3.03	Zn3-GO.04-Cp	8.7	1.53	4.01
Zn3-G.1-Cp	9.0	1.53	4.26	Zn3-GO.1-Cp	9.0	1.54	4.23
Zn3-G.2-Cp	9.0	1.54	4.26	Zn3-GO.2-Cp	8.9	1.54	4.13
Zn3-G.4-Cp	9.0	1.53	4.23	Zn3-GO.4-Cp	8.9	1.53	4.13

## B- FTIR

Figures from 5-12 to 5-15 are FTIR spectra of the prepared G/GO-LDH hybrids. The characteristic bands of pristine LDH are superimposed on those of G and GO. The characteristic broad band at around  $3400\text{ cm}^{-1}$  is attributed to the OH group of the brucite-like layers and the adsorbed water molecules as well as the OH groups of GO where applicable [20][113]. The band at around  $1600\text{ cm}^{-1}$  is due to the H-O-H bending vibration of the interlayer water molecules. Highly intense nitrate band at around  $1384\text{ cm}^{-1}$ , which proves the absence of intercalation of G or GO in the LDH interlayer space. The vibration bands appearing at lower frequencies (around  $400$ ,  $600$ , and  $800\text{ cm}^{-1}$ ) are assigned to the M-O and M-O-M bonds of the brucite-like layer, which indicates that the G and GO have no effect on the brucite-like layers [113].



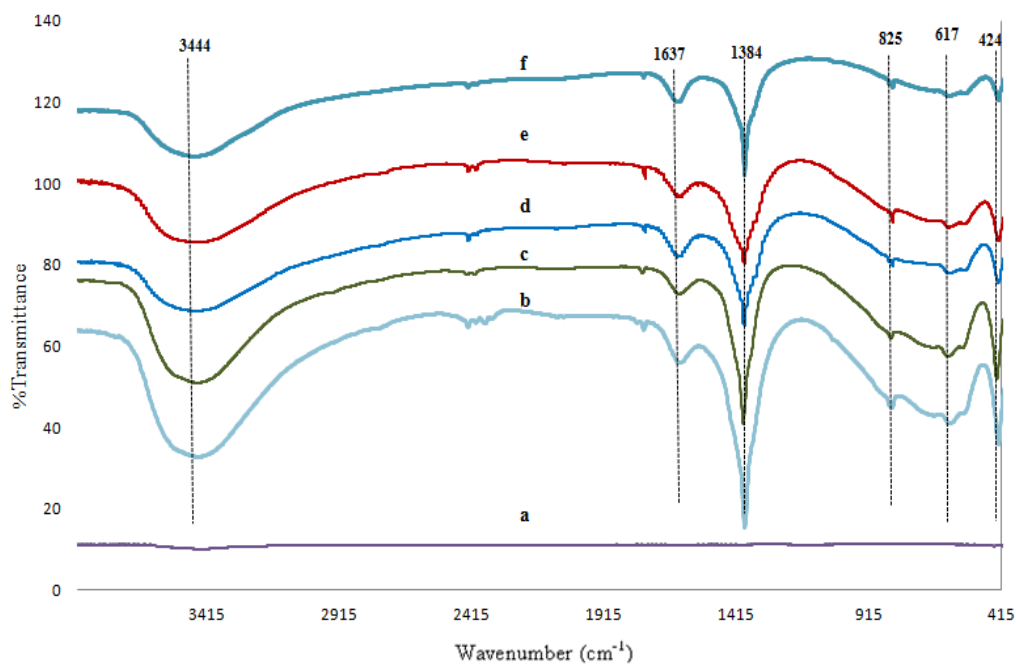


Fig 5-12. FTIR spectra of G (a), Zn<sub>2</sub>-Cp (b) Zn<sub>2</sub>-G.04-Cp (c), Zn<sub>2</sub>-G.1-Cp (d), Zn<sub>2</sub>-G.2-Cp (e), and Zn<sub>2</sub>-G.4-Cp (f).

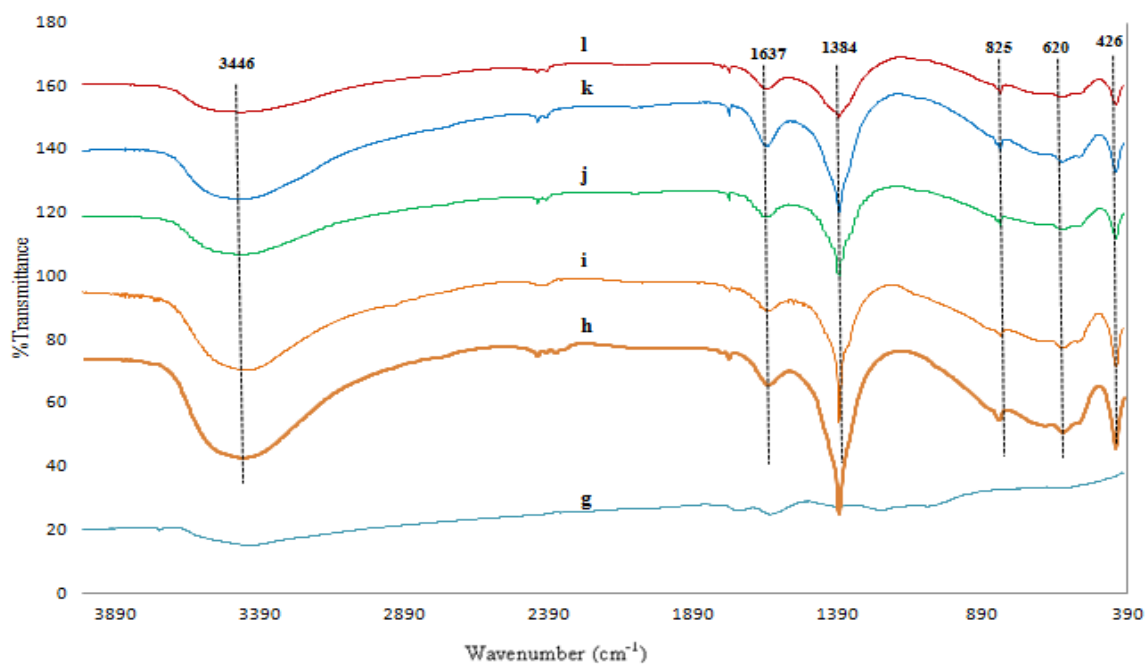


Fig 5-13. FTIR spectra of GO (g), Zn<sub>2</sub>-Cp (h), Zn<sub>2</sub>-GO.04-Cp (i), Zn<sub>2</sub>-GO.1-Cp (j), Zn<sub>2</sub>-GO.2-Cp (k), and Zn<sub>2</sub>-GO.4-Cp (l).

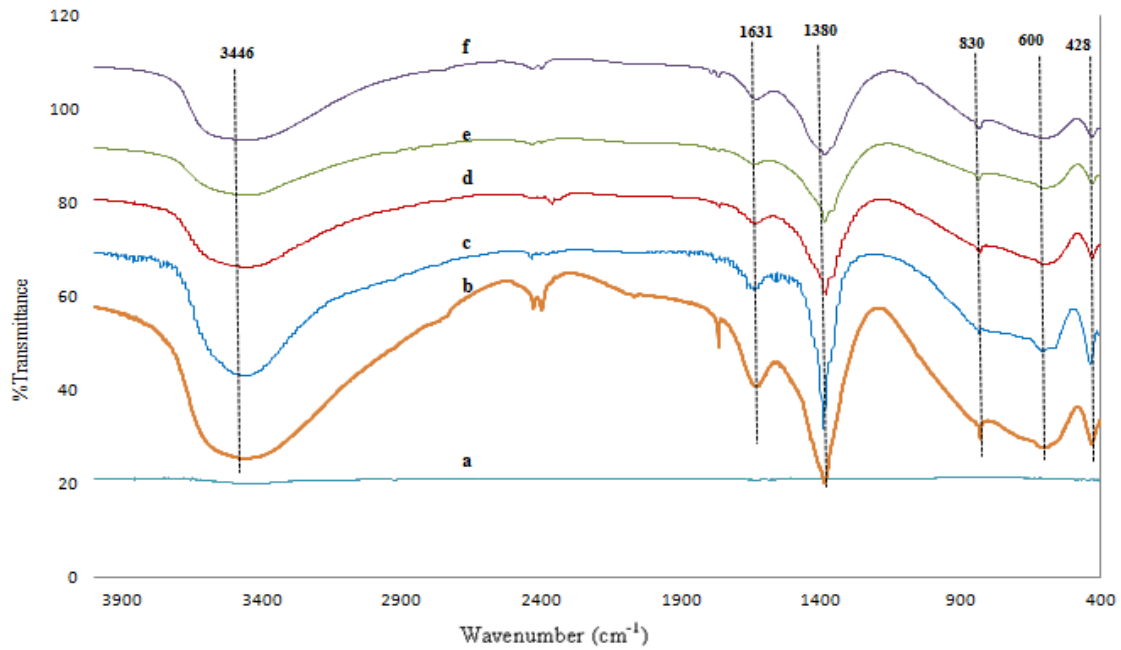


Fig 5-14. FTIR spectra of G (a), Zn3-Cp (b), Zn3-G.04-Cp (c), Zn3-G.1-Cp (d), Zn3-G.2-Cp (e), and Zn3-G.4-Cp (f).

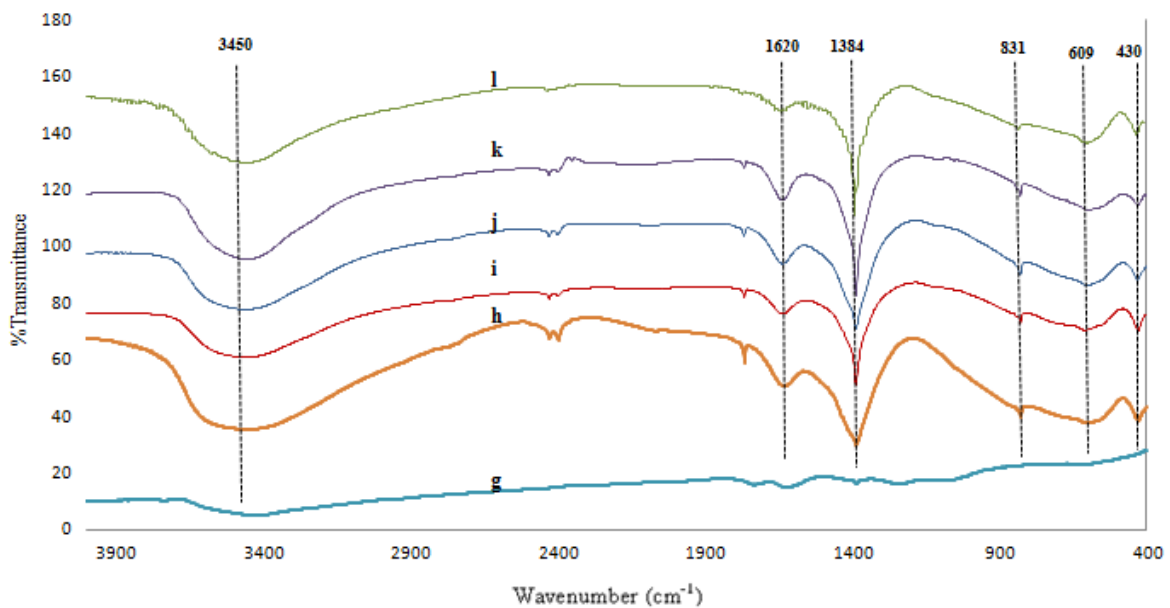


Fig 5-15. FTIR spectra of GO (g), Zn3-Cp (h), Zn3-GO.04-Cp (i), Zn3-GO.1-Cp (j), Zn3-GO.2-Cp (k), and Zn3-GO.4-Cp (l).

## 5.4. Loading of Alendronate sodium

In this section, for each loaded system, the XRD results were analyzed for successful drug intercalation, followed by their FT-IR spectra to confirm the XRD findings. The systems were then tested for their loading efficiency, and those showing best intercalation results are tested for their in-vitro drug release behavior.

### 5.4.1. Co-precipitation samples:

#### A- XRD

Figures 5-16 and 5-17 show the XRD patterns of samples A-Zn3-Cp, A-Zn3-G-Cp and A-Zn3-GO-Cp, which are prepared by co-precipitation using  $M^{2+}/M^{3+}$  ratio of 3:1. All of the three samples showed an obvious shift of the (003) reflection to a lower  $2\theta$  value indicating an expansion in the d-spacing when compared to their corresponding precursors: Zn3-Cp, Zn3-G.04-Cp, and Zn3-GO.04-Cp respectively, as summarized in table 5-3.

A-Zn3-Cp, (figure 5-16), showed a huge shift of the (003) reflection to a lower  $2\theta$  of  $4.8^\circ$ ; corresponding to an expansion of the  $d(003)$  from  $8.6 \text{ \AA}$  to  $18.3 \text{ \AA}$ . When subtracting the brucite-like layer thickness ( $4.77 \text{ \AA}$ ), the interlayer space is calculated to be  $13.5 \text{ \AA}$  [110]. The expansion of the interlayer space suggests the successful intercalation of alendronate sodium. The interlayer gallery ( $13.5 \text{ \AA}$ ) is greater than the maximum height of one drug anion ( $6.1 \text{ \AA}$ ) [115][116], suggesting drug intercalation in a bi-layered arrangement [55][61][104]. These results are similar to those reported for the intercalation of Ketoprofen, with the most comparable molecular size value ( $8.2 \text{ \AA}$ ) in Mg/Al system, giving an interlayer distance of  $17.2 \text{ \AA}$ , suggesting its intercalation as slightly tilted bi-layer [60]. In addition, the broadening of the reflections along the XRD pattern is an indication of decreased crystallinity post drug's intercalation [61]. The calculated d value for plane (110) is  $1.53 \text{ \AA}$ , which is almost the same as that of the precursor ( $1.52 \text{ \AA}$ ), therefore, the brucite-like layers are not affected by the hosted drug [61].

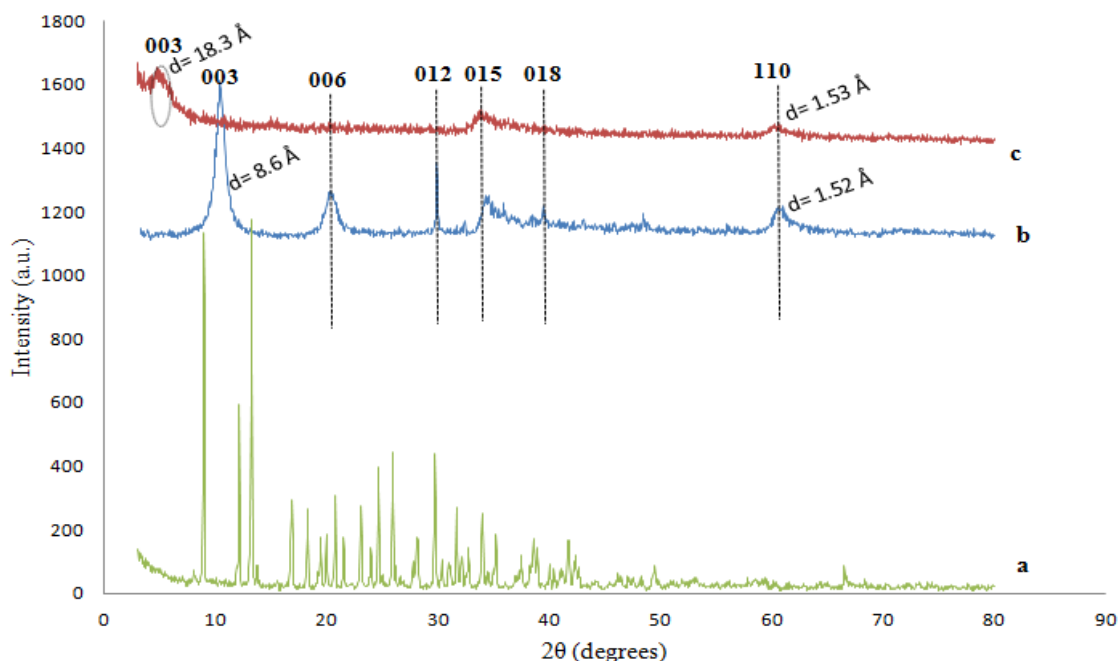


Fig 5-16. XRD patterns of alendronate sodium (a), pristine LDH Zn<sub>3</sub>-Cp (b), and A-Zn<sub>3</sub>-Cp (c).

For samples A-Zn<sub>3</sub>-G-Cp and A-Zn<sub>3</sub>-GO-Cp (figure 5-17), the reflection at (003) shifted to lower  $2\theta$  values of  $4.77^\circ$  and  $4.98^\circ$ , giving an expansion of the  $d(003)$  of  $18.5 \text{ \AA}$  and  $17.73 \text{ \AA}$  respectively when compared to their precursors,  $7.8$  and  $8.7 \text{ \AA}$  respectively. Subtracting the brucite-like layer thickness ( $4.77 \text{ \AA}$ ), the interlayer distances are calculated as  $13.7 \text{ \AA}$  and  $12.9 \text{ \AA}$  respectively [110]. The reflection peaks of the G or GO don't appear, being superimposed by those of the LDH phase [117]. The expansion of the interlayer spacing can be explained by the successful intercalation of the drug in a bi-layered arrangement ( $12.2 \text{ \AA}$ ). While drug loaded on G or GO surface is probably adsorbed on the surface of the LDH. The preparation of a drug loaded G/GO-LDH nanocomposite by co-precipitation was not reported by others in the literature, but rather the loading of antibacterial benzyl penicillin by ionic exchange using solvent evaporation process has been reported. Their XRD results for GO-benzyl penicillin-LDH were similar to that of the benzyl penicillin-LDH, that by turn has shown a bi-layered arrangement of the drug ( $11.7 \text{ \AA}$ ), attributed to the interlayer distance of  $17.4 \text{ \AA}$ . The non significant effect of the GO on the drug-LDH reflection indicated its surface adsorption rather than intercalation [61].

The presence of G or GO may have prevented the proper stacking of the brucite-like layers during co-precipitation leading to a decrease in crystallinity, indicated by the broadening of the XRD reflections, especially that at plane (003) [6][55][61]. This is indeed more noticeable for sample A-Zn<sub>3</sub>-G-Cp, probably due to G tending to

agglomerate by  $\pi$ - $\pi$  stacking, and thus preventing the layer stacking of the LDH. This is indicated by the slight increase in the interlayer space for this sample as compared to that of A-Zn3-GO-Cp [6][118][119].

The calculated d values for plane (110), in both samples are the same as that of their precursors (1.54 and 1.53 Å respectively), which is an indication that the brucite-like layers remained unchanged and not affected by the presence of either G or GO [61].

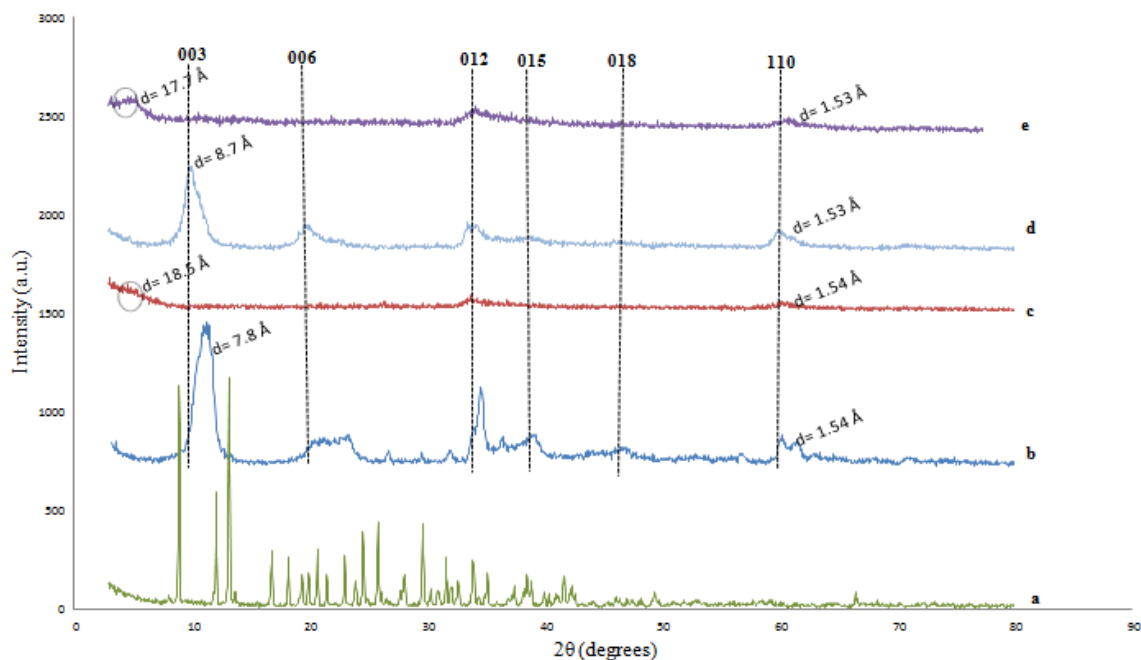


Fig 5-17. XRD patterns of alendronate sodium (a), Zn3-G.04-Cp (b), A-Zn3-G-Cp (c), Zn3-GO.04-Cp (d), and A-Zn3-GO-Cp (e).

Table 5-3. Comparison between the parameters of the loaded samples prepared by co-precipitation using metal cations ratio of 3:1 and their controls.

Before drug loading				After drug loading					
Sample precursor	2θ (at 003 plane)	d-spacing (Å)		Interlayer space (Å)	Loaded Sample	2θ (at 003 plane)	d-spacing (Å)		Interlayer space (Å)
		d (003)	d (110)				d (003)	d (110)	
Zn3-Cp	10.3°	8.6	1.52	3.83	A-Zn3-Cp	4.8°	18.3	1.53	13.53
Zn3-G.04-Cp	11.3°	7.8	1.54	3.00	A-Zn3-G-Cp	4.8°	18.5	1.54	13.70
Zn3-GO.04-Cp	10.1°	8.7	1.53	4.02	A-Zn3-GO-Cp	5.0°	17.7	1.53	12.90

Figure 5-18 and 5-19, show XRD patterns of samples A-Zn2-Cp, A-Zn2-G-Cp and A-Zn2-GO-Cp, which are prepared by co-precipitation, using a  $M^{2+}/M^{3+}$  ratio of 2:1. The samples were compared to their corresponding precursors: Zn2-Cp, Zn2-G.04-Cp and Zn2-GO.04-Cp respectively.

The XRD pattern of A-Zn2-Cp (figure 5-18) shows an obvious collapse of the LDH layered structure. The very weak reflections at high  $2\theta$  values are attributed to the metal oxides of the disordered brucite like layers [104][111]. It is suggested that the ratio used for the  $M^{2+}/M^{3+}$  (2:1), is rendering the brucite-like layers more positive than the 3:1 ratio, and therefore, the LDH structure would need to accommodate more negatively charged anions to neutralize these charges. However, the large size of the drug molecule cannot fit in the interlayers, and fails to neutralize the positively charged brucite-like layers and hinders its proper stacking, and thus resulting in the loss of the of layered structure of LDH [6][119].

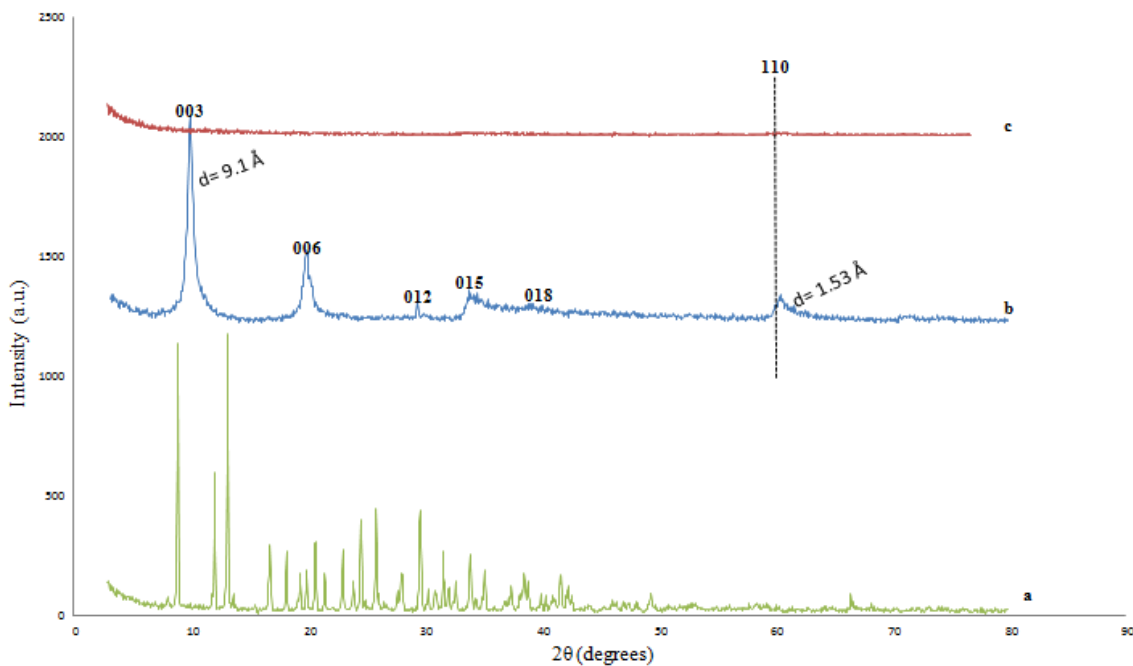


Fig 5-18. XRD patterns of alendronate sodium (a), pristine LDH Zn2-Cp (b), and A-Zn2-Cp (c).

The XRD patterns of A-Zn2-G-Cp and A-Zn2-GO-Cp (figure 5-19), show same XRD features as previous sample (A-Zn2-Cp), indicating the collapse of the LDH layered structure. All three samples (A-Zn2-Cp, A-Zn2-G-Cp, and A-Zn2-GO-Cp), show traces of reflections at high  $2\theta$ , that correspond to the metal oxide of the disordered brucite-like layers [104][111].

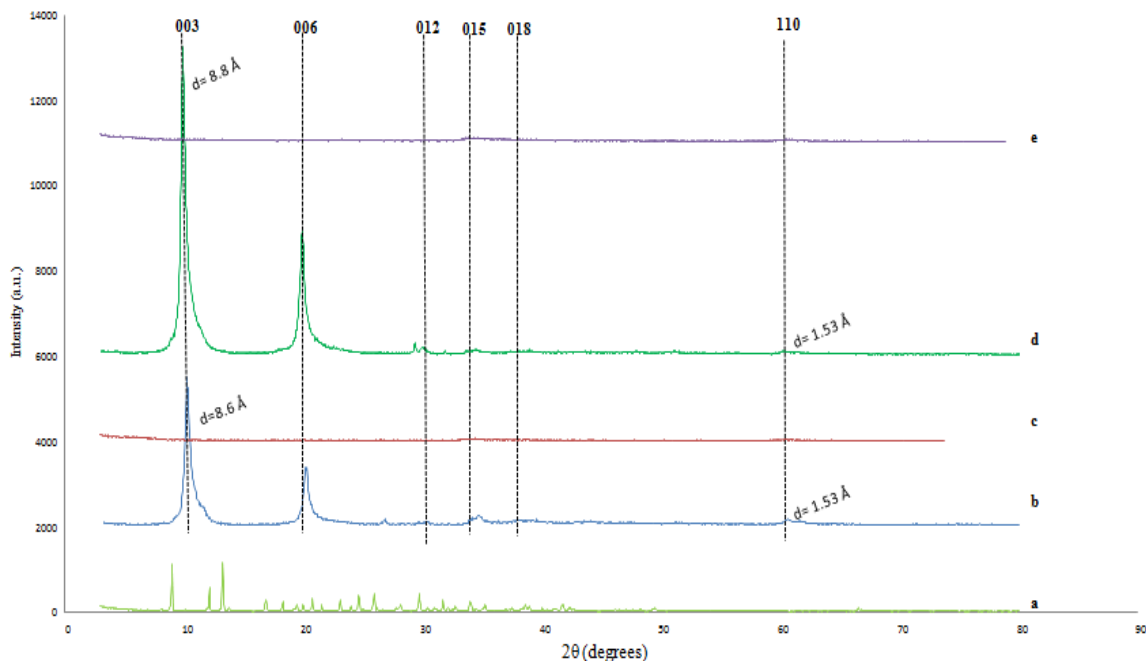


Fig 5-19. XRD patterns of alendronate sodium (a), Zn<sub>2</sub>-G.04-Cp (b), A-Zn<sub>2</sub>-G-Cp (c), Zn<sub>2</sub>-GO.04-Cp (d), and A-Zn<sub>2</sub>-GO-Cp (e).

## B- FTIR

Figure 5-20 shows the FTIR spectra of A-Zn<sub>3</sub>-Cp compared to its precursor (Zn<sub>3</sub>-Cp) and free alendronate sodium. The loaded system (A-Zn<sub>3</sub>-Cp) shows the pristine LDH characteristic broad band at around 3442 cm<sup>-1</sup>, that is attributed to the OH groups of the brucite-like layers and the adsorbed water molecules, as well as the OH group in the free alendronate sodium. This band overlaps with the stretching vibration band of N-H (primary amine) of the free alendronate sodium, that appears in the range of 3400-3250 cm<sup>-1</sup> [56][106][113]. The band at around 1641 cm<sup>-1</sup> is due to the H-O-H bending vibration of the interlayer water molecules of the LDH. The decrease in intensity suggests a disturbance in the interlayer water molecules. The intensity of the nitrate band at 1383 cm<sup>-1</sup> in pristine LDH has noticeably decreased in the loaded sample (A-Zn<sub>3</sub>-Cp), indicating the displacement of the nitrate anions by alendronate sodium [113][120]. However, the incomplete disappearance of the band may indicate the presence of some retained nitrate anions [1]. The free drug shows distinctive bands between 925 and 1238 cm<sup>-1</sup>, which are attributed to the stretching vibrations of C-O and P=O bonds. In the loaded sample, these peaks were shifted, and overlapped, giving a broader peak at around 1118 cm<sup>-1</sup>. This suggests a hydrogen-bond interaction with the brucite-like layers [121][122]. The peaks appearing in pristine LDH at 576.6 and 971 cm<sup>-1</sup>, assigned to the M-O and M-O-M bonds of the LDH [113], are down shifted in the loaded sample from

their original frequencies (428, 606, 831  $\text{cm}^{-1}$ ), to 576 and 971  $\text{cm}^{-1}$ , suggesting a guest-host interaction between the drug and the OH groups of the brucite-like layers, which is also supported by their overlap with the 1118  $\text{cm}^{-1}$  band of the loaded drug [113]. This confirms the successful intercalation of the alendronate sodium into the LDH interlayer, as has been suggested.

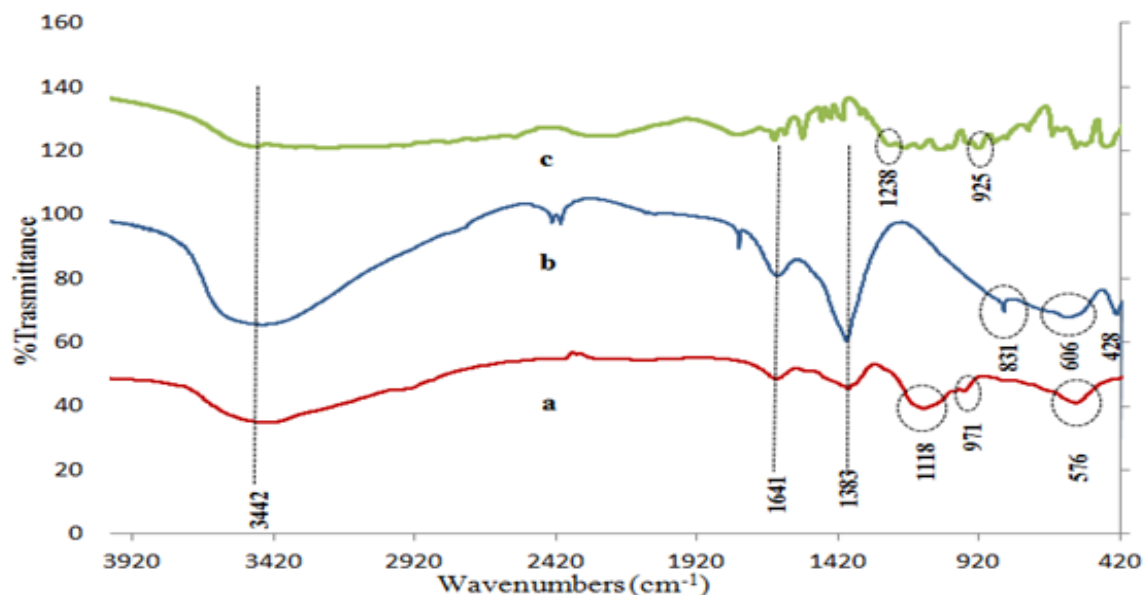


Fig 5-20. FTIR spectra of A-Zn3-Cp (a), Zn3-Cp (b), and alendronate sodium (c).

Figure 5-21 and 5-22 show the FTIR spectra of A-Zn3-G-Cp and A-Zn3-GO-Cp compared to their corresponding precursors Zn3-G.04-Cp and Zn3-GO.04-Cp respectively, as well as free alendronate sodium. Both loaded systems have same interpretation bands' features as the above sample (A-Zn3-Cp) as follows:

- OH broad band at around 3440  $\text{cm}^{-1}$  ( that also corresponds to the COOH of GO in sample A-Zn3-GO-Cp).
- H-O-H bending vibration band at around 1620  $\text{cm}^{-1}$ .
- Nitrate band at around 1384  $\text{cm}^{-1}$ .
- C-O and P=O stretching bands of alendronate sodium for sample A-Zn3-G-Cp and A-Zn3- GO-Cp at 1116 and 1114  $\text{cm}^{-1}$  respectively.
- M-O and M-O-M vibration bands at around 600 and 940  $\text{cm}^{-1}$ .

The decrease in the nitrate band intensity indicates its displacement with the drug. This decrease is more noticeable in these two samples (A-Zn3-G-Cp and A-Zn3-GO-Cp) than



that of A-Zn3-Cp, because the expansion of the interlayer spaces as observed in their XRD patterns indicates an increased amount of intercalated drug. The intercalation is also proven by the overlap and the shift of the alendronate sodium band giving a single broad band, and the down shift of M-O and M-O-M bands [113][121][122].

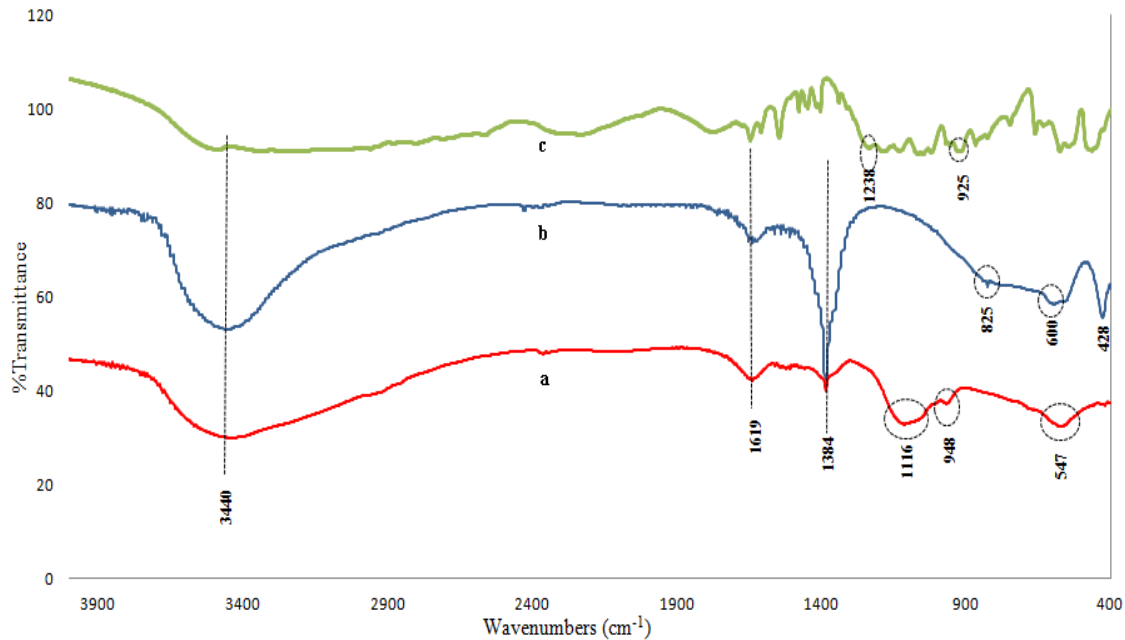


Fig 5-21. FTIR spectra of A-Zn3-G-Cp (a), Zn3-G.04-Cp (b), and alendronate sodium (c).

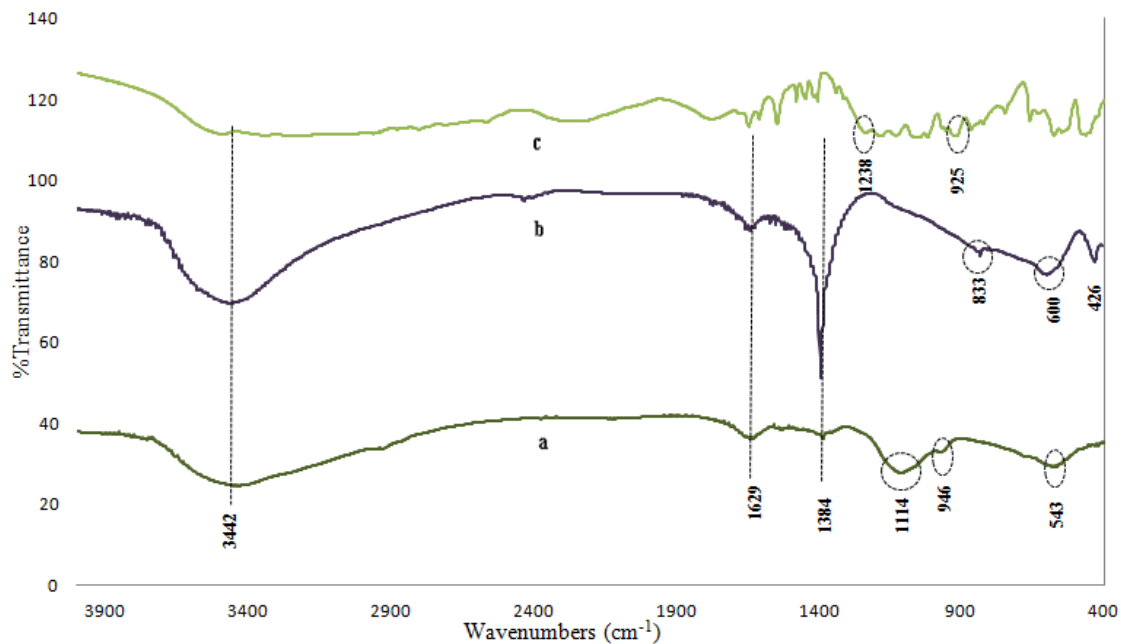


Fig 5-22. FTIR spectra of A-Zn3-GO-Cp (a), Zn3-GO.04-Cp (b), and alendronate sodium (c).

Figure 5-23, shows the FTIR spectra of A-Zn<sub>2</sub>-Cp compared to its precursor Zn<sub>2</sub>-Cp and free alendronate sodium. As mentioned previously, the XRD result for A-Zn<sub>2</sub>-Zp, has shown a collapse in the LDH structure, with only traces of reflections corresponding to the disordered brucite-like layers. Therefore, the FTIR shows the characteristic peaks for the LDH as discussed previously, which mainly correspond to the brucite-like layers in addition to other features as follows:

- OH vibration broad band at around 3440 cm<sup>-1</sup>.
- H-O-H bending vibration band at 1640 cm<sup>-1</sup>.
- Nitrate band at 1384 cm<sup>-1</sup>.
- C-O and P=O stretching vibration bands of the alendronate sodium appears at 1112 cm<sup>-1</sup>.
- M-O and M-O-M vibration bands at 426 and 580 cm<sup>-1</sup>.

The nitrate band intensity is noticeable due to failure of intercalation. However, it is of low intensity than that of the precursor, due to the loss of the nitrate anions neutralizing the brucite-like layers. In addition, The presence of the characteristic band of the drug, indicates its presence in the LDH environment. This can possibly indicate the alendronate sodium adsorption on the surface of the brucite-like layers. Although most of the M-O and the M-OM bands are still at their original frequencies, one of which is down shifted and overlapping with that of the drug (1112 cm<sup>-1</sup>), which could explain the presence of weak hydrogen bonding between the drug and the brucite-like layers [121][122].

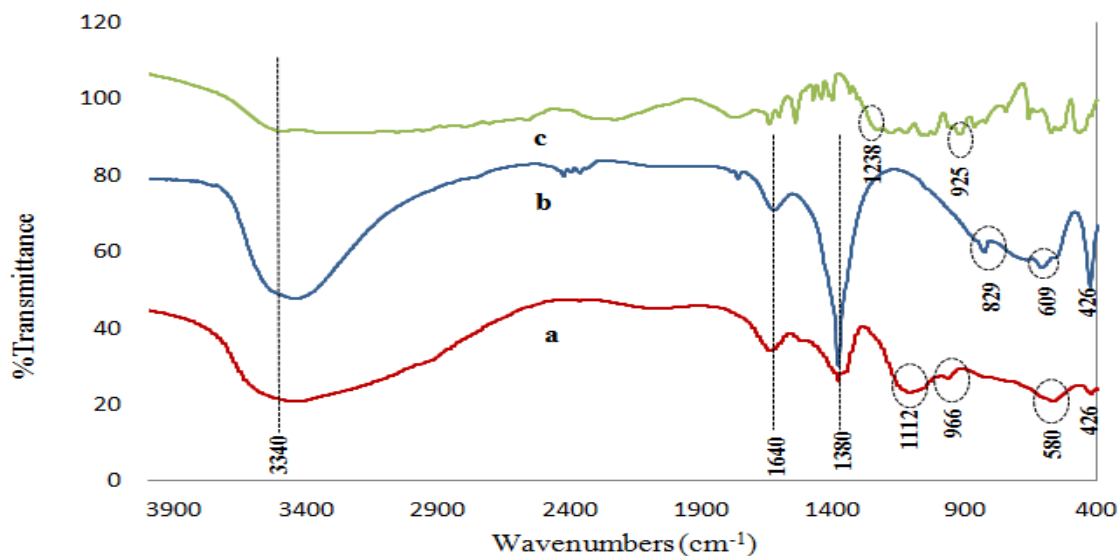


Fig 5-23. FTIR spectra of A-Zn<sub>2</sub>-Cp (a), Zn<sub>2</sub>-Cp (b), and alendronate sodium (c).

Figure 5-24 and 5-25 show the FTIR spectra of A-Zn2-G-Cp and A-Zn2-GO-Cp respectively, which have the same FTIR features and interpretation as in previous sample (A-Zn2-Cp), as follows:

- OH broad band at around  $3440\text{ cm}^{-1}$ .
- H-O-H bending vibration band at  $1630\text{ cm}^{-1}$ .
- Nitrate band at  $1380\text{ cm}^{-1}$ .
- C-O and P=O stretching bands of the alendronte sodium at around  $1110\text{ cm}^{-1}$ .
- M-O and M-O-M vibration bands around  $570$  and  $960\text{ cm}^{-1}$ .

The M-O and M-O-M bands in these two samples (A-Zn2-G-Cp and A-Zn2-GO-Cp), are all down shifted to around  $570$  and  $960\text{ cm}^{-1}$ , compared to previous sample (A-Zn2-Cp), which indicates the presence of stronger hydrogen bonding of drug loaded on the G or GO and brucite-like layers.

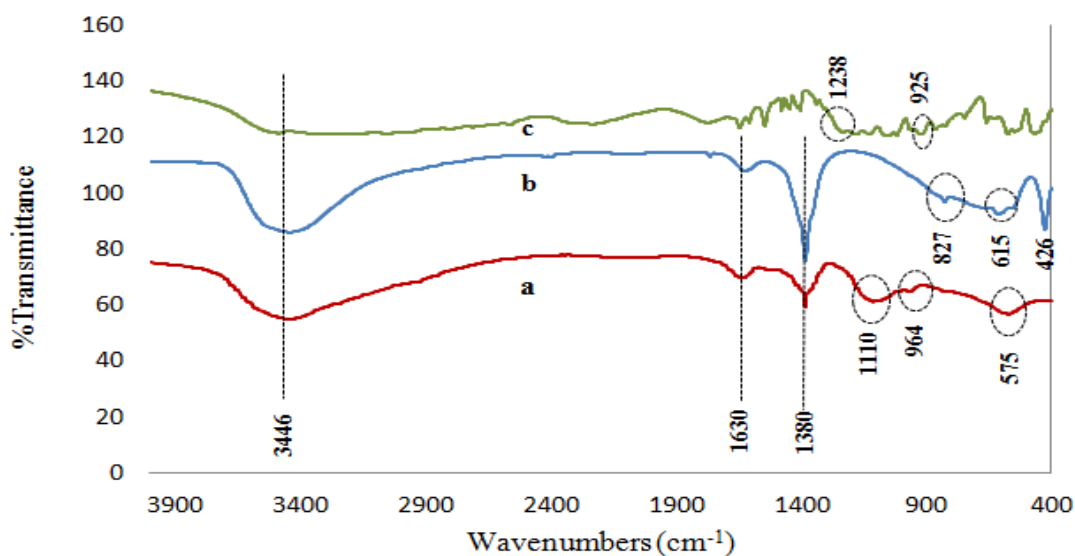


Fig 5-24. FTIR spectra of A-Zn2-G-Cp (a), Zn2-G.04-Cp (b), and alendronate sodium (c).

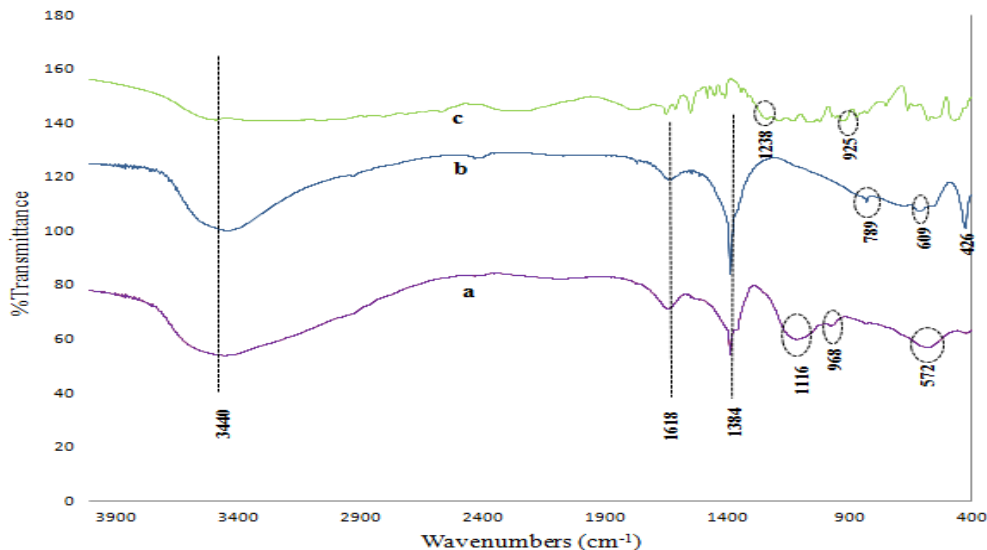


Fig 5-25. FTIR spectra of A-Zn2-GO-Cp (a), Zn2-GO.04-Cp (b), and alendronate sodium (c).

## 5.4.2. Ion-exchange samples:

### A- XRD

Figures 5-26 and 5-27 show the XRD patterns of samples A-Zn3-IE, A-Zn3-G-IE and A-Zn3-GO-IE, which are prepared by loading the free drug dissolved in an aqueous media by ion exchange with the dispersed precursor Zn3-Cp, Zn3-G.04-Cp and Zn3-GO.04-Cp respectively. The parameters are calculated and summarized in table 5-4.

XRD pattern of sample A-Zn3-IE (figure 5-26), shows a huge downshift of  $2\theta$  from  $10.3^\circ$  to  $4.74^\circ$ , to give a  $d(003)$  expansion of  $\approx 18.62 \text{ \AA}$ , and by subtracting the brucite-like layer thickness ( $4.77 \text{ \AA}$ ), the calculated interlayer distance is equal to  $13.82 \text{ \AA}$ , suggesting the intercalation of the drug in a bi-layered arrangement [55][61][104]. The peak at (003) is broad and of low intensity, indicating disturbance of the layer stacking to some extent [6][55]. However, the reflections at (006), (012), and (110) suggest that the LDH structure somehow still keeps its integrity and is not completely distorted. The calculated  $d$  value for the (110) plane is  $1.52 \text{ \AA}$ , which is as same as that of the precursor, indicating that the brucite-like layers are not affected during ion exchange [61]. These are similar to findings reported by Ambrogi et al. for the intercalation of diclofenac in Mg/Al LDH by ion exchange, suggesting their arrangement as bi-layers, which was indicated by the interlayer distance value compared to the drug molecule height [58]. The  $d$ -spacing

expansion value is also similar to those reported by literature (Michelle Chakraborti 2011), for intercalation of alendronate sodium in Mg/Al LDH giving an interlayer distance of 12.8 Å [124].

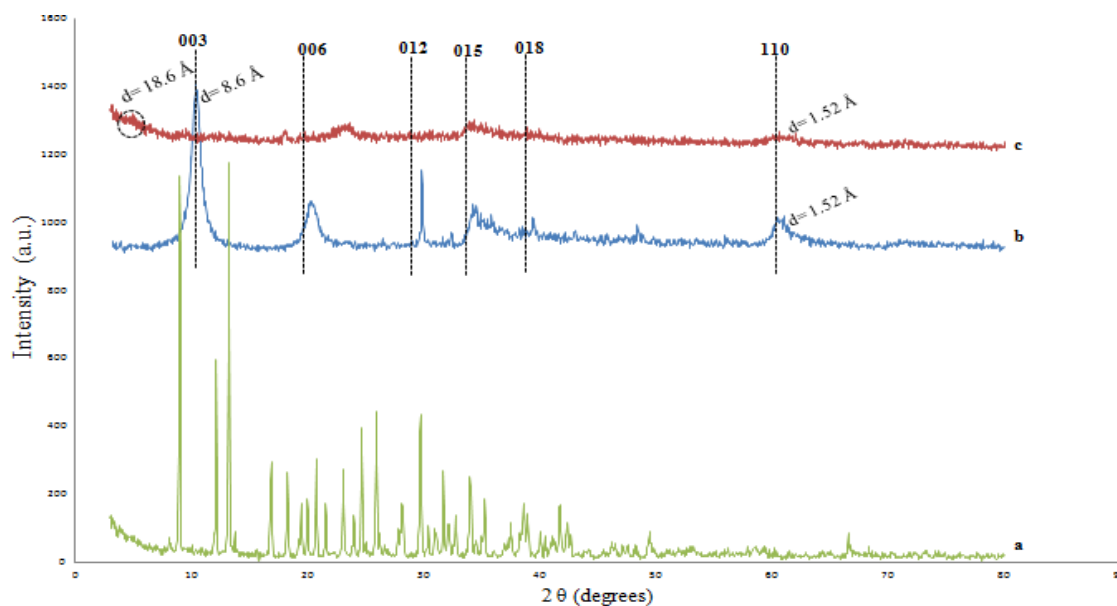


Fig 5-26. XRD patterns of alendronate sodium (a), pristine LDH Zn<sub>3</sub>-Cp (b), and A-Zn<sub>3</sub>-IE (c).

The XRD patterns of samples A-Zn<sub>3</sub>-G-IE and A-Zn<sub>3</sub>-GO-IE (figure 5-27), show a very slight shift of the peak at plane (003) to a higher  $2\theta$  of  $11.79^\circ$  and  $11.2^\circ$ , corresponding to d-spacing values of 7.5 and 7.85 Å respectively. When subtracting the brucite-like layer thickness (4.77 Å), the calculated interlayer gallery heights are 2.73 and 3.09 Å for Zn<sub>3</sub>-G.04-Cp and Zn<sub>3</sub>-GO.04-Cp respectively [110]. The interlayer gallery height is lower than the maximum height of one drug molecule (6.1 Å) [114][116]. Moreover, the size of carbonate is 1.31Å, which excludes the possibility of contamination with dissolved carbonate [6][102][123]. This therefore seems to indicate that no exchange reaction has taken place. The slight interlayer compaction could be due to the loss of some nitrate anions during the high contact with the solution (24 hr). In both samples, the significance of the reflections at (006), (012), and (110) suggests that the LDH structure still keeps its integrity and is not completely distorted [1][111]. The calculated d values for the (110) planes of both samples are 1.54 and 1.534 Å respectively, which indicates that the brucite-like layers are intact [61]. These findings were different than the previously mentioned study by Wang et al., reporting the preparation of GO-benzyl penicillin-LDH nanocomposite by ionic exchange using solvent evaporation process [61]. The nanocomposite have shown a successful intercalation of the drug in bi-layered arrangement, and surface adsorption of the GO. This difference is attributed to the

different preparation techniques used. Where the GO suspension is mixed with that of benzyl penicillin-LDH and allowed to evaporate under temperature [61]. While in this paper, the drug is rather mixed with as-prepared G or GO-LDH precursor, and allowed to stir for long period of time.

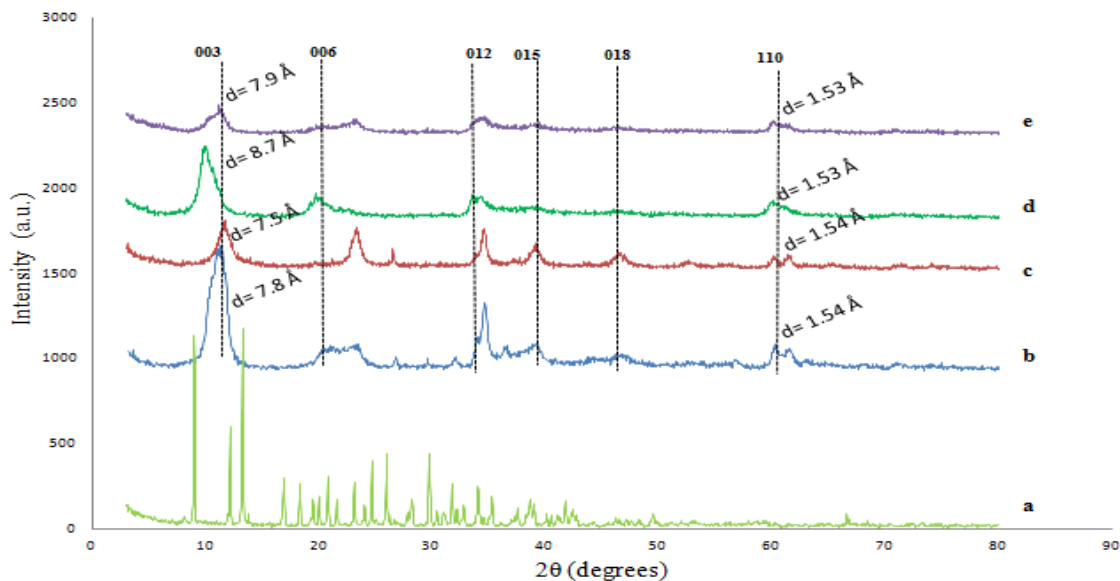


Fig 5-27. XRD patterns of alendronate sodium (a), Zn<sub>3</sub>-G.04-Cp (b), A-Zn<sub>3</sub>-G-IE (c), Zn<sub>3</sub>-GO.04-Cp (d), and A-Zn<sub>3</sub>-GO-IE (e).

Table 5-4. Comparison between the parameters of the loaded samples prepared by ion-exchange, using ametal cations ratio of 3:1 and their controls.

Before drug loading					After drug loading				
Sample precursor	2θ (at 003 plane)	d-spacing (Å)		Interlayer space (Å)	Loaded Sample	2θ (at 003 plane)	d-spacing (Å)		Interlayer space (Å)
		d (003)	d (110)				d (003)	d (110)	
Zn <sub>3</sub> -Cp	10.3°	8.6	1.52	3.83	A-Zn <sub>3</sub> -IE	4.7°	18.6	1.52	13.82
Zn <sub>3</sub> -G.04-Cp	11.3°	7.8	1.54	3.00	A-Zn <sub>3</sub> -G-IE	11.8°	7.5	1.54	2.73
Zn <sub>3</sub> -GO.04-Cp	10.1°	8.7	1.53	4.02	A-Zn <sub>3</sub> -GO-IE	11.2°	7.8	1.53	3.09

Figures 5-28 and 5-29 show the XRD patterns of samples A-Zn2-IE, A-Zn2-G-IE and A-Zn2-GO-IE, which are prepared by loading the free drug dissolved in an aqueous media by ion exchange with the dispersed precursor Zn2-Cp, Zn2-G.04-Cp and Zn2-GO.04-Cp respectively. The parameters are calculated and summarized in table 5-5.

The XRD pattern for sample A-Zn2-IE (figure 5-28). Shows a shift of the peak at plane (003) to a lower  $2\theta$  of  $4.5^\circ$ , and a d-spacing expansion of  $18.5 \text{ \AA}$ . After subtracting the brucite-like layer thickness ( $4.77 \text{ \AA}$ ), it gives an interlayer space of  $13.73 \text{ \AA}$ , suggesting the intercalation of the drug in a bi-layered arrangement [55][61][104]. The peak at (003) is broad and of low intensity, indicating disturbance of the layer stacking of the LDH [6][55]. The calculated d(110) is  $1.53 \text{ \AA}$ , indicating no change in the brucite-like layer [61].

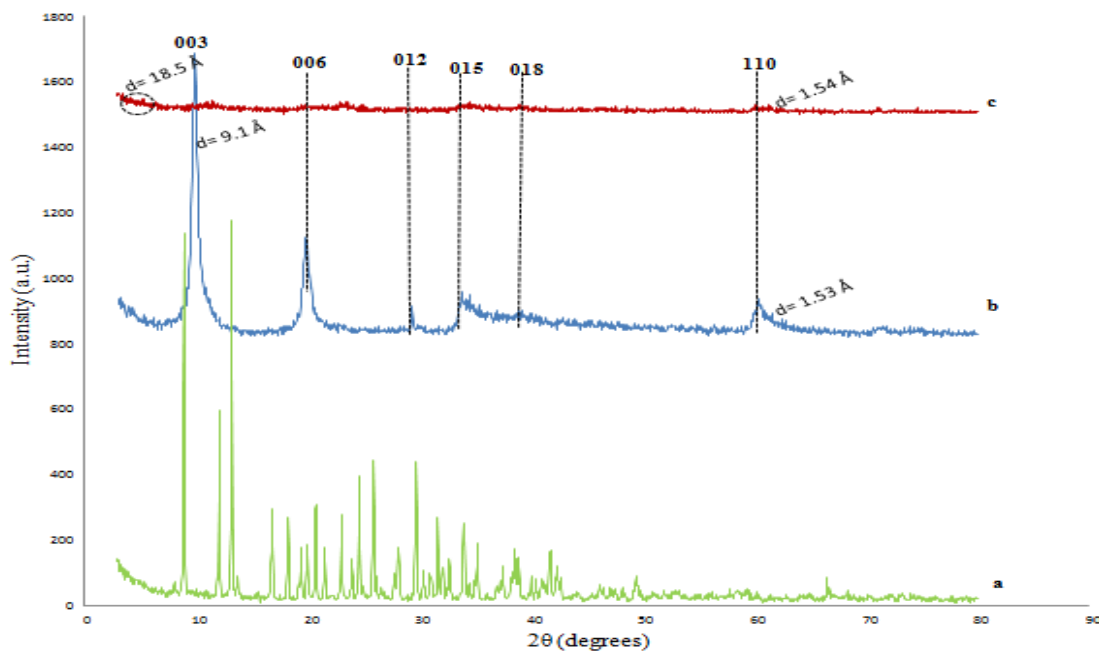


Fig 5-28. XRD patterns of alendronate sodium (a), pristine LDH Zn2-Cp (b), and A-Zn2-IE (c).

The XRD patterns of samples A-Zn2-G-IE and A-Zn2-GO-IE (figure 5-29), show no noticeable change of the d-spacing ( $8.7$  and  $8.5 \text{ \AA}$  respectively) compared to their precursors ( $8.6$  and  $8.8 \text{ \AA}$  respectively). After subtracting the brucite-like layer thickness ( $4.77 \text{ \AA}$ ), it gives an interlayer distance of  $3.8$  and  $4 \text{ \AA}$  respectively, which is equal to the size of the nitrate anion ( $4 \text{ \AA}$ ). These findings suggests failure of drug exchange with nitrate anions. The reflections at (006), (012), and (110) are wide and of low intensity due to the disturbance in the interlayer anions during exchange [1][111]. The calculated

d(110) is 1.53 Å, same as that of the precursors indicating no change in the brucite-like layer [61].

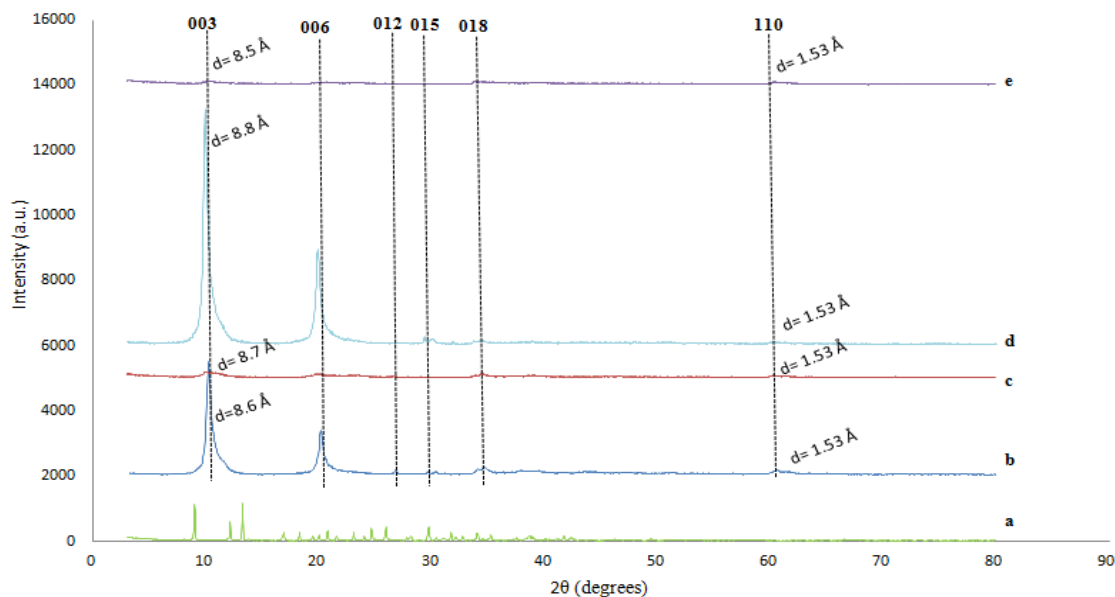


Fig 5-29. XRD patterns of alendronate sodium (a), Zn<sub>2</sub>-G.04-Cp (b), A-Zn<sub>2</sub>-G-IE (c), Zn<sub>2</sub>-GO.04-Cp (d), and A-Zn<sub>2</sub>-GO-IE (e).

Table 5-5. Comparison between the parameters of the loaded samples prepared by ion-exchange, using metal cations ratio of 2:1 and their controls.

Before drug loading					After drug loading				
Sample precursor	2θ (at 003 plane)	d-spacing (Å)		Interlayer space (Å)	Loaded Sample	2θ (at 003 plane)	d-spacing (Å)		Interlayer space (Å)
		d (003)	d (110)				d (003)	d (110)	
Zn <sub>2</sub> -Cp	9.7°	9.1	1.53	4.30	A-Zn <sub>2</sub> -IE	4.5°	18.5	1.54	13.7
Zn <sub>2</sub> -G.04-Cp	10.2°	8.6	1.53	3.89	A-Zn <sub>2</sub> -G-IE	10.1°	8.76	1.53	3.99
Zn <sub>2</sub> -GO.04-Cp	10.0°	8.8	1.53	4.00	A-Zn <sub>2</sub> -GO-IE	10.6°	8.50	1.53	3.70



## B- FTIR

Figure 5-30, shows the FTIR spectra of A-Zn3-IE being compared to its precursor Zn3-Cp and free alendronate sodium. The loaded system (A-Zn3-IE), shows the characteristic broad band at around  $3440\text{ cm}^{-1}$  of pristine LDH, that is attributed to OH groups of the brucite-like layers, adsorbed water molecules, and the OH group of the free alendronate sodium [106][113]. This band overlaps with the stretching vibration band of N-H (primary amine) of the free alendronate sodium, that appears in the range of  $3400\text{--}3250\text{ cm}^{-1}$  [56][106][113]. The nitrate band at  $1380\text{ cm}^{-1}$  of pristine LDH has noticeably decreased, indicating the displacement of the nitrate anions by alendronate sodium, with possible presence of some retained nitrate anions [113][120]. The free drug shows distinctive bands between  $925$  and  $1238\text{ cm}^{-1}$ , which attribute to the stretching vibrations of C-O and P=O bonds. These bands are shifted and overlapped to give a distinctive broad band at around  $1110\text{ cm}^{-1}$  in the loaded sample, which suggests a hydrogen bond interaction with the LDH structure [106][121][122]. The vibration bands appearing at lower frequencies ( $428$ ,  $606$ , and  $831\text{ cm}^{-1}$ ) in the pristine LDH are assigned to the bending vibrations of the M-O and M-O-M bonds in the brucite-like layer [111]. These bands in the loaded samples are shifted ( $580\text{ cm}^{-1}$  and  $966\text{ cm}^{-1}$ ), suggesting a guest-host interaction between the drug and the OH groups of the brucite-like layers, which is also supported by the overlap of these band with that of the drug ( $1110\text{ cm}^{-1}$ ) [113][121][122]. All of these observations confirm the successful intercalation of the alendronate sodium into the LDH interlayer space as has been suggested by the XRD results [120].

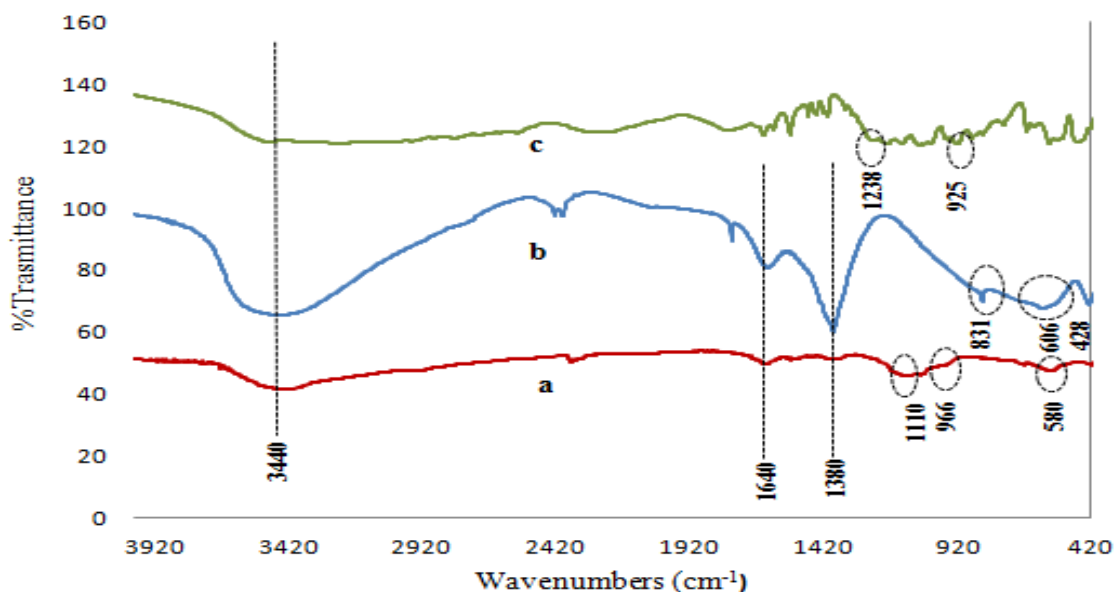


Fig 5-30. FTIR spectra of A-Zn3-IE (a), Zn3-Cp (b), and alendronate sodium (c).

Figure 5-31 and 5-32, show the FTIR spectra of samples A-Zn3-G-IE and A-Zn3-GO-IE. Their XRD results have shown failure of intercalation, but the LDH stayed intact. Therefore, the LDH's characteristic bands and other band features appears in the FTIR pattern as follows:

- OH broad band at around  $3461\text{cm}^{-1}$ .
- Nitrate band at around  $1363\text{ cm}^{-1}$ .
- C-O and P=O stretching vibrations of alendronate sodium at around  $1110\text{ cm}^{-1}$ .
- M-O and M-O-M bonds at their original frequencies at around 400, 600 and  $800\text{ cm}^{-1}$ .

The nitrate band intensity decreases, but did not completely disappear, which indicates the presence of nitrate traces in the interlayers [113][120]. The decrease in the intensity is probably because of the loss of nitrates during the long contact with the solution. The failure of drug exchange is proven by the presence of the M-O and M-O-M bands at their original frequencies. However, the presence of the characteristic alendronate sodium band proves the presence of the drug in the system. The drug's band is shifted from its original frequencies and overlapped, giving a single broad band at  $1110\text{ cm}^{-1}$ , suggesting a hydrogen bond interaction [106][121][122]. Therefore, the drug seem to be adsorbed on the surface of the brucite-like layers rather than intercalated. However, one of the M-O and M-O-M bands overlaps with the drug's band at  $964\text{ cm}^{-1}$  appears in sample A-Zn3-G-IE, but not in A-Zn3-GO-IE, which indicates that the drug in case of A-Zn3-G-IE favors hydrogen bonding with the brucite-like layers rather than G, which is not the case with the A-Zn3-GO-IE, where the drug probably favors the adsorption on the highly functionalized GO rather than the brucite-like layers.

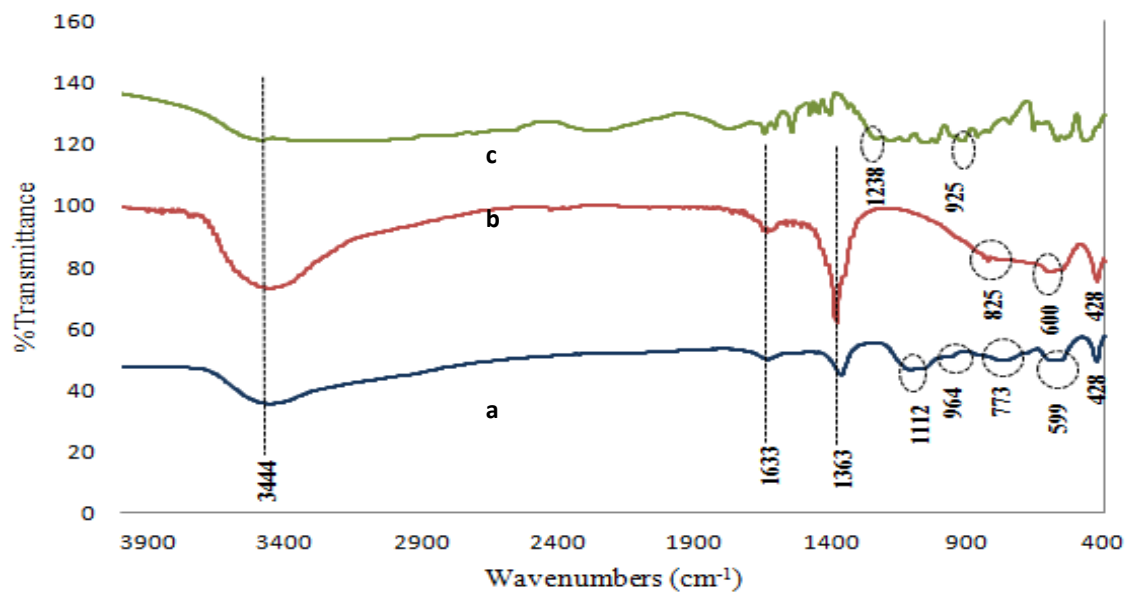


Fig 5-31. FTIR spectra of A-Zn3-G-IE (a), Zn3-G.04-Cp (b), and alendronate sodium (c).

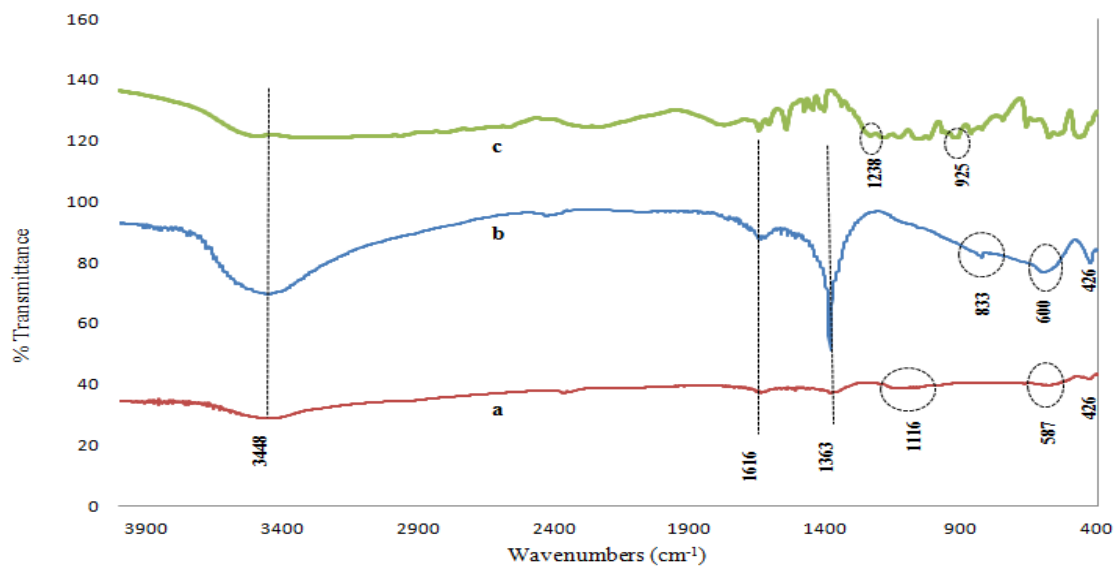


Fig 5-32. FTIR spectra of A-Zn3-GO-IE (a), Zn3-GO.04-Cp (b), and alendronate sodium (c).

Figure 5-33, shows the FTIR spectrum of sample A-Zn2-IE. It has same interpretation and band features as sample A-Zn3-IE, as follows:

- OH broad band at around 3440 cm<sup>-1</sup> of pristine LDH.
- Nitrate nitrate band at around 1367 cm<sup>-1</sup>.
- C-O and P=O stretching vibrations of alendronate sodium appears at 1114 cm<sup>-1</sup>.
- M-O and M-O-M vibration bands of the brucite-like layer at 568, and 966 cm<sup>-1</sup>.

The decrease of the nitrate band, is due to displacement with the drug, but with very small retained traces. The hydrogen bonding and the guest host interaction between the drug and the brucite-like layers, are supported by the overlapping and shift of the alendronate sodium band and the down shift of the M-O and M-O-M bands from their original frequencies [113][121][122].

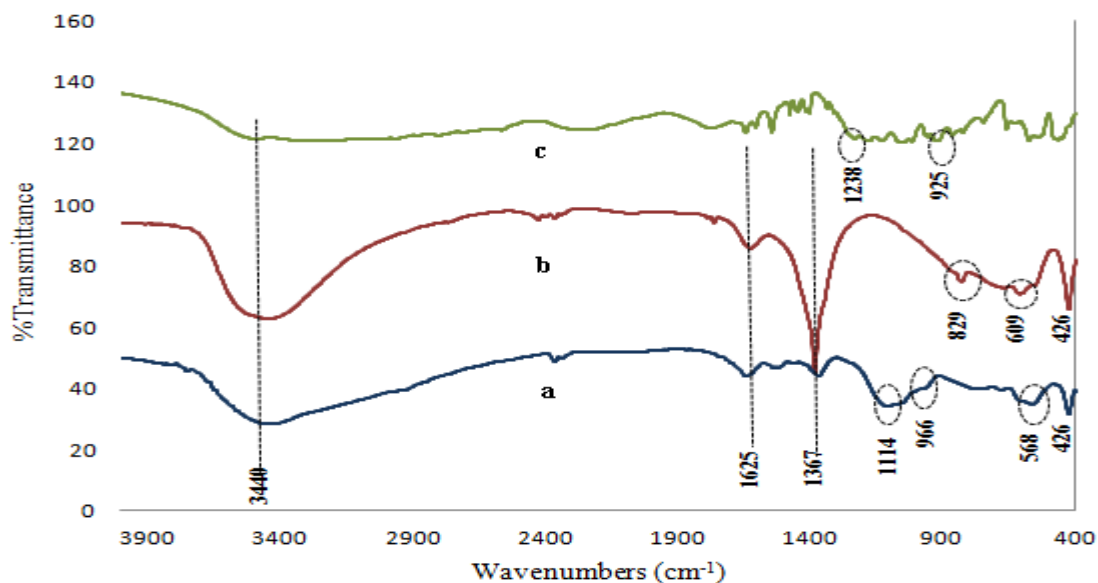


Fig 5-33. FTIR spectra of A-Zn<sub>2</sub>-IE (a), Zn<sub>2</sub>-Cp (b), and alendronate sodium (c).

Figure 5-34 and 5-35, show the FTIR spectra of samples A-Zn<sub>2</sub>-G-IE and A-Zn<sub>2</sub>-GO-IE. They have same interpretation and band features as in samples A-Zn<sub>3</sub>-G-Cp and A-Zn<sub>3</sub>-GO-Cp as follows:

- OH broad band at around 3440 cm<sup>-1</sup> of pristine LDH.
- Nitrate band at 1384 cm<sup>-1</sup>.
- C-O and P=O stretching vibrations bonds of alendronate sodium at around 1112 cm<sup>-1</sup>.
- M-O and M-O-M vibration bands at around 426, 600 and 800 cm<sup>-1</sup>.

The nitrate band intensity is very noticeable, which indicates no displacement of the nitrate anions. The slight decrease in the band intensity is probably because of the loss of nitrates during the long contact with the solution as previously mentioned rather than being exchanged. The failure of drug exchange is proven by the presence of the M-O and M-O-M bands at their original frequencies. However, the characteristic broad band of alendronate sodium, indicates its presence in the LDH system, suggested to be adsorbed

on the surface of the brucite-like layer via hydrogen bonding, supported by the overlapping and shifting of the drug's band and the overlap of one of the M-O and M-O-M bands with the drug's band at  $935\text{ cm}^{-1}$  and  $962\text{ cm}^{-1}$  for A-Zn<sub>2</sub>-G-Cp and A-Zn<sub>2</sub>-GO-Cp respectively [106][113][121][122].

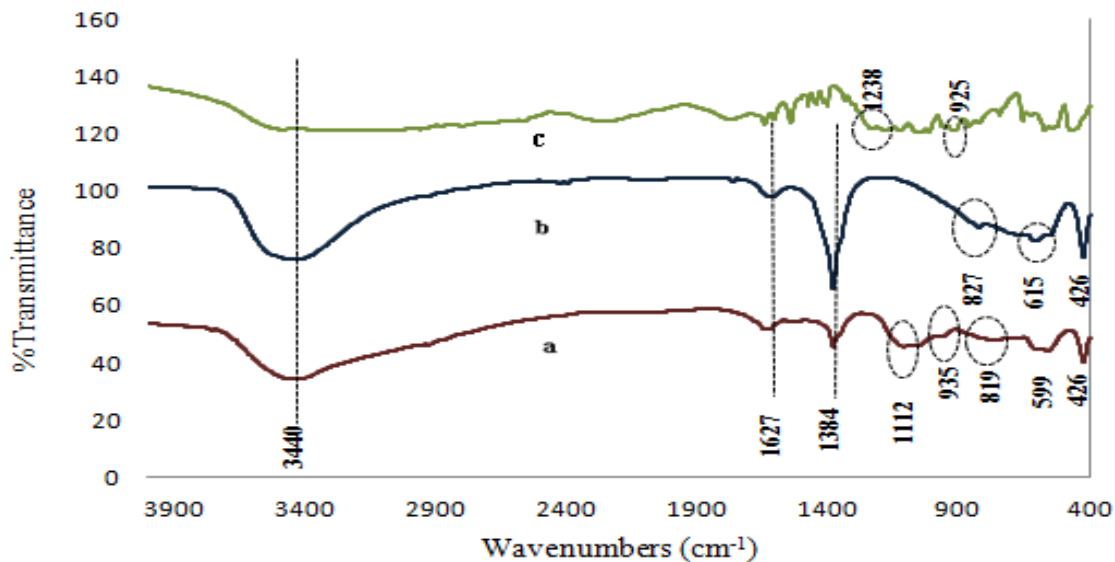


Fig 5-34. FTIR spectra of A-Zn<sub>2</sub>-G-IE (a), Zn<sub>2</sub>-G.04-Cp (b), and alendronate sodium (c).

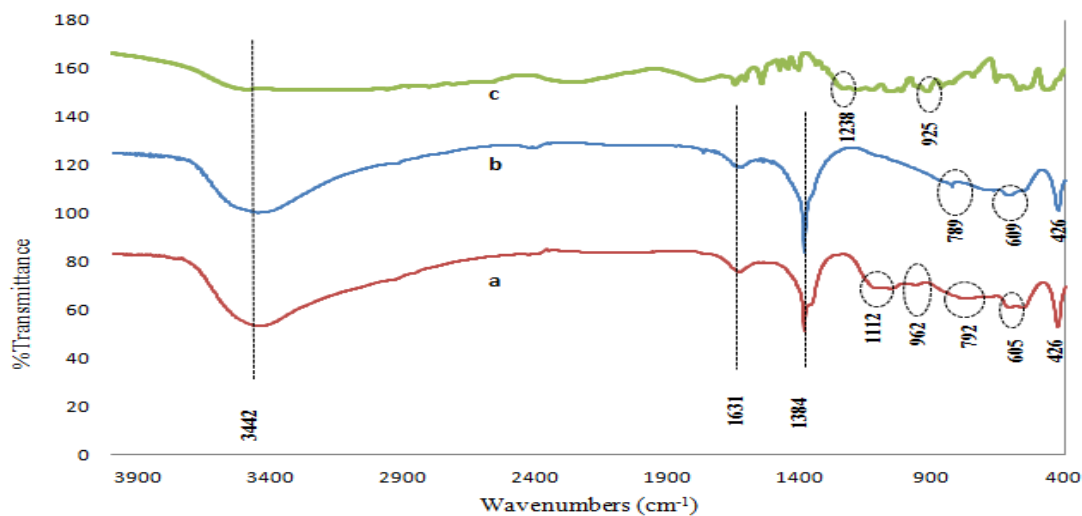


Fig 5-35. FTIR spectra of A-Zn<sub>2</sub>-GO-IE (a), Zn<sub>2</sub>-GO.04-Cp (b), and alendronate sodium (c).

## 5.5. Determination of drug loading and release profile

### 5.5.1. Drug loading:

The amount of drug loaded was calculated for the successfully loaded samples, and the particle size was measured for such samples in order to investigate the relationship between the particle size and the amount of loaded drug. There are some suggested outcomes that could be obtained from such relationship: the particle size might have an effect on the surface area available for loading (inversely proportional), it could be an indication to how the drug is loaded (intercalation or surface adsorption), or show any particles' agglomerates. A summary of the loading percentages and particle size values are shown in table (5-6 and 5-7).

In samples prepared by co-precipitation using  $M^{2+}/M^{3+}$  ratio 3:1 (figure 5-36, blue). The loaded amount of alendronate sodium in sample A-Zn3-Cp is determined to be 25.36 % w/w (amount of loaded drug (mg) per 100 mg of the total hybrid), this loaded amount includes both intercalated drug and that adsorbed on the surface of the brucite-like layers. While the determined intercalated and adsorbed amounts in A-Zn3-G-Cp and A-Zn3-GO-Cp are 36% and 36.6 % w/w respectively. The G/GO-LDH hybrid samples have shown an increase in the percentage loaded, due to the increase of the surface available for drug adsorption provided by the G or GO. Therefore, for the co-precipitated samples, the effect of G and GO on the drug loading was noticeable. However, the size differences between the three samples 656.1, 765.2 and 610.0 nm respectively (table 5-6) are limited, which indicates that loading via intercalation is predominant.

As for samples prepared by co-precipitation using  $M^{2+}/M^{3+}$  ratio 2:1 (figure 5-36, orange): A-Zn2-Cp, A-Zn2-G-Cp and Zn2-GO-Cp, have shown low percentages of loaded drug: 15.26%, 12.28%, and 16.4 % w/w respectively. These low loading percentages are due to the collapse of the LDH structure, leading to no intercalation of the drug. Loaded drug amounts are believed to be mostly surface adsorbed on the exfoliated brucite-like layers, and/or on G and GO. The size difference between that of A-Zn2-Cp and A-Zn2-GO-Cp is minimal (386.4 and 336.9 nm respectively), but that of A-Zn2-G-Cp (1273.4 nm) is noticeably larger. This might be due to G agglomerating by  $\pi$ - $\pi$  stacking, forming large sized particles; without necessarily being accompanied by adsorption of the drug on the G surface, because these agglomerate hinders the drug to reach the surface of the G or LDH.

As an overall findings, the hybrid samples prepared by LDH of  $M^{2+}/M^{3+}$  ratio 3:1 (A-Zn3-Cp, A-Zn3-G-Cp and A-Zn3-GO-Cp), have higher loading percentages compared to those prepared by 2:1 ratio (A-Zn2-Cp, A-Zn2-G-Cp and A-Zn2-GO-Cp), with a further increase in the presence of G or GO.

Table 5-6. The drug loaded amounts and particle sizes of samples prepared by co-precipitation using  $M^{2+}/M^{3+}$  ratios 2:1 and 3:1 respectively.

<b>Sample</b>	<b>Loading (% w/w)</b>	<b>Size (nm)</b>
A-Zn2-Cp	15.3	386.4 ± 85
A-Zn2-G-Cp	16.4	1273.4± 261
A-Zn2-GO-Cp	12.4	336.9± 3
A-Zn3-Cp	25.4	656.1± 16
A-Zn3-G-Cp	36.0	765.2± 43
A-Zn3-GO-Cp	36.6	610.0± 16

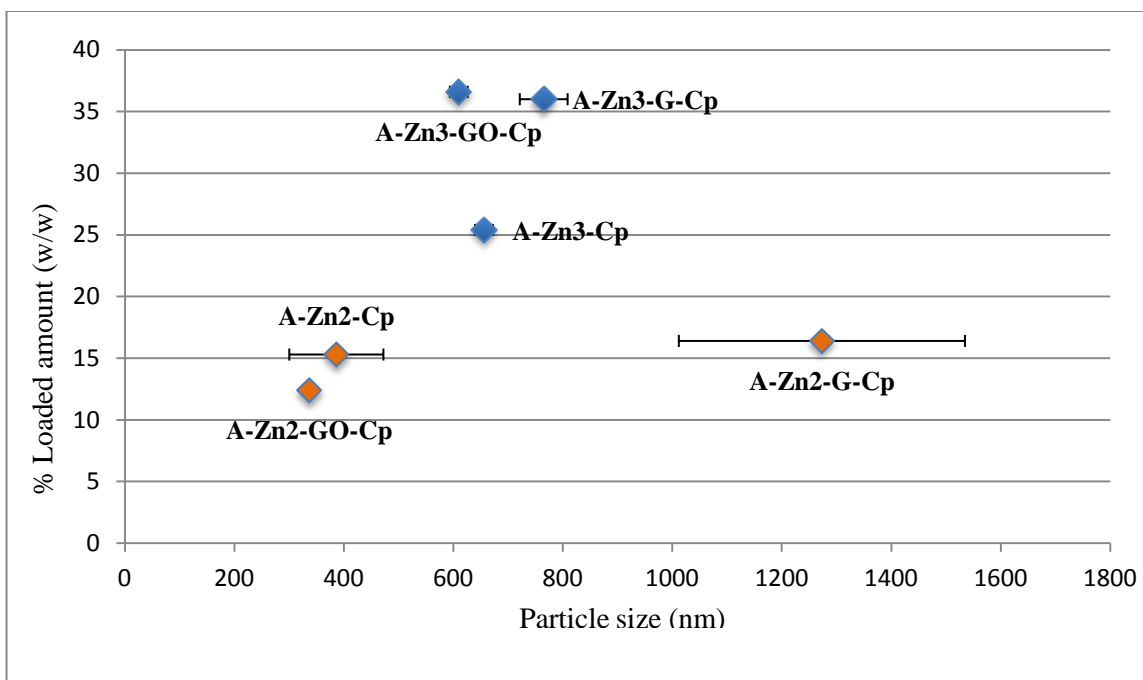


Fig 5-36. A plot of the percentages of the drug loaded (% w/w) versus particle sizes (nm), to compare between the loading percentages, particle sizes and loading-size relationship, among samples prepared by same  $M^{2+}/M^{3+}$  ratio, 3:1 (blue) or 2:1 (orange), and between both ratios.

As for the ion-exchange samples A-Zn3-IE (figure 5-37, green) and A-Zn2-IE (figure 5-37, red), which are prepared using LDH of  $M^{2+}/M^{3+}$  ratio 3:1 and 2:1 respectively, the loaded percentages are 50.5% and 51 % w/w respectively. Both samples almost have the same loading values, in spite of their size difference (380.9 and 853.0 nm respectively), which is very noticeable, suggesting that loading is primarily via intercalation and the size difference is rather due to particles' agglomeration. The loading percentage is high compared to their equivalents in the co-precipitation samples, indicating that the nitrate groups have been largely exchanged during the long contact time with the drug.

As for samples A-Zn3-G-IE (figure 5-37, green) and A-Zn2-G-IE (figure 5-37, red), the loading percentages are 22.5% and 57.3 % w/w respectively. As discussed previously in the XRD results, these two samples have shown loss in the ordered arrangement of the brucite-like layers, therefore the drug loading is believed to primarily be by surface adsorption, with higher loading percentage in sample A-Zn2-G-IE, because the LDH of  $M^{2+}/M^{3+}$  ratio of 2:1 possesses more positive charges, and hence attracting more drug anions onto its surface. This explains the difference in drug loaded amount in spite of the comparable particle size (568.8 and 562.8 nm respectively).



Finally, samples A-Zn3-GO-IE and A-Zn2-GO-IE show almost the same sizes, 299.7 and 290.5 nm respectively and loading percentages: 24 and 25.9 % w/w with slight increase in the latter because of the high positive charges ( $M^{2+}/M^{3+}$  ratio is 2:1). The relatively low loading % in both is attributed to the presence of GO, which may be contributing to the neutralization of charges of the brucite-like layers limiting drug adsorption on the LDH surface.

As an overall findings, the samples prepared using LDH of  $M^{2+}/M^{3+}$  ratio 2:1, and their corresponding in 3:1 samples, have relatively comparable loading percentages, except A-Zn2-G-IE, which has high loading percentage than A-Zn3-G-IE, due to the high charge density as previously discussed. They all have comparable sizes as well except A-Zn2-IE, which has bigger size than A-Zn3-IE, which could be due to agglomeration caused by the high charge density. However, hybrids with GO (A-Zn2-GO-IE, A-Zn3-GO-IE) have shown the lowest loaded amount, due to GO competing to neutralize the brucite-like layers as previously discussed.

Table 5-7. The drug loaded amounts and particle sizes of samples prepared by ion-exchange using  $M^{2+}/M^{3+}$  ratios 2:1 and 3:1 respectively.

<b>Sample</b>	<b>Loading (% w/w)</b>	<b>Size (nm)</b>
A-Zn2-IE	51.0	853.0± 19
A-Zn2-G-IE	57.3	562.8± 24
A-Zn2-GO-IE	25.9	290.5± 3
A-Zn3-IE	50.5	380.9± 1
A-Zn3-G-IE	22.4	568.8± 32
A-Zn3-GO-IE	24.0	299.7± 0

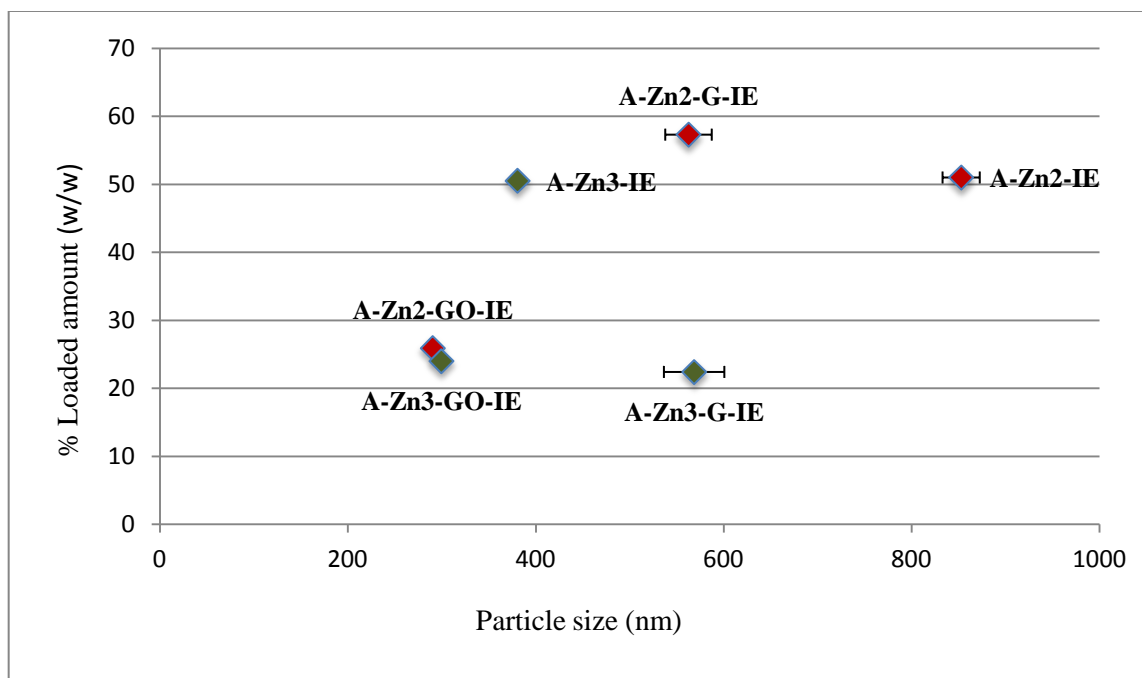


Fig 5-37. A plot of the percentages of the drug loaded (% w/w) versus particle sizes (nm), to compare between the loading percentages, particle sizes and loading-size relationship, among samples prepared by same  $M^{2+}/M^{3+}$  ratio, 3:1 (green) or 2:1 (red), and between both ratios.

System A-Zn2-IE, A-Zn2-G-IE and A-Zn3-IE, are with the highest loaded drug amounts (57.3, 51 and 50.5 mg respectively), which are equivalent to 1.3, 1.04 and 1 mg of alendronate sodium in each mg of the system (drug-LDH, drug-G-LDH and drug-LDH respectively), either adsorbed on the LDH surface or intercalated. These amounts of drug loaded are higher than that reported in the previously mentioned literature reported by Chakraborti (2011) [124], where the alendronate sodium intercalated in Mg/Al LDH system was 0.6 mg/mg LDH [124].

### **5.5.2. Drug release profile:**

Based on the previously discussed XRD and FTIR results, the release profile of the samples that have shown successful loading via intercalation was studied in water for a period of 24 hours according to the USP for alendronate sodium. While the samples that have shown drug loading via surface adsorption were excluded from this study, as would give a burst release rather than sustained.

Figure 5-38 plots the percentage of drug released from the systems prepared by coprecipitation using  $M^{2+}/M^{3+}$  ratio 3:1: A-Zn3-Cp, A-Zn3-G-Cp and A-Zn3-GO-Cp versus time in hours. The three systems show a highly sustained release profile over 24 hours,

giving a slight increase at the end with a total release of 3.5%, 4.2% and 2.9%, from A-Zn3-Cp, A-Zn3-G-Cp and A-Zn3-GO-Cp hybrid systems respectively. This is attributed to the strong attachment of the positively charged brucite-like layers to the intercalated drug guest. The sample with the lowest total release percentage is A-Zn3-GO-Cp is the, because GO has a high functionalized platform that attracts the drug onto its surface through hydrogen bonding, slightly hindering the release of the drug when compared to the other two samples. Followed by Sample A-Zn3-Cp with a slightly higher total release percentage, because it has less charge density, where only the brucite-like layer is the surface attracting the drug, facilitating the release. And finally sample A-Zn3-G-Cp, with the highest total release percentage, because some of the drug is attached to the surface of the brucite-like layer, and others are weakly attached to the surface of G (unfunctionalized), therefore, the drug is easily released.

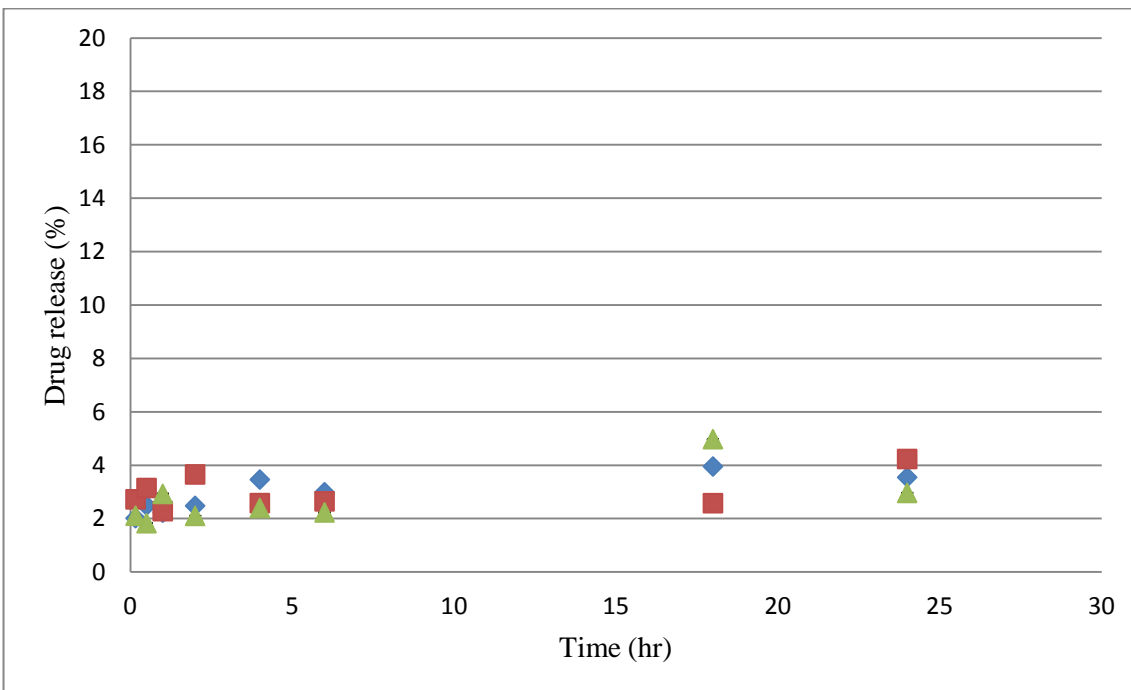


Fig 5-38. Release profile of A-Zn3-Cp (blue), A-Zn3-G-Cp (red) and A-Zn3-GO-Cp (green).

Figure 5-39 shows the release profile of the samples prepared by ion exchange: A-Zn2-IE and A-Zn3-IE, of metal cations ratio 3:1 and 2:1 respectively. The release profile shows a sustained release over 24 hours, giving a total release percentage of 2.1% and 2.5%. The total release percentage of sample A-Zn3-IE is slightly higher, attributed to the fact that the LDH with  $M^{2+}/M^{3+}$  ratio of 3:1 has lower positive charge density than that of sample A-Zn2-IE ( $M^{2+}/M^{3+}$ , 2:1), and therefore, is more likely to lose the hosted drug easily. But in case of A-Zn2-IE, the drug is more attached to the brucite-like layer, hindering its release.

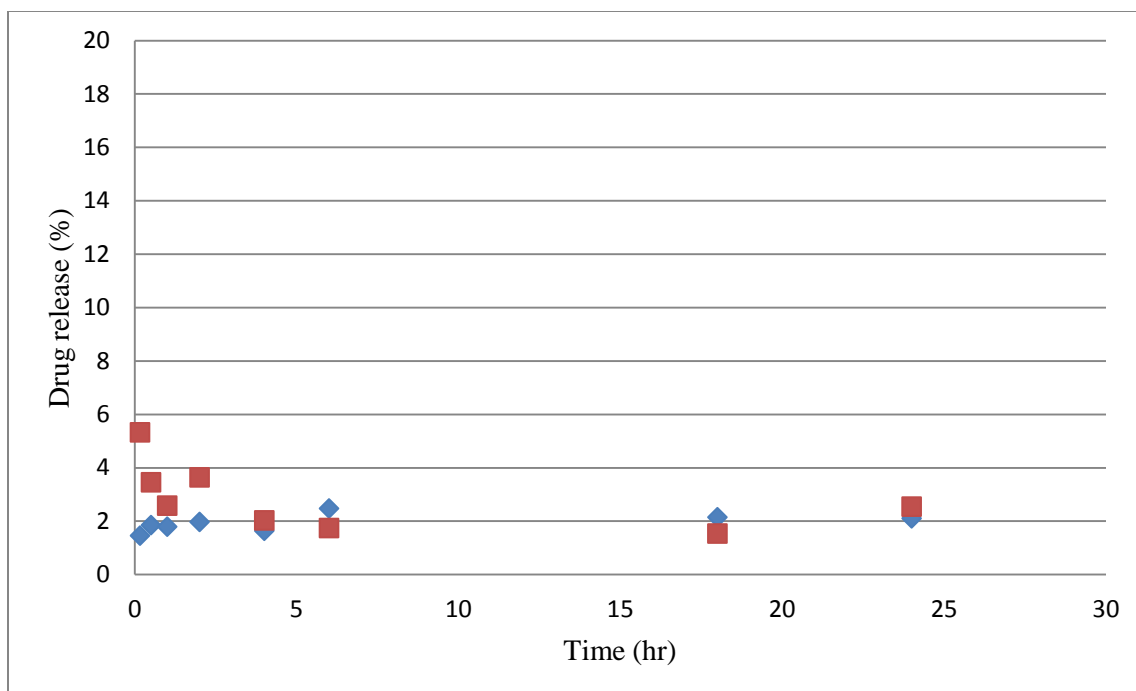


Fig 5-39. Release profile of A-Zn2-IE (blue), and A-Zn3-IE (red).

Table 5-8. Amount and percentages of drug released from 100 mg of hybrid system at 24 hr.

Time interval (hr)	Amount released from 100 mg of hybrid sample at 24 hr (mg)	% Released from 100 mg of hybrid sample at 24 hr
A-Zn3-Cp	0.90	3.5± 0.009
A-Zn3-G-Cp	1.52	4.2±0.034
A-Zn3-GO-Cp	1.08	2.9±0.003
A-Zn2-IE	1.07	2.1±0.002
A-Zn3-IE	1.28	2.5±0.013

Table 5-8 presents a summary of the amounts and percentages of drug released at 24 hr from 100 mg of the hybrid system. These results have been compared to literature reported by Chakraborti [124]. The literature showed burst release of  $\approx 45\%$  over the 6 hour, while that of the systems in this research work, the release over the 6 hours is ranging between 1.7-2.9 %, which continue with a sustained behavior for 24 hrs with maximum drug release ranging between 2.1-4.2 %. As for the one reported in literature had shown a sustained release over 6 days with approximate release of 80 %.






## 5.6. Summary of the work and results

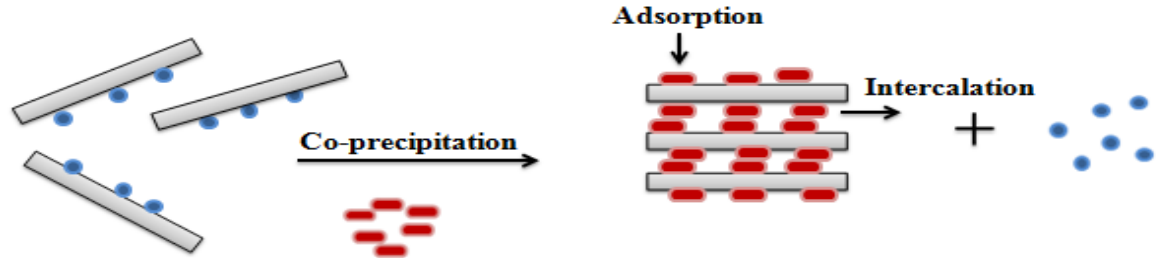
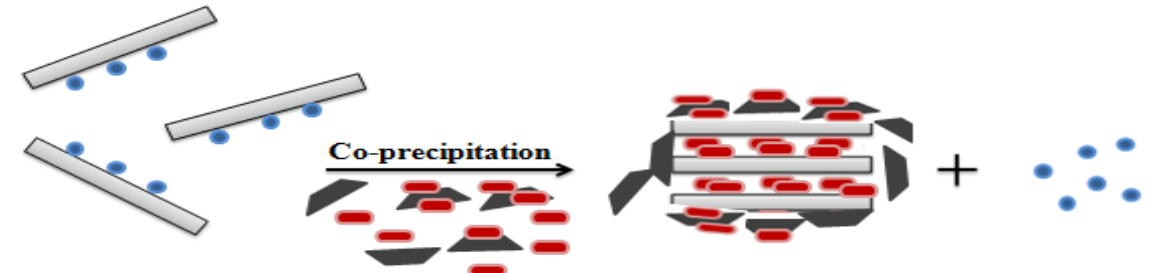
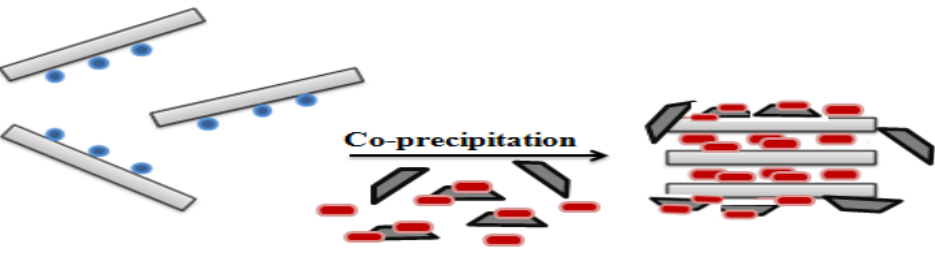
The work is summarized in the following points:

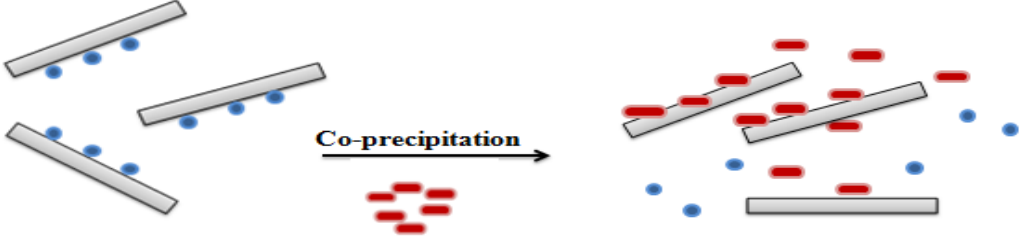
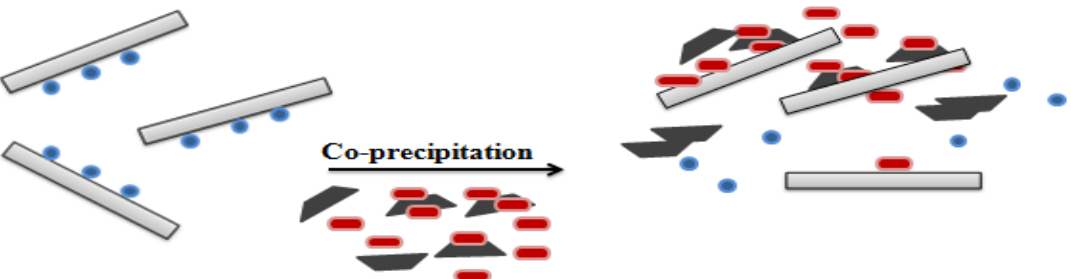
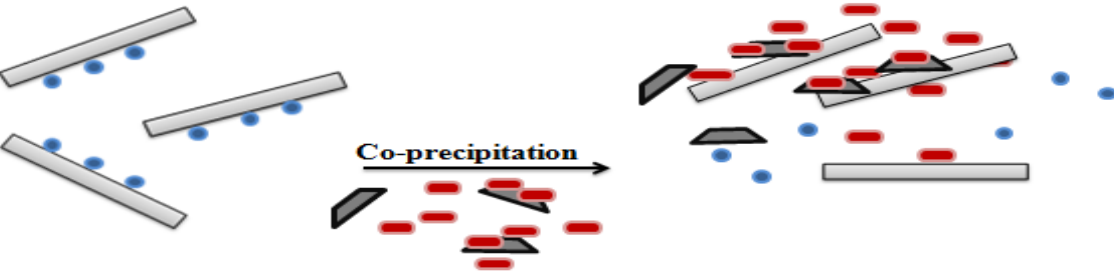
- G was oxidized to GO sheets by Hummers method and characterized by XRD, FTIR and SEM.
- Zn-Al-NO<sub>3</sub> LDH controls of M<sup>2+</sup>/M<sup>3+</sup> ratios 2:1 and 3:1 were prepared for comparison with the loaded corresponding samples.
- Different amounts of G and GO were incorporated with the LDHs by co-precipitation, and the crystallinity of the resulting nanocomposites investigated. The 2 % w/w had the best LDH crystallinity, and therefore was chosen as the amount of G and GO to be incorporated.
- The masses of G and GO corresponding to a content of 2 % w/w in the nanocomposite, were dispersed in water of different volumes to result in suspensions of different concentrations. This was for the purpose of investigating whether the volume of water in which the G and GO were dispersed had any effect on the composition and crystallinity of the final LDH-G and LDH-GO nanocomposites. Different dispersion concentrations gave comparable results for crystallinity. Therefore, the lowest dispersion concentration was chosen (highest volume of water) to ensure better G and GO dispersion.
- The formed nanocomposites were loaded with alendronate sodium by two methods: co-precipitation and ion exchange. They were then characterized by XRD and FTIR, where some have showed loading via intercalation and adsorption.
- Only samples with successful intercalation were tested for their release profile. These exhibited sustained release over 24 hours.
- The prepared samples and a summary of their results are summarized in the following table (5-9).

Table 5-9. All prepared samples and their results, with respect to the following aspects: drug loading mechanism, loaded amount (% w/w), and the total drug released at 24 hr (% of total load).

<b>Zn-Al-NO3 (M<sup>2+</sup>/M<sup>3+</sup>, 2:1)</b>							
Loaded by co-precipitation				Loaded by ion-exchange			
Samples	Loading method	Loaded amount (% w/w)	Total drug released over 24 hr (% of total load)	Samples	Loading method	Loaded amount (% w/w)	Total drug released over 24 hr (% of total load)
<b>A-Zn2-Cp</b>	Primarily via Surface adsorption on LDH layers	15.3	Drug not intercalated	<b>A-Zn2-IE</b>	Primarily via intercalation in bi-layer arrangement and surface adsorption on LDH	51.0	2.1
<b>A-Zn2-G-Cp</b>	Primarily via Surface adsorption on LDH layers and G	16.4	Drug not intercalated	<b>A-Zn2-G-IE</b>	Primarily via surface adsorption on LDH and G	57.3	Drug not intercalated
<b>A-Zn2-GO-Cp</b>	Primarily via Surface adsorption on LDH layers and GO	12.4	Drug not intercalated	<b>A-Zn2-GO-IE</b>	Primarily via surface adsorption on LDH and GO	25.9	Drug not intercalated
<b>Zn-Al-NO3 ( M<sup>2+</sup>/M<sup>3+</sup>, 3:1)</b>							
Loaded by co-precipitation				Loaded by ion-exchange			
Samples	Loading method	Loaded amount (%w/w)	Total drug released over 24 hr (% of total load)	Samples	Loading method	Loaded amount (%w/w)	Total released Over 24 hr (% of total load)
<b>A-Zn3-Cp</b>	Primarily via intercalation in a bi-layer arrangement and surface adsorption on LDH	25.4	3.5	<b>A-Zn3-IE</b>	Primarily via intercalation in a bi-layer arrangement and surface adsorption on LDH	50.5	2.5
<b>A-Zn3-G-Cp</b>	Primarily via intercalation in a bi-layer arrangement and surface adsorption LDH and G	36.0	4.2	<b>A-Zn3-G-IE</b>	Primarily via surface adsorption on LDH and G	22.4	Drug not intercalated
<b>A-Zn3-GO-Cp</b>	Primarily via intercalation in a bi-layer arrangement and surface adsorption LDH and GO	36.6	2.9	<b>A-Zn3-GO-IE</b>	Primarily via surface adsorption on LDH and GO	24.0	Drug not intercalated

Table 5-10. Schematic presentation of the drug loading mechanism in the prepared loaded samples, where each component is represented as follows:  
 LDH(  ), Interlayer nitrate anions (  ), drug anions (  ), G (  ), and GO(  ).

Co-precipitation prepared samples		
Sample	Loading mechanism	Schematic presentation
A-Zn3-Cp	Primarily by intercalation in a bi-layer arrangement and surface adsorption on LDH.	 <p>The diagram shows three grey rectangular layers representing LDH. Blue circles representing interlayer nitrate anions are located between the layers. Red rectangles representing drug anions are adsorbed on the surface of the LDH layers. An arrow labeled "Co-precipitation" points to a structure where the layers are stacked, and red rectangles are on the surface. A downward arrow labeled "Adsorption" points to the surface. An arrow labeled "Intercalation" points to the interlayer space, where blue circles are now located. A plus sign and more blue circles are shown to the right, indicating the final intercalated state.</p>
A-Zn3-G-Cp,	Primarily by intercalation in a bi-layer arrangement and surface adsorption LDH and G.	 <p>The diagram shows three grey rectangular layers representing LDH. Blue circles representing interlayer nitrate anions are located between the layers. Red rectangles representing drug anions are adsorbed on the surface. Black trapezoids representing G are also adsorbed on the surface. An arrow labeled "Co-precipitation" points to a structure where the layers are stacked, and red rectangles and black trapezoids are on the surface. A plus sign and more blue circles are shown to the right, indicating the final intercalated state.</p>
A-Zn3-Go-Cp	Primarily by intercalation in a bi-layer arrangement and surface adsorption LDH and GO.	 <p>The diagram shows three grey rectangular layers representing LDH. Blue circles representing interlayer nitrate anions are located between the layers. Red rectangles representing drug anions are adsorbed on the surface. Grey trapezoids representing GO are also adsorbed on the surface. An arrow labeled "Co-precipitation" points to a structure where the layers are stacked, and red rectangles and grey trapezoids are on the surface. A plus sign and more blue circles are shown to the right, indicating the final intercalated state.</p>

<p><b>A-Zn<sub>2</sub>-Cp</b></p>	<p>Primarily by surface adsorption on LDH layers</p>	 <p>The diagram illustrates the synthesis of A-Zn<sub>2</sub>-Cp. On the left, LDH layers (gray rectangles) have Zn ions (blue dots) adsorbed on their surfaces. In the center, a ZnO precipitate (red rectangles) is shown. An arrow labeled "Co-precipitation" points to the right, where the ZnO-coated LDH layers are formed, with ZnO particles (red rectangles) attached to the LDH surfaces.</p>
<p><b>A-Zn<sub>2</sub>-G-Cp</b></p>	<p>Primarily by surface adsorption on LDH layers and G</p>	 <p>The diagram illustrates the synthesis of A-Zn<sub>2</sub>-G-Cp. On the left, LDH layers (gray rectangles) have Zn ions (blue dots) adsorbed on their surfaces. In the center, a ZnO precipitate (red rectangles) and GO (black sheets) are shown. An arrow labeled "Co-precipitation" points to the right, where the ZnO-coated LDH layers are formed, with ZnO particles (red rectangles) attached to the LDH surfaces and GO sheets (black) also attached to the LDH layers.</p>
<p><b>A-Zn<sub>2</sub>-GO-Cp</b></p>	<p>Primarily by surface adsorption on LDH layers and GO</p>	 <p>The diagram illustrates the synthesis of A-Zn<sub>2</sub>-GO-Cp. On the left, LDH layers (gray rectangles) have Zn ions (blue dots) adsorbed on their surfaces. In the center, a ZnO precipitate (red rectangles) and GO (black sheets) are shown. An arrow labeled "Co-precipitation" points to the right, where the ZnO-coated LDH layers are formed, with ZnO particles (red rectangles) attached to the LDH surfaces and GO sheets (black) also attached to the LDH layers.</p>



**Ion-Exchange prepared samples**

<p><b>A-Zn<sub>2</sub>-IE, and A-Zn<sub>3</sub>-IE</b></p>	<p>Primarily by intercalation in bi-layer arrangement and surface adsorption on LDH</p>	
<p><b>A-Zn<sub>2</sub>-G-IE, and A-Zn<sub>3</sub>-G-IE</b></p>	<p>Primarily by surface adsorption on LDH and G</p>	
<p><b>A-Zn<sub>2</sub>-GO-IE, and A-Zn<sub>3</sub>-GO-IE</b></p>	<p>Primarily by surface adsorption on LDH and GO</p>	

# Chapter 6.

## Conclusion and Future Work

## 6. Conclusion and Future work

---

### 6.1. Conclusion

Nanocomposites of G/GO-Zn-Al LDH were prepared, with 2% w/w of G and GO (prepared by modified Hummers method) incorporated with two different  $M^{2+}/M^{3+}$  ratios of LDH (2:1 and 3:1), and their use as potential drug delivery systems was tested. The samples were tested for the loading and release of alendronate sodium, which is a nBP drug, typically with low bioavailability (< 1%), and gastrointestinal adverse effects.

The nanocomposites, as well as the blank LDH samples, were loaded with alendronate sodium with two methods: co-precipitation and ion-exchange, and they were then characterized by XRD and FTIR. The samples that showed successful intercalation of the drug in bi-layered arrangement are : co-precipitation samples prepared using  $M^{2+}/M^{3+}$  of 3:1 (A-Zn3-Cp, A-Zn3-G-Cp and A-Zn3-GO-Cp), and ion exchange samples with either  $M^{2+}/M^{3+}$  of 2:1 or 3:1, with no G or GO (A-Zn2-IE and A-Zn3-IE). Their drug loading amounts were found to be 25.4, 36.0, 36.6, 51.0, and 50.5 % w/w respectively. The G and GO had a noticeable effect on the amount of drug loaded in the co-precipitation samples (51 and 50.0 % respectively). The release of the drug from these systems were sustained showing almost a plateau over 24 hours, with minimum amounts released, and a total release percentages after 24 hr ranging from 2.1% to 4.2 % which are equivalent to 1.07 and 1.5 mg of the drug respectively, released from 100 mg of the system.

For samples that did not show successful intercalation (A-Zn2-Cp, A-Zn2-G-Cp, A-Zn2-GO-Cp, A-Zn2-G-IE, A-Zn2-GO-IE, A-Zn3-G-IE, and A-Zn3-GO-IE), drug loading was by surface adsorption on the LDH brucite-like layers and G/GO. Their corresponding drug loading amounts are 15.3, 16.4, 12.4, 57.3, 25.9, 22.4, and 24 % w/w respectively. Samples prepared by co-precipitation using  $M^{2+}/M^{3+}$  of 2:1 (A-Zn2-Cp, A-Zn2-G-Cp, and A-Zn2-GO-Cp) were with the lowest loaded amount of the drug, because of the collapse of the LDH layered structure. While samples prepared by ion-exchange, incorporating G/GO (A-Zn3-G-IE, A-Zn3-GO-IE, A-Zn2-G-IE and A-Zn2-GO-IE),

showed the highest loading, because of the long contact of the hybrid with the drug solution allowing more drug to be adsorbed on the surface.

Findings show that two systems are meeting the criteria of high drug loading and sustained release behavior. The systems are A-Zn3-G-Cp and A-Zn3-GO-Cp, with loaded drug amounts of 36 and 36.5 % w/w and sustained release over 24 hrs with total amount released 1.52 and 1.08 mg, which are the highest among samples.

## 6.2. Future work

Future work would focus on the following aspect:

- Molecular simulation, to predict the arrangement of the drug molecules in the LDH interlayers, as well as those adsorbed on the surface.
- To perform a mucus adsorption and a cellular uptake studies to investigate the permeability of the hybrid through the GIT mucus membrane, and its uptake by the bone cells.
- Toxicity test of the hybrid to identify limit of toxicity for oral intake of the required dose.

# References

# References

- [1] D. G. Evans and C. T. Slade, “Structural Aspects of Layered Double Hydroxides,” 1–87, *Structure and Bonding*., 119, 1–87, 2006.
- [2] X. Hou, “Structure And Dynamics Of Layered Double Hydroxides,” PhD. dissertation, Dept. Geology, University of Illinois, Urbana-Champaign, 2001.
- [3] S. Auerbach, K. Carrado, P. Dutta, “Handbook of layered materials,” New York, N.Y; Marcel Dekker Inc, 2004.
- [4] L. Frederick, “Synthesis and Characterisation of Layered Double Hydroxides and their Application for Water Purification,” M.S. thesis, Dept. Chemistry, Queensland University of Technology, Australia, 2012.
- [5] C. Delhoyo, “Layered double hydroxides and human health: An overview,” *Appl. Clay Sci.*, 36, 103–121, 2007.
- [6] F. Cavani, F. Trifirò, A-Vaccari, “Hydrotalcite-type anionic clays: preparation, properties, applications,” *Catalysis Today*, 11, 173-301, 1991.
- [7] S. V. Prasanna and P. V. Kamath, “Anion-Exchange Reactions of Layered Double Hydroxides: Interplay between Coulombic and H-Bonding Interactions,” *Ind. Eng. Chem. Res.*, 48, 6315–6320, 2009.
- [8] J. Choy, S. Choi, J. Oh, and T. Park, “Clay minerals and layered double hydroxides for novel biological applications,” *Appl. Clay Sci.*, 36, 122–132, 2007.
- [9] Y. Kuang, L. Zhao, S. Zhang, F. Zhang, M. Dong, and S. Xu, “Morphologies, preparations and applications of layered double hydroxide micro-/nanostructures,” *Materials (Basel)*., 3, 5220–5235, 2010.
- [10] S.-J. Choi and J.-H. Choy, “Layered double hydroxide nanoparticles as target-specific delivery carriers: uptake mechanism and toxicity,” *Nanomedicine (Lond)*., 6, 803–814, 2011.
- [11] T. Kuila, S. Bose, A. K. Mishra, P. Khanra, N. H. Kim, and J. H. Lee, “Chemical functionalization of graphene and its applications,” *Prog. Mater. Sci.*, 57, 1061–1105, 2012.
- [12] S. Goenka, V. Sant, and S. Sant, “Graphene-based nanomaterials for drug delivery and tissue engineering,” *J. Control. Release*, 173, 75–88, 2014.
- [13] V. Singh, D. Joung, L. Zhai, S. Das, S. I. Khondaker, and S. Seal, “Graphene based materials: Past, present and future,” *Prog. Mater. Sci.*, 56, 1178–1271, 2011.

- [14] C. Soldano, A. Mahmood, and E. Dujardin, "Production, properties and potential of graphene," *Carbon N. Y.*, 48, 2127–2150, 2010.
- [15] Rao, C. N. R, Sood, A. K. "Graphene: synthesis, properties, and phenomena", *John Wiley and Sons, Somerset, NJ, USA*, 21–68, 2013.
- [16] J. Liu, L. Cui, and D. Losic, "Graphene and graphene oxide as new nanocarriers for drug delivery applications.," *Acta Biomater.*, 9, 9243–57, 2013.
- [17] D. C. Marcano, D. V Kosynkin, J. M. Berlin, A. Sinitskii, Z. Sun, A. Slesarev, L. B. Alemany, W. Lu, and J. M. Tour, "Improved synthesis of graphene oxide.," *ACS Nano*, 4, 4806–14, 2010.
- [18] V. C. Sanchez, A. Jachak, R. H. Hurt, and A. B. Kane, "Biological interactions of graphene-family nanomaterials: an interdisciplinary review.," *Chem. Res. Toxicol.*, 25, 15–34, 2012.
- [19] A. M. Pinto, I. C. Gonçalves, and F. D. Magalhães, "Graphene-based materials biocompatibility: A review.," *Colloids Surf. B. Biointerfaces*, 111C, 188–202, 2013.
- [20] S. Makharza, G. Cirillo, A. Bachmatiuk, I. Ibrahim, N. Ioannides, B. Trzebicka, S. Hampel, and M. H. Rummeli, "Graphene oxide-based drug delivery vehicles: functionalization, characterization, and cytotoxicity evaluation," *J. Nanoparticle Res.*, 15, 2099, 2013.
- [21] J. Chen, B. Yao, C. Li, and G. Shi, "An improved Hummers method for eco-friendly synthesis of graphene oxide," *Carbon N. Y.*, 64, 225–229, 2013.
- [22] L. Sun and B. Fugetsu, "Massive production of graphene oxide from expanded graphite." *Material Letters*, 109, 207–210, 2013.
- [23] G. Shao, Y. Lu, F. Wu, C. Yang, F. Zeng, and Q. Wu, "Graphene oxide: the mechanisms of oxidation and exfoliation," *J. Mater. Sci.*, 47, 4400–4409, 2012.
- [24] S. Pei and H.-M. Cheng, "The reduction of graphene oxide," *Carbon N. Y.*, 50, 3210–3228, 2012.
- [25] C. Chung, Y. Kim, D. Shin, S. Ryoo, B. H. E. E. Hong, and D. Min, " Biomedical applications of graphene and graphene Oxide," *Acc. Chem. Res.*, 46, 2211–2224, 2013.
- [26] K. S. Novoselov, V. I. Fal'ko, L. Colombo, P. R. Gellert, M. G. Schwab, and K. Kim, "A roadmap for graphene.," *Nature*, 490, 192–200, 2012.
- [27] Y. Zhu, S. Murali, W. Cai, X. Li, J. W. Suk, J. R. Potts, and R. S. Ruoff, "Graphene and graphene oxide: synthesis, properties, and applications.," *Adv. Mater.*, 22, 3906–24, 2010.

- [28] X. Yang, X. Zhang, Z. Liu, Y. Ma, Y. Huang, and Y. Chen, “High-Efficiency Loading and Controlled Release of Doxorubicin Hydrochloride on Graphene Oxide,” *J. Phys. Chem. C*, 112, 17554–17558, 2008.
- [29] Y. Li, H. Yuan, A. von dem Bussche, M. Creighton, R. H. Hurt, A. B. Kane, and H. Gao, “Graphene microsheets enter cells through spontaneous membrane penetration at edge asperities and corner sites.,” *Proc. Natl. Acad. Sci. U. S. A.*, 110, 12295–300, 2013.
- [30] X. Hu and Q. Zhou, “Health and ecosystem risks of graphene.,” *Chem. Rev.*, 113, 3815–35, 2013.
- [31] X. Guo and N. Mei, “Assessment of the toxic potential of graphene family nanomaterials.,” *J. food drug Anal.*, 22, 105–15, 2014.
- [32] K. Yang, H. Gong, X. Shi, J. Wan, Y. Zhang, and Z. Liu, “In vivo biodistribution and toxicology of functionalized nano-graphene oxide in mice after oral and intraperitoneal administration.,” *Biomaterials*, 34, 2787–95, 2013.
- [33] A. M. Jastrzębska, P. Kurtycz, and A. R. Olszyna, “Recent advances in graphene family materials toxicity investigations.,” *J. Nanopart. Res.*, 14, 1320, 2012.
- [34] M. Saxena and S. Sarkar, “Involuntary graphene intake with food and medicine,” *RSC Adv.*, 4, 30162, 2014.
- [35] T. Drake, L. Clarke, K. Sundeep, “Bisphosphonates: Mechanism of action and role in clinical practice.,” *Mayo. Clin. Proc.*, 83, 1032–1045, 2009.
- [36] F. Karamustafa, N. Çelebi, “Bisphosphonates and Alendronate,” *Pharm. Sci.*, 31, 31–42, 2007.
- [37] R. A. Terkeltaub, “Inorganic pyrophosphate generation and disposition in pathophysiology,” *Am. J. Physiol. Cell Physiol.*, 281, 1-11, 2001.
- [38] W. N. Addison, F. Azari, E. S. Sørensen, M. T. Kaartinen, and M. D. McKee, “Pyrophosphate inhibits mineralization of osteoblast cultures by binding to mineral, up-regulating osteopontin, and inhibiting alkaline phosphatase activity.,” *J. Biol. Chem.*, 282, 15872–83, 2007.
- [39] C. Thouverey, G. Bechkoff, S. Pikula, and R. Buchet, “Inorganic pyrophosphate as a regulator of hydroxyapatite or calcium pyrophosphate dihydrate mineral deposition by matrix vesicles.,” *Osteoarthritis Cartilage*, 17, 64–72, 2009.
- [40] J. Biernacka, K. Betlejewska-kielak, and A. P. Mazurek, “Prediction of Bioavailability of selected bisphosphonates using in silico methods towards categorization into biopharmaceutical classification system,” *Acta pol. Pharm.*, 70, 877–882, 2013.



- [41] D. B. Kimmel, "Mechanism of Action, Pharmacokinetic and Pharmacodynamic Profile, and Clinical Applications of Nitrogen-containing Bisphosphonates," *J. Dent. Res.*, 86, 1022–1033, 2007.
- [42] J. E. Dunford, K. Thompson, F. P. Coxon, S. P. Luckman, F. M. Hahn, C. D. Poulter, F. H. Ebetino, and M. J. Rogers, "Structure-Activity Relationships for Inhibition of Farnesyl Diphosphate Synthase in Vitro and Inhibition of Bone Resorption in Vivo by Nitrogen-Containing Bisphosphonates," *J. Pharmacol. Exp. Ther.*, 296, 235–242, 2001.
- [43] P. Conte and V. Guarneri, "Safety of intravenous and oral bisphosphonates and compliance with dosing regimens.," *Oncologist*, 9 Suppl 4, 28–37, 2004.
- [44] B. J. Gertz, S. D. Holland, W. F. Kline, B. K. Matuszewski, and A. G. Porras, "International Clinical Pharmacology of Alendronate Sodium," *Osteoporos Int.*, 3 13–16, 2000.
- [45] M. H. Yun, J.-S. Woo, and K.-I. Kwon, "Bioequivalence and pharmacokinetics of 70 mg alendronate sodium tablets by measuring alendronate in plasma," *Arch. Pharm. Res.*, 29, 328–332, 2006.
- [46] L. Cruz, E. Assumpção, S. F. Andrade, D. J. Conrado, S. S. Guterres, and A. R. Pohlmann, "Microencapsulation of sodium alendronate reduces drug mucosal damage in rats.," *Drug Deliv.*, 17, 231–7, 2010.
- [47] Q. Lin, X. Huang, J. Tang, Y. Han, and H. Chen, "Environmentally friendly, one-pot synthesis of folic acid-decorated graphene oxide-based drug delivery system," *J. Nanoparticle Res.*, 15, 2144, 2013.
- [48] V. Rives, M. Del Arco, and C. Martín, "Layered double hydroxides as drug carriers and for controlled release of non-steroidal antiinflammatory drugs (NSAIDs): a review.," *J. Control. Release*, 169, 28–39, 2013.
- [49] M. Ramli and K. Yusoff, "Preparation and characterization of an anti-inflammatory agent based on a zinc-layered hydroxide-salicylate nanohybrid and its effect on viability of Vero-3 cells," *International Journal of Nanomedicine*, 8, 297–306, 2013.
- [50] B. Li, J. He, D. Gevans, and X. Duan, "Inorganic layered double hydroxides as a drug delivery system? intercalation and in vitro release of fenbufen," *Appl. Clay Sci.*, 27, 199–207, 2004.
- [51] M. del Arco, a. Fernández, C. Martín, and V. Rives, "Solubility and release of fenbufen intercalated in Mg, Al and Mg, Al, Fe layered double hydroxides (LDH): The effect of Eudragit® S 100 covering," *J. Solid State Chem.*, 183, 3002–3009, 2010.

- [52] M. Wei, S. Shi, J. Wang, Y. Li, and X. Duan, “Studies on the intercalation of naproxen into layered double hydroxide and its thermal decomposition by in situ FT-IR and in situ HT-XRD,” *J. Solid State Chem.*, 177, 2534–2541, 2004.
- [53] M. R. Berber, K. Minagawa, M. Katoh, T. Mori, and M. Tanaka, “Nanocomposites of 2-arylpropionic acid drugs based on Mg-Al layered double hydroxide for dissolution enhancement,” *Eur. J. Pharm. Sci.*, 35, 354–60, 2008.
- [54] M. del Arco, S. Gutiérrez, C. Martín, V. Rives, and J. Rocha, “Synthesis and characterization of layered double hydroxides (LDH) intercalated with non-steroidal anti-inflammatory drugs (NSAID),” *J. Solid State Chem.*, 177, 3954–3962, 2004.
- [55] W. G. Hou and Z.-L. Jin, “Synthesis and characterization of Naproxen intercalated Zn-Al layered double hydroxides,” *Colloid Polym. Sci.*, 285, 1449–1454, 2007.
- [56] V. Ambrogi, G. Fardella, G. Grandolini, and L. Perioli, “Intercalation compounds of hydrotalcite-like anionic clays with antiinflammatory agents — I. Intercalation and in vitro release of ibuprofen,” *Int. J. Pharm.*, 220, 23–32, 2001.
- [57] V. Ambrogi, G. Fardella, G. Grandolini, L. Perioli, and M. C. Tiralti, “Intercalation compounds of hydrotalcite-like anionic clays with anti-inflammatory agents, II: Uptake of diclofenac for a controlled release formulation,” *AAPS PharmSciTech*, 3, 77–82, 2002.
- [58] V. Ambrogi, L. Perioli, M. Ricci, L. Pulcini, M. Nocchetti, S. Giovagnoli, and C. Rossi, “Eudragit® and hydrotalcite-like anionic clay composite system for diclofenac colonic delivery,” *Microporous Mesoporous Mater.*, 115, 405–415, 2008.
- [59] L. Perioli, T. Posati, M. Nocchetti, F. Bellezza, U. Costantino, and a. Cipiciani, “Intercalation and release of antiinflammatory drug diclofenac into nanosized ZnAl hydrotalcite-like compound,” *Appl. Clay Sci.*, 53, 374–378, 2011.
- [60] M. S. San Román, M. J. Holgado, B. Salinas, and V. Rives, “Characterisation of Diclofenac, Ketoprofen or Chloramphenicol Succinate encapsulated in layered double hydroxides with the hydrotalcite-type structure,” *Appl. Clay Sci.*, 55, 158–163, 2012.
- [61] Y. Wang, D. Zhang, Q. Bao, J. Wu, and Y. Wan, “Controlled drug release characteristics and enhanced antibacterial effect of graphene oxide–drug intercalated layered double hydroxide hybrid films,” *J. Mater. Chem.*, 22, 23106, 2012.
- [62] E. Song, W. Han, C. Li, D. Cheng, L. Li, L. Liu, G. Zhu, Y. Song, and W. Tan, “Hyaluronic acid-decorated graphene oxide nanohybrids as nanocarriers for targeted and pH-responsive anticancer drug delivery,” *ACS Appl. Mater. Interfaces*, 6, 11882–90, 2014.
- [63] X. Zhao, L. Liu, X. Li, J. Zeng, X. Jia, and P. Liu, “Biocompatible graphene oxide nanoparticle-based drug delivery platform for tumor microenvironment-responsive triggered release of doxorubicin,” *Langmuir*, 30, 10419–29, 2014.

- [64] X. Sun, Z. Liu, K. Welsher, J. T. Robinson, A. Goodwin, S. Zaric, and H. Dai, "Nano-Graphene Oxide for Cellular Imaging and Drug Delivery.," *Nano Res.*, 1, 203–212, 2008.
- [65] H. Wen, C. Dong, H. Dong, A. Shen, W. Xia, X. Cai, Y. Song, X. Li, Y. Li, and D. Shi, "Engineered redox-responsive PEG detachment mechanism in PEGylated nanographene oxide for intracellular drug delivery.," *Small*, 8, 760–9, 2012.
- [66] H. Xiong, Z. Guo, W. Zhang, H. Zhong, S. Liu, and Y. Ji, "Redox-responsive biodegradable PEGylated nanographene oxide for efficiently chemo-photothermal therapy: a comparative study with non-biodegradable PEGylated nanographene oxide.," *J. Photochem. Photobiol. B.*, 138, 191–201, 2014.
- [67] H. Bao, Y. Pan, Y. Ping, N. G. Sahoo, T. Wu, L. Li, J. Li, and L. H. Gan, "Chitosan-functionalized graphene oxide as a nanocarrier for drug and gene delivery.," *Small*, 7, 1569–78, 2011.
- [68] X. Cao, F. Feng, Y. Wang, X. Yang, H. Duan, and Y. Chen, "Folic acid-conjugated graphene oxide as a transporter of chemotherapeutic drug and siRNA for reversal of cancer drug resistance," *J. Nanoparticle Res.*, 15, 1965, 2013.
- [69] H. Hu, C. Tang, and C. Yin, "Folate conjugated trimethyl chitosan/graphene oxide nanocomplexes as potential carriers for drug and gene delivery," *Mater. Lett.*, 125, 82–85, 2014.
- [70] H. Wu, H. Shi, Y. Wang, X. Jia, C. Tang, J. Zhang, and S. Yang, "Hyaluronic acid conjugated graphene oxide for targeted drug delivery," *Carbon N. Y.*, 69, 379–389, 2014.
- [71] H. Shen, M. Liu, H. He, L. Zhang, J. Huang, Y. Chong, J. Dai, and Z. Zhang, "PEGylated graphene oxide-mediated protein delivery for cell function regulation.," *ACS Appl. Mater. Interfaces*, 4, 6317–23, 2012.
- [72] T. Kavitha, I. Kang, and S. Park, "Poly(acrylic acid)-Grafted Graphene Oxide as an Intracellular Protein Carrier," *Langmuir*, 30, 402–409, 2014.
- [73] H. K. Han, H.-J. Shin, and D. H. Ha, "Improved oral bioavailability of alendronate via the mucoadhesive liposomal delivery system.," *Eur. J. Pharm. Sci.*, 46, 500–7, 2012.
- [74] K. M. Hosny, O. A. A. Ahmed, and R. T. Al-Abdali, "Enteric-coated alendronate sodium nanoliposomes: a novel formula to overcome barriers for the treatment of osteoporosis.," *Expert Opin. Drug Deliv.*, 10, 741–6, 2013.
- [75] J. Ezzati Nazhad Dolatabadi, H. Hamishehkar, M. Eskandani, and H. Valizadeh, "Formulation, characterization and cytotoxicity studies of alendronate sodium-loaded solid lipid nanoparticles.," *Colloids Surf. B. Biointerfaces*, 117, 21–8, 2014.

[76] "Introduction to Powder X-Ray Diffraction History: Wilhelm Conrad Röntgen," [Internet] [Cited 15/1/2015]. Available from:

<http://www.smcr.fisica.unam.mx/8temasutiles/articulosutiles/Bas-XRD.pdf>

[77] "X-Ray Diffraction," [Internet] [Cited 15/1/2015]. Available from:

[http://www.chem.sc.edu/faculty/zurloye/xrdtutorial\\_2013.pdf](http://www.chem.sc.edu/faculty/zurloye/xrdtutorial_2013.pdf)

[78] "Basics of X-Ray Powder Diffraction Required Training to Become an Independent User in the X-Ray SEF," [Internet] [Cited 20/1/2015]. Available from:

<http://prism.mit.edu/xray/oldsite/Basics%20of%20XRay%20Powder%20Diffraction.pdf>

[79] "X-Ray Crystallography," [Internet] [Cited 20/1/2015]. Available from:

<http://www.tulane.edu/~sanelson/eens211/x-ray.htm>

[80] "Basics of X-ray Diffraction." [Internet] [Cited 20/1/2015]. Available from:

<http://old.vscht.cz/clab/RTG/dokumenty/thermo/xrd/Introduction%20to%20powder%20diffraction.pdf>

[81] "Basic X-ray Powder Diffraction ( XRPD )," [Internet] [Cited 20/1/2015]. Available from:

<http://xray.tamu.edu/pdf/notes/intro2xrd.pdf>

[82] A. Hofmann, "12 Spectroscopic techniques: I Spectrophotometric techniques," *Principles and Techniques of Biochemistry and Molecular Biology*, Cambridge, United Kingdom: Cambridge University Press, 477-519, 2010.

[83] D. Harvey, "Spectriscopic methods," *Analytical chemistry*, 2, 1–124, 1856.

[85] "Spectroscopic Techniques Outline," [Internet] [Cited 21/1/2015]. Available from:

<http://research.pbsci.ucsc.edu/chemistry/li/teaching/chem268/Spectroscopic%20techniques.pdf>

[86] "Ultraviolet Spectroscopy," [Internet] [Cited 21/1/2015]. Available from:

[http://opencourseware.kfupm.edu.sa/colleges/cs/chem/chem303/files%5C3-Lecture\\_Notes\\_CHEM-303\\_UV\\_Spectroscopy.pdf](http://opencourseware.kfupm.edu.sa/colleges/cs/chem/chem303/files%5C3-Lecture_Notes_CHEM-303_UV_Spectroscopy.pdf)

[87] T. Nicolet and C. All, "Introduction to Fourier Transform Infrared Spectrometry," *A Thermo Electron Bussines*, 1–8, 2001.

[88] *Handbook for Organic Chemistry Lab*, online ed., University of Colorado, Boulder, Dept. of Chem. And Biochem, 214, 155–164, 2002.

[89] M. Reichenbacher and J. Popp, “Vibrational spectroscopy,” *Challenges in Molecular Structure Determination*, Springer Heidelberg Dordrecht London New York, 63–143, 2012.

[90] B. Stuart, “Introduction,” *Infrared Spectroscopy: Fundamentals and Applications*, 8, 1–13, 2004.

[91] “( IR ) Theory and Interpretation of IR spectra,” [Internet] [Cited 21/1/2015]. Available from:

[https://www.utdallas.edu/~scortes/ochem/OChem\\_Lab1/recit\\_notes/ir\\_presentatio.pdf](https://www.utdallas.edu/~scortes/ochem/OChem_Lab1/recit_notes/ir_presentatio.pdf)

[92] “Structure Determination I: UV-Vis and Infrared Spectroscopy,” [Internet] [Cited 21/1/2015]. Available from:

[http://chemwiki.ucdavis.edu/Organic\\_Chemistry/Organic\\_Chemistry\\_With\\_a\\_Biological\\_Emphasis/Chapter\\_04%3A\\_Structure\\_Determination\\_I/Section\\_4.2%3A\\_Infrared\\_spectroscopy](http://chemwiki.ucdavis.edu/Organic_Chemistry/Organic_Chemistry_With_a_Biological_Emphasis/Chapter_04%3A_Structure_Determination_I/Section_4.2%3A_Infrared_spectroscopy)

[93] “Introduction to Infrared Spectroscopy: Instrumental Analysis,” [Internet] [Cited 22/1/2015]. Available from:

<http://webpage.pace.edu/dnabirahni/rahnidocs/Introduction%20to%20Infrared%20Spectroscopy.ppt>

[94] “Infra-red absorption spectroscopy,” [Internet] [Cited 22/1/2015]. Available from:

<http://teaching.shu.ac.uk/hwb/chemistry/tutorials/molspec/irspec3.htm>

[95] “IR instrumentation,” [Internet] [Cited 22/1/2015]. Available from:

<http://science.unitn.it/~semicon/members/pavesi/FTIR.pdf>

[96] “Sample handling technique for IR analysis,” [Internet] [Cited 22/1/2015]. Available from:

<http://www.bama.ua.edu/~sstreet/Instrumental/ir.PDF>

[97] W. Hawkes and C.H. Spence, “Scanning electron microscope,” *Science of Microscopy* (Department of physics), Springer Science+Business Media, LLC, New York, USA, 1, 133–272, 2008.

- [98] Carrassi and S. Abati, "Introduction to scanning electron microscopy," *Mondo odontostomatologico*, 29, 29–36, 2012.
- [99] F. Bierring and P. Skaaring, "Scanning electron microscopy," *Ugeskr. Laeger*, 137, 2499–2502, 1975.
- [100] M. F. Chisholm, "Fundamentals of scanning electron microscopy," *Scanning Microscopy for Nanotechnology*, Springer Science+Business Media, LLC, New York, USA, 1–39, 2006.
- [101] G.H. Michler, "Scanning electron microscopy (SEM)," *Electron Microscopy of Polymers*, Springer-Verlag Berlin Heidelberg, Germany, 87–120, 2008.
- [102] Anonymous, "Malvern launches new zetasizer nanoseries," *Powder Metallurgy*, 46, 1-8, 2003.
- [103] Anonymous, "New autotitrator for Zetasizer nano," *Powder Metallurgy*, 47, 1-12, 2004.
- [104] F. Zahraa, "Zn-Al and Mg-Al layered double hydroxides as nanostructured carriers for vitamins," M.S. Thesis, Dept. Chemistry, Egypt, 2012.
- [105] P. Nalawade, B. Aware, V.J. Kada and R.S. Hirleker, "Layered double hydroxides: A review," *Journal of Scientific and Industrial Research*, 68, 267-272, 2009.
- [106] G. Ananchenko, "Alendronate sodium," *Profiles of Drug Substances, Excipients, and Related Methodology*, 38, 1-33, 2013.
- [107] M.I. Walsh, M.E.S. Metwally, M. Eid and R.N. EL-Shaheny, "Spectroscopic determination of Risedronate in pharmaceutical formulations via complex formation with Cu (II) ions: Application to content uniformity testing," *Int. J. Biomed. Sci.*, 4, 303-309, 2008.
- [108] D. Ostović, C. Stelmach and B. Hulshizer, "Formation of chormophoric complex between alendronate and copper (II) ions," *Pharmaceutical Research*, 10, 470-472, 1993.
- [109] N. Salak, J. Tedim, I. Kuznetsova, L. Ribeiro, G. Vieira, L. Zheludkevich, and G.S. Ferreira, "Comparative X-ray diffraction and infrared spectroscopy study of Zn-Al layered double hydroxides: Vandate vs nitrate," *Chemical Physics*, 397, 102-108, 2012.
- [110] S. Miyata, and A. Okada, "Synthesis of hydrotalcite-like compounds and their physico-chemical properties : the sytems of Mg-Al-SO<sub>4</sub>, and Mg-Al-CrO<sub>4</sub>," *Clays and Clay Minerals*, 25, 14-18, 1977.
- [111] V. Rives, "Characterization of layered double hydroxides and their decomposition products," *Materials Chemistry and Physics*, 75, 19-25, 2002.

- [112] E. M. Seftel, E. Popovici, M. Mertens, K. De Witte, G. Van Tendeloo, P. Cool, and E. F. Vansant, "Zn-Al layered double hydroxides: Synthesis, characterization, and photocatalytic application," *Microscopic and Mesoporous Materials*, 113, 296-304, 2008.
- [113] R. Xiao, W. Wang, L. Pan, R. Zhu, Y. Yu, H. Li, H. Liu, and S. Wang, "A sustained folic acid release system based on ternary magnesium/ zinc/ aluminum layered hydroxides," *J. Mater. Sci.*, 46, 2635-2643, 2011.
- [114] C. Puscasu, C. Gherasim, D. Mardare, and G. Carja, "Structural of the textured properties of some layered double hydroxides," *Acta. Chemica. Iasi.*, 21, 1-8, 2013.
- [115] M. Regí, "Revisiting ceramics for medical applications," *Royal Society of Chemistry*, 44, 5211-5220, 2006.
- [116] M. Regí, and M. Monzano, "New developments in ordered mesoporous materials for drug delivery," *Royal Society of Chemistry*, 20, 5593-5604, 2010.
- [117] F. Zhang, Y. Song, S. Song, R. Zhang, and W. Hou, "Synthesis of magnetite-graphene oxide-layered double hydroxide composites and applications for the removal of Pb(II) and 2,4-dichlorophenoxyacetic acid from aqueous solutions," *ACS Appl. Mater. Interfaces*, 7, 7251-7263, 2015.
- [118] Z. Gao, J. Wang, Z. Li, W. Yang, B. Wang, M. Hou, Y. He, Q. Liu, T. Mann, P. Yang, M. Zhang, and L. Liu, "Graphene nanosheet/Ni<sup>2+</sup>/Al<sup>3+</sup> layered double hydroxide composite as a novel electrode for a super capacitor," *Chem. Mater.*, 23, 3509-3516, 2011.
- [119] K. Zou, H. Zhag, and X. Duan, "Studies on the formation of 5-aminosalicylate intercalated Zn/Al molar ratios and synthesis routes," *Chemical Engineering Science*, 62, 2022-2031, 2007.
- [120] M. Sillion, D. Hritcu, M. Jaba, B. Tamba, D. Ionescu, C. Mungiu, M. Popa, "In vitro and in vivo behaviour of ketoprofen intercalated into layered double hydroxides," *J Mater Sci: Mater Med*, 21, 3009-3018, 2010.
- [121] S. Gordon, X. Cao, A. Mohamed, and J. Willett, "Infrared spectroscopy method reveals hydrogen bonding and intermolecular interaction between components in polymer blends," *Applied Polymer Science*, 97, 813-821.
- [122] M. Wolf, C. Shumann, R. Gross, T. Domratcheva, and R. Diller, "Ultra fast infrared spectroscopy of riboflavin: Dynamics, electronic structure, and vibrational mode analysis," *J. Phys. Chem B*, 112, 13424-13432, 2008.
- [123] "Molecular gate adsorption technology," [Internet] [Cited 20/8/2015]. Available on: <http://www.moleculargate.com/molecular-gate-adsorption-systems.html>

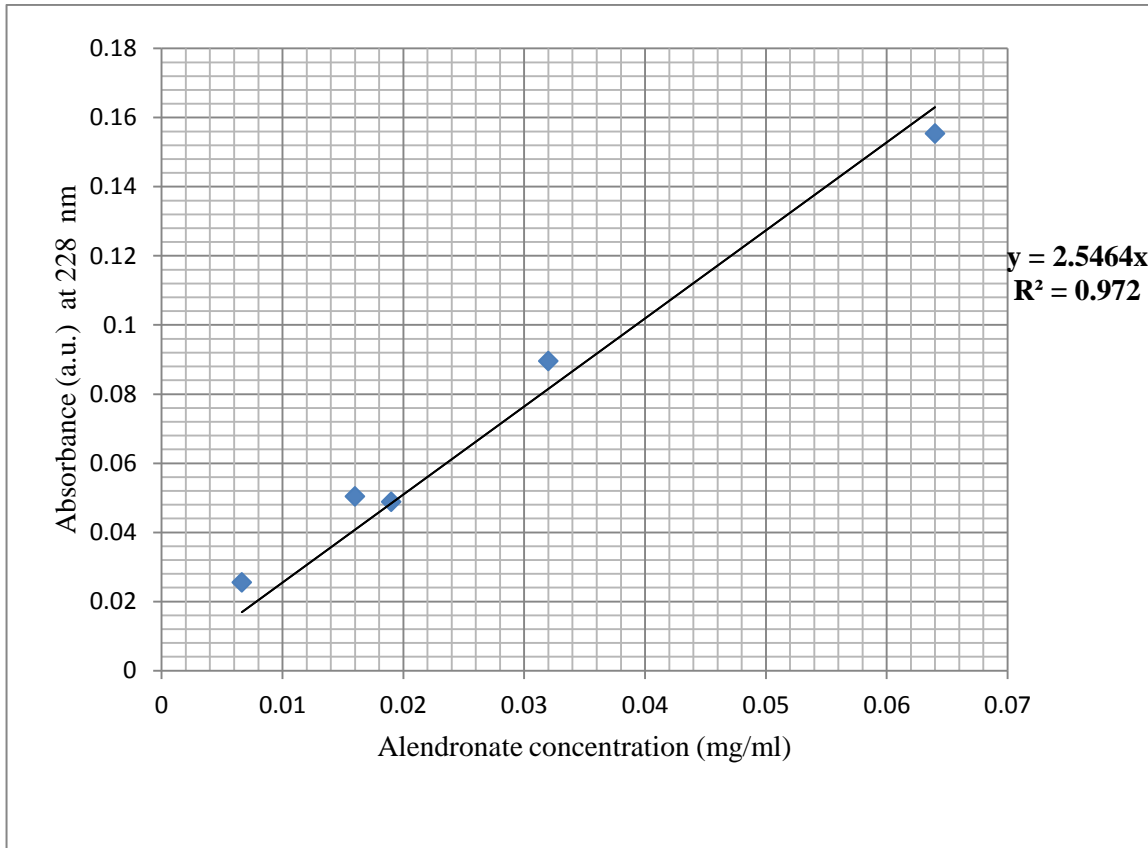
[124] M. Chakraborti, “ The development and characterization of nanocomposite films for the controlled release and localized delivery of alendronate and tetracycline for periodontal application,” M.S. Thesis, Dept. Pharmaceutical Science, British Columbia University, Vancouver, 2011.



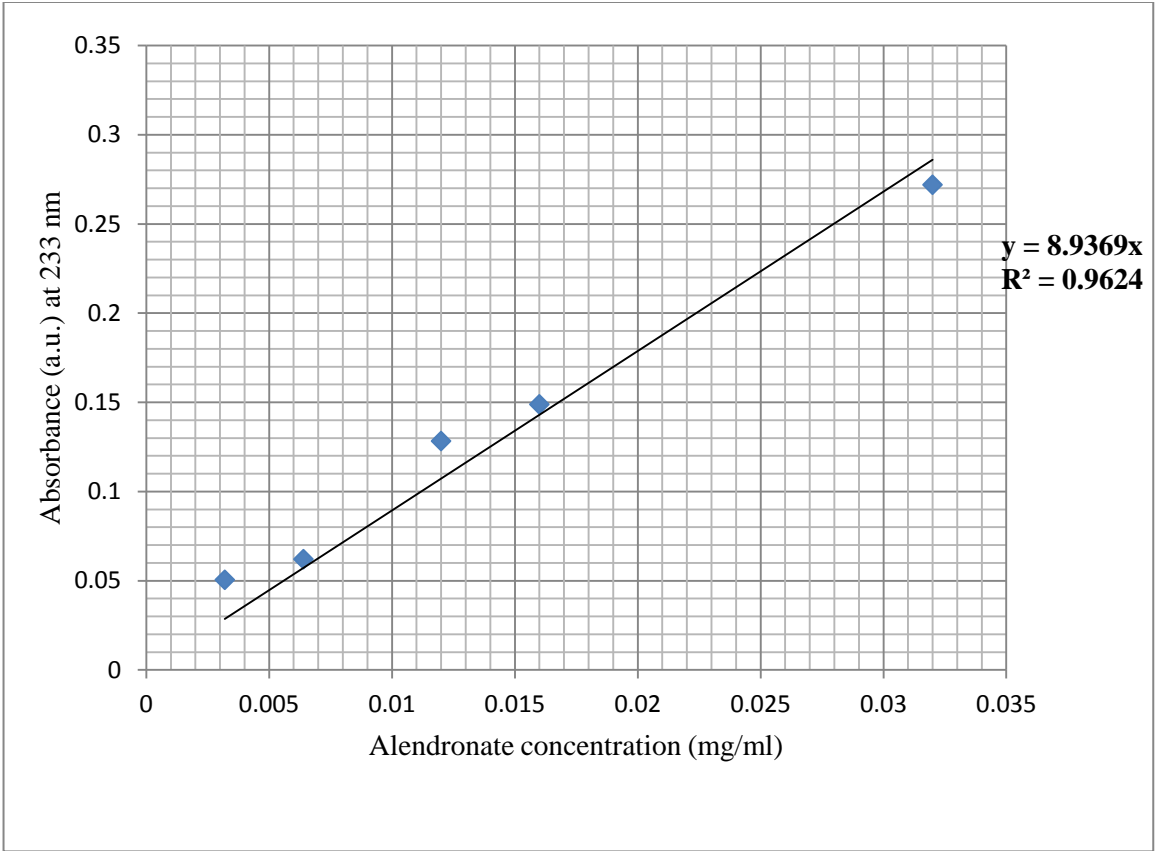
# Appendix A

## Calibration Curves

## Appendix A: Calibration curves



**Calibration curve of Alendronate sodium in simulated gastric fluid for the loading determination test.**



**Calibration curve of Alendronate sodium in de-ionized water for the release test.**